

ANALYSIS OF ACOUSTIC REFLECTIONS FOR THE DETECTION OF OBSTRUCTIONS
IN LIQUID-FILLED TUBES

By

Ricardo H. Castañeyra Tamariz

A thesis submitted in partial fulfillment of the requirements for the
degree of

MASTER OF SCIENCE
in

ELECTRICAL ENGINEERING

UNIVERSITY OF PUERTO RICO
MAYAGÜEZ CAMPUS

July, 2011

Approved by:

Silvina Cancelos, Ph.D.
Member, Graduate Committee

Date

Henrick M. Ierkic, Ph.D.
Member, Graduate Committee

Date

Eduardo J. Juan, Ph.D.
President, Graduate Committee

Date

Alberto Santana, Ph.D.
Representative of Graduate Studies

Date

Erick Aponte, Ph.D.
Chairperson of the Department

Date

ABSTRACT

Detection and estimation of obstructions located in liquid-filled tubes is a major concern that ranges from oil industries to medical applications. In the medical devices field, the obstruction detection and estimation could be used in catheters, infusion pumps, etc. Acoustic reflections produced by obstructions of different type, size and positions along water-filled tubes made of PVC, copper and vinyl were analyzed, in order to extract their acoustic signatures that identifies each obstruction along the water-filled tubes. The acoustic propagation becomes complex since the tubes are water-filled, resulting in many propagation modes traveling at different velocities, which are frequency dependent. To overcome the complex reflection analysis, the reflections envelope and spectrogram time-axis projection features were extracted and stored in a database for each obstruction type, size and position. The extracted features of unknown obstructions reflection were compared with the features database using the Euclidean distance formula to estimate the obstruction type, size and position. For the water-filled PVC tube, the obstruction position was estimated with an accuracy of 78.8% and error of $0.93 \pm 0.59\text{cm}$ (mean \pm STD) using the signal envelope. The obstruction size was estimated with 74.4% of accuracy with an error of $-1.78 \pm 3.98\%$, and the obstruction type with an accuracy of 71.5% using the time-axis projection. For the water-filled copper tube, the obstruction position was estimated with an accuracy of 85.3% and error of $0.19 \pm 2.04\text{cm}$, the obstruction size with accuracy of 93.0% and error of $-0.10 \pm 3.44\%$, and the obstruction type with accuracy of 99.2%, all using the signal envelope. In the water-filled vinyl tube, the obstruction position was estimated with an accuracy of 85.2% and error of $0.02 \pm 0.86\text{cm}$, the obstruction size with accuracy of 90.3% and error of $-0.22 \pm 3.71\%$, and the obstruction type with accuracy of 99.1%, all using the signal envelope.

RESUMEN

La detección y estimación de obstrucciones localizadas en tubos llenos de líquido es una gran preocupación que cubre desde las industrias de petróleo hasta aplicaciones médicas. En el área de la medicina la detección y estimación de obstrucciones se podría utilizar, por ejemplo, en catéteres, bombas de infusión, etc. Reflexiones acústicas producidas por obstrucciones de diferentes materiales, tamaño y posición a lo largo de tubos de PVC, cobre y vinil llenos de agua fueron analizadas, con el fin de extraer su huella acústica que identifica cada una de las obstrucciones a lo largo de los tubos. La propagación acústica en tubos llenos de agua se vuelve compleja, ya que hay diferentes modos de propagación viajando a distintas velocidades las cuales son dependientes de frecuencia. Dado a la complejidad de las reflexiones se extrajo y almacenó la proyección del eje de tiempo del espectrograma y la envoltura para cada tipo de obstrucción, tamaño y posición en cada tubo. Estas características se extrajeron de reflexiones causadas por obstrucciones desconocidas para ser comparadas usando la fórmula de distancia Euclidiana con la base de datos anteriormente creada, y así poder estimar el tipo de obstrucción, su tamaño y posición. La estimación de posición en el tubo lleno de agua de PVC se logró con una exactitud de 78.8% y un error de $0.93 \pm 0.59\text{cm}$ (promedio \pm SD) usando la envoltura de la señal. La estimación de tamaño se obtuvo con una exactitud de 74.4% y un error de $-1.78 \pm 3.98\%$ (promedio \pm SD), y la estimación de tipo de obstrucción con una exactitud de 71.5% usando la proyección del eje de tiempo. En el tubo de cobre la estimación de posición de las obstrucción se logró con una exactitud de 85.3% y un error de $0.19 \pm 2.04\text{cm}$, el tamaño con una exactitud de 93.0% y un error de $-0.10 \pm 3.44\%$, y el tipo con una exactitud de 99.2%, todos usando la envoltura de la señal. Para el tubo de vinil la estimación de posición de las obstrucción se logró con una exactitud de 85.2% y un error de $0.02 \pm 0.86\text{cm}$, el tamaño con una exactitud de 90.3% y un error de $-0.22 \pm 3.71\%$, y el tipo con una exactitud de 99.1%, todos usando la envoltura de la señal.

. . . I still remember the exact moment and time when my mother asked me, “Are you going to do your master’s right?”

To my parents Teresa Tamariz (R.I.P) and Carlos R. Castañeyra, my brother Carlos J. Castañeyra, and my girlfriend Kidian D. Santana and her family. Thanks for all your love, support and encouragement during these years. You were my motivation.

ACKNOWLEDGMENTS

This research was supported by the *Biomedical Instrumentation Research Laboratory*. I want thank the University of Puerto and the Department of Electrical and Computer Engineering of Mayagüez Campus for giving me the opportunity to grow intellectually and for the economic support throughout these years.

Thanks to Dr. Eduardo J. Juan for your guidance, support, friendship, help and most important allowing me to work with you during these years, letting me become a better engineer and person.

I want to make a special acknowledgment and thanks to Dr. Mario Ierkic and Dr. Silvina Cancelos for your advice and unconditional support.

I also want to thanks my colleagues and friends, Javier Tafúr, Andrés Salazar, Michelle Visbal and Rafael González for your unconditional friendship and support during the process of measuring at least 8,000 measurements and all the other amazing moments I lived with you throughout these years.

TABLE OF CONTENTS

	<u>page</u>
ABSTRACT.....	ii
RESUMEN	iii
LIST OF FIGURES	viii
LIST OF TABLES.....	xvii
1 INTRODUCTION	1
1.1 Clinical Problem	1
1.2 Actual Treatments for Occluded Catheters	3
1.3 Acoustic Pulse Reflectometry Method and Principles	4
1.3.1 Brief Summary of Sonar and Pulse-Echo Technique.....	5
1.4 Acoustic Pulse Reflectometry Applications.....	6
1.4.1 Biological Applications	6
1.4.2 Other Applications	6
1.5 Previous Works in Air and Liquid Sound Propagation.....	7
1.6 Objectives	9
1.7 Outline.....	10
2 THEORETICAL BACKGROUND	11
2.1 Sonar and Pulse-Echo Technique.....	11
2.2 Reflections in Lossless Rigid Tubes	14
2.3 Acoustic Losses in Rigid Tubes.....	16
2.4 Sound Propagation in Waveguides with Constant Cross Sectional Area	18
2.5 Bessel Functions	20
2.6 Propagation Modes	22
2.7 Acoustic Signal Processing	23
2.7.1 Acoustic Signature and Recognition Framework.....	24
3 MATERIALS AND METHODS.....	26
3.1 Experimental System Setup	26
3.2 Signal Processing and Analysis	31
3.3 Experimental Design.....	37
4 EXPERIMENTAL RESULTS.....	43
4.1 PVC Tube Measurements	43

4.1.1 Wave Propagation in PVC Tube.....	43
4.1.2 PVC Tube Reflections Analysis.....	46
4.1.2.1 Onset Detection in PVC Tube.....	46
4.1.2.2 Feature Extraction of PVC Tube Reflections.....	52
4.1.2.2.1 Spectrogram Time-Axis Projection	52
4.1.2.2.2 Reflection Signal Envelope.....	55
4.1.2.2.3 Extracted Features as a Function of Obstruction Type	57
4.1.3 Signal Matching Algorithm.....	58
4.1.3.1 Database Creation	58
4.1.3.2 Signal Matching Results	59
4.1.3.2.1 Signal Matching Algorithm Accuracy and Average Errors Detecting Stainless Steel Obstructions	69
4.1.3.2.2 Signal Matching Algorithm Accuracy and Average Errors Detecting Delrin Obstructions	73
4.2 Copper Tube Measurements	77
4.2.1 Signal Matching Results	78
4.2.1.1 Signal Matching Algorithm Accuracy and Average Errors Detecting Stainless Steel Obstructions	79
4.2.1.2 Signal Matching Algorithm Accuracy and Average Errors Detecting Delrin Obstructions	83
4.3 Vinyl Tube Measurements	87
4.3.1 Signal Matching Results	89
4.3.1.1 Signal Matching Algorithm Accuracy and Average Errors Detecting Stainless Steel Obstructions	89
4.3.1.2 Signal Matching Algorithm Accuracy and Average Errors Detecting Delrin Obstructions	93
4.4 Signal Envelope and Time-Axis Projection Comparison to Estimate Obstruction Type, Size and Position in Water-Filled PVC, Copper and Vinyl Tubes.....	97
5 CONCLUSIONS AND RECOMENDATIONS	100
REFERENCES	103

LIST OF FIGURES

Figure 1-1 Central venous catheter of three lumen in a patient jugular vein (a) and a catheter kit with the saline injections (b).....	1
Figure 1-2 Example of a CVC insertion in the superior vena cava (a) and a Foley catheter for urinary extraction (b).....	2
Figure 1-3 Example of a CVC in a patient receiving hemodialysis.....	3
Figure 1-4 Chest X-Ray Fluoroscopy showing the Swan-Ganz catheter with its distal end in the proximal pulmonary artery. [4]	3
Figure 1-5 Example of the active sonar Surveillance Towed Array Sensor System (SURTASS) Low Frequency Active (LFA) used by the U.S. Navy. [11]	5
Figure 1-6 Pulse-echo technique diagram.....	5
Figure 1-7 Group velocity dispersion curves for a copper tube filled with air (a) and filled with water (b). A comparison between Disperse predictions (—) and experimental results (o, •) presented by [18].....	7
Figure 1-8 Phase velocity of the first five propagation modes in an aluminum tube of 2cm radius as a function of frequency [19].	8
Figure 1-9 Experimental setup for sound propagation studies performed by Lafleur in aluminum tube (a) and PVC tube (b). [20].....	9
2-1 Sound speed as a function of depth. The deep sound channel axis is between 600-1200 meters below the sea surface.[22]	12
2-2 Pulse-Echo general components diagram	13
2-3Experimental setup by Aristegui to excite axisymmetric modes along a fluid-filled pipe surrounded by a fluid [18].....	14
2-4 Waveform from Sturtevant’s Pulse-Echo system, where the initial pulse and two reflections are recorded [24].....	14
Figure 2-5 Portion of a tube with a change in cross-sectional area at $x=0$ from S_1 to S_2 , where an incident wave traveling towards $x=0$ is divided into a reflection wave and a transmitted wave.....	15
Figure 2-6 Two changes in cross-sectional area in a tube, where $S_1 > S_2$ creating a reflection with the same phase of the incident wave (Case 2) and $S_2 < S_3$ creating a reflection with the negative phase of the incident wave (Case 3).....	16
Figure 2-7 Rectangular and circular waveguides shapes.	19
Figure 2-8 Bessel functions of the first kind.....	21
Figure 2-9 Vibrating modes (m, n) of a circular membrane [15].....	22

2-10 Measurements of the Polaroid sonar used by M. Ihsan [27]. (a) Typical sonar echo after a bandpass filter is applied. (b) Average envelope functions of the echo produced by a plastic bottle at 100 cm from the sonar.	23
2-11 Average recognition accuracy as a function of distance using the envelope (solid line) and PSD (dashed line) [27].	24
2-12 Acoustic signatures of the ships Cornide de Saavedra (blue), Vizconde de Eza with keel down (green) and keel retracted (red). Speed 4 knots [30].	24
2-13 Framework used in acoustic signature recognition [29] and audio identification [31].	25
Figure 3-1 Block diagram of experimental device used to measure acoustic reflections in a water-filled tube.	26
Figure 3-2 Process to create an excitation pulse that will be sent through the hydrophone to the water-filled tube.	27
Figure 3-3 Acoustic pulse (a) created in MATLAB with its Fast Fourier Transform (b).	27
Figure 3-4 Reson TC4013 hydrophone used in the experiments as projector and receiver.	28
Figure 3-5 Functional block diagram (a) of the SPDT switch ADG419 and a top view of its pin configuration.	29
Figure 3-6 Reson VP-1000 signal amplifier and analog filter.	29
3-7 Connection diagram of the experimental setup used to record acoustic reflections of water-filled tubes.	30
Figure 3-8 Photo of the experimental setup used to create and record acoustic reflections produced by obstructed water-filled tubes made of copper, PVC and vinyl.	30
Figure 3-9 Flow chart of the algorithm for acoustic reflections signal preprocessing (blue), feature extraction (red) and signal matching (green).	31
Figure 3-10 Example of a reflection recorded by the pulse-echo measuring system in a water-filled copper tube of 2.54cm (1 inch) diameter and 1.3 meters long (a). The incident acoustic pulse is 20 μ s and 200 KHz of frequency. The reflection belongs to the water/air interface at the top-end of the tube (b).	32
Figure 3-11 FFT of the reflection raw data (a) and after the bandpass filter is applied (b) with cutoff frequencies of 100 KHz and 300 KHz.	33
Figure 3-12 Reflection signal of the water/air interface after the bandpass filter is applied.	33
Figure 3-13 Spectrogram of the filtered reflection signal of the water/air interface, where an increased in PSD is observed at 1.5 ms which belongs to the reflection and at 0 ms due to the electric crosstalk.	34
Figure 3-14 Projections of the spectrogram (Figure 3-11) frequency axis (a) and time axis (b) using Equation 3.3 and 3.4.	35
Figure 3-15 Three different tubes used for the experiments, (a) copper, (b) PVC and (c) vinyl.	37

Figure 3-16 Varying obstruction position along the water-filled copper tube.....	38
Figure 3-17 Stainless Steel obstructions used with different diameters.....	39
Figure 3-18 Delrin obstructions used with different diameters	39
Figure 3-19 Experimental setup for the measurements in water-filled vinyl tube varying obstruction location, size and density.	40
Figure 3-20 Stainless Steel and Delrin obstructions used for the 1.5 diameter vinyl tube.	41
Figure 4-1 Water-filled PVC tube used for the experiment and measurements. An 80% stainless steel obstruction is located at 75cm from the bottom part of the PVC tube where the hydrophone is located. ..	44
Figure 4-2 Acoustic reflections due to a 100% S.S. obstruction located at 60cm from the hydrophone. The incident pulse carrier frequency and duration was varied from (a) 20 μ s and 50 KHz, (b) 20 μ s and 100 KHz, (c) 10 μ s and 150 KHz, (d) 20 μ s and 200 KHz, (e) 10 μ s and 250 KHz, (f) 20 μ s and 300 KHz and (g) 30 μ s and 300 KHz.....	45
Figure 4-3 Reflection produced by a 100% S.S. obstruction in a water-filled PVC tube, located at 15cm (a), 55cm (b) and 95cm (c) from the hydrophone, using an acoustic pulse of 200 KHz with 20 μ s of duration. HACER UPDATE.....	46
Figure 4-4 Reflection Onset Detection example of a 100% S.S. obstruction located at 75cm from the hydrophone in the PVC tube. The onset detection measures the time when reflections overpasses the threshold limits, in this case results in 1.3ms.....	47
Figure 4-5 Calculated velocities using the onset detection algorithm and Equation 4.1. Each velocity belongs to a reflection produced by an obstruction located in the water-filled PVC tube.....	48
Figure 4-6 Error percentages of obstruction location measurements for 5 different obstruction sizes, using Onset Detection method with $\pm 0.04V$ threshold. The obstructions used were made of stainless steel and the sizes were 100% (blue line), 80% (red line), 60% (green line), 40% (violet line) and 20% (light blue line) from the 2.54cm diameter PVC tube.	49
Figure 4-7 Reflection of the 20% obstruction located at 80cm from the hydrophone in the PVC tube. The reflection at 1.25ms is produced by the obstruction, and the 1.5ms reflection is from the water/air interface at the distal end of the PVC tube. The thresholds are $\pm 0.06V$ (red line) and $\pm 0.04V$ (green line).	50
Figure 4-8 Reflection of the 20% obstruction located at 80cm from the hydrophone in the PVC tube. The reflection at 1.25ms is produced by the obstruction, and the 1.5ms reflection is from the water/air interface at the distal end of the PVC tube. The thresholds are $\pm 0.06V$ (red line) and $\pm 0.04V$ (green line).	51
Figure 4-9 Error percentages of obstruction location measurements for 5 different obstruction sizes, using Onset Detection method with $\pm 0.04V$ threshold. The obstructions used were made of stainless steel and the sizes were 100% (blue line), 80% (red line), 60% (green line), 40% (violet line) and 20% (light blue line) from the 2.54cm diameter PVC tube.	51
Figure 4-10 Spectrograms of an obstruction reflection of 20% size at 40cm (a) and 70cm (b) in a water-filled PVC tube using a 200 KHz and 20 μ s acoustic pulse.....	53

Figure 4-11 Spectrograms of an obstruction reflection of 20% (a) and 100% (b) size located at 60 cm from Hyd. in a water-filled copper tube using a 200 KHz and 20 μ s acoustic pulse. 53

Figure 4-12 Graph of the time axis projections of the Spectrogram for the S.S. obstruction sizes used (100% blue, 80% red, 60% green, 40% brown and 20% black). The time projection calculation was performed in MATLAB, cropping the electric crosstalk. At 1.3 ms an increased in the PSD is observed as expected for the water level of 1 meter from the Hyd. 54

Figure 4-13 Reflections Envelope (red line) of an S.S. obstruction reflection of 40% size at 40cm (a) and 70cm (b) in a water-filled PVC tube using a 200 KHz and 20 μ s acoustic pulse. The reflection that occurred at approx. at 1.3ms in both (a) and (b), belongs to the water/air interface at the distal end of the PVC tube. 55

Figure 4-14 Reflections Envelope (red line) of an S.S. obstruction reflection of 20% (a) and 100% (b) size located at 60cm in a water-filled PVC tube using a 200 KHz and 20 μ s acoustic pulse. The reflection that occurred at approx. at 0.75ms in both (a) and (b) belongs to the echo produced by the 20% and 100% obstructions. 56

Figure 4-15 Graph of the reflection envelopes for the S.S. obstruction sizes used (100% blue, 80% red, 60% green, 40% brown and 20% black). The reflections envelope was performed in MATLAB, cropping the electric crosstalk. At 1.3ms an increased in amplitude is observed as expected for the water level of 1 meter from the Hyd. 56

Figure 4-16 Spectrogram time axis projections of (a) S.S. and (b) Delrin obstructions located at 70cm in the PVC tube. Reflections produced by Delrin obstructions have a lower intensity that S.S. obstructions as expected, since the acoustic impedance of Delrin is lower than S.S. 57

Figure 4-17 Reflections Envelopes of (a) S.S. and (b) Delrin obstructions located at 70cm in the PVC tube. Reflections produced by Delrin obstructions have a lower intensity compared to S.S. obstructions as expected, since the acoustic impedance of Delrin is lower than S.S. 58

Figure 4-18 Process to create and stored the features database. 59

Figure 4-19 Comparison between the time axis projection feature of an unknown obstruction reflection and the reflections database. The reflection database presented is for S.S. obstructions located at 50cm from the hydrophone in the water-filled PVC tube. The unknown reflection (dashed blue line) is closest to the 100% S.S. obstruction (blue line), overlapping in the PSD peak, resulting on a Euclidian distance of 29.02. 60

Figure 4-20 Comparison between the envelope feature of an unknown obstruction reflection and the envelope reflection database. The reflection database presented is for S.S. obstructions located at 50cm from the hydrophone in the water-filled PVC tube. The unknown reflection envelope (dashed blue line) is closest to the 100% S.S. obstruction (blue line) resulting on a Euclidian distance of 4.02. 60

Figure 4-21 Prediction percentage of the Envelope Detection algorithm to recognize 100% S.S. obstruction at different locations along the water-filled PVC tube. Location predictions are plotted in the blue bar, size in the red bar and type in green bar. 61

Figure 4-22 Prediction percentage of the Time Projection algorithm to recognize 100% S.S. obstruction at different locations along the water-filled PVC tube. Location predictions are plotted in the blue bar, size in the red bar and type in green bar. 62

Figure 4-23 Histograms of the reflections processed by the Envelope Detection (a) and Time Projection (b) algorithms to detect 100% obstruction in the water-filled PVC tube. Ten reflections were recorded for each of the 16 positions along the PVC tube, resulting on 160 reflections processed by each algorithm. . 62

Figure 4-24 Obstruction position detection error using envelope detection (blue line) and Time Projection (green line) algorithms for 100% obstruction. Positive error values means overestimation of the real values and negative error values means underestimation. The error was zero for all locations, except for 85cm which was 5cm for both features. 63

Figure 4-25 Obstruction size detection error using envelope detection (blue line) and Time Projection (green line) algorithms for S.S. 100% obstruction. Standard deviations of each error are also presented. Time projection feature results on less error than the envelope feature to detect obstruction size. The overall error using the envelope feature was $-0.93 \pm 2.38 \%$ and for the time-axis projection was $-0.13 \pm 0.42 \%$ 64

Figure 4-26 80% S.S. Obstruction position detection error using envelope detection (blue line) and Time Projection (green line) algorithms for 80% S.S. obstruction. The error was zero for all locations, except for 85cm which was 5cm for both features. 65

Figure 4-27 80% S.S. Obstruction size detection error using envelope detection (blue line) and Time Projection (green line) algorithms. The overall error using the envelope feature was $-3.6 \pm 2.30 \%$ and for the time-axis projection was $-3.2 \pm 5.52 \%$. Time-axis projection feature shows slightly lower errors than the envelope feature as the obstruction distances increases but with higher standard deviations..... 65

Figure 4-28 60% S.S. Obstruction distance detection error using envelope detection (blue line) and Time Projection (green line) algorithms. The error was zero for all locations, except for 80cm with an error of 1 ± 3.16 cm for the envelope feature and at 85cm with an error 5cm for both features. 66

Figure 4-29 60% S.S. Obstruction size detection error using envelope detection (blue line) and Time Projection (green line) algorithms. The overall error using the envelope feature was $-2.8 \pm 0.98 \%$ and for the time-axis projection was $7.46 \pm 5.77 \%$ 66

Figure 4-30 40% S.S. Obstruction distance detection error using envelope detection (blue line) and Time Projection (green line) algorithms. As obstructions become smaller and farer from the hydrophone the error increases for both features. Average error using the envelope feature was 3.7 ± 1.38 cm and using time projection was 4.06 ± 1.38 cm. 67

Figure 4-31 40% S.S. Obstruction size detection error using envelope detection (blue line) and Time Projection (green line) algorithms. The overall error using the envelope feature was $6.26 \pm 2.23 \%$ and for the time-axis projection was $-7.73 \pm 6.16 \%$. As obstructions become smaller and farer from the hydrophone the error increases for both features..... 67

Figure 4-32 20% S.S. Obstruction distance detection error using envelope detection (blue line) and Time Projection (green line) algorithms. As obstructions become smaller and farer from the hydrophone the error increases for both features. Average error using the envelope feature was 4.06 ± 1.17 cm and using time projection was 4.26 ± 1.33 cm. 68

Figure 4-33 20% S.S. Obstruction size detection error using envelope detection (blue line) and Time Projection (green line) algorithms. The overall error using the envelope feature was $30.8 \pm 2.96 \%$ and for the time-axis projection was $1.33 \pm 6.65 \%$ 68

Figure 4-34 Algorithm accuracy using signal envelope and time-axis projection to detect stainless steel obstruction size, position and type in PVC tube. For 20% and 40% obstruction size the algorithm accuracy decreases due to similarity between reflections of small stainless steel obstructions and large Delrin obstructions..... 69

Figure 4-35 Average errors detecting S.S. obstructions position in water-filled PVC tube, using the envelope detection and time-axis projection. From 60cm onwards, the overall distance prediction error increases up to 8 ± 0.42 cm at 70cm. Both features results in similar error values detecting the S.S. obstructions positions along the PVC tube. 70

Figure 4-36 Average errors detecting S.S. obstructions position as function of obstruction size in water-filled PVC tube. For 40% and 20% S.S. obstructions, the average error detecting the obstruction position increases up to 4.26 ± 1.33 cm for 20% obstruction. Both features results in similar error values detecting the S.S. obstructions positions along the PVC tube. 71

Figure 4-37 Average errors detecting S.S. obstructions size in water-filled PVC tube, using the envelope detection and time-axis projection. The envelope detection average errors show that this method overestimates the obstruction size real value with an overall error of 5.94 ± 2.17 %. The time-axis projections method underestimates the obstruction size real value with an overall error of -3.36 ± 4.10 % 72

Figure 4-38 Average errors detecting S.S. obstructions size as function of obstruction size in water-filled PVC tube. For 40% and 20% S.S. obstructions, the envelope detection average error increases up to 30.8 ± 2.96 %. The time-axis projection average errors are lower, up to -7.46 ± 5.77 % for 60% S.S. obstruction..... 72

Figure 4-39 Algorithm accuracy using signal envelope and time-axis projection to detect Delrin obstruction size, position and type in PVC tube. The obstruction type (orange line) was estimated correctly using both methods. The obstruction position estimation accuracy (blue lines) decreases as the obstruction size decreases. For the obstruction size, it was estimated with an accuracy of at least 84.6% for 20% Delrin obstruction using the time-axis projection. 73

Figure 4-40 Average errors detecting Delrin obstructions position in water-filled PVC tube, using the envelope detection and time-axis projection. For distances of 70cm and closer, both algorithms underestimate the obstruction position up to -0.8 ± 1.68 cm at 40cm. And for distances over 70cm, both algorithms overestimates the obstructions position up to 1.8 ± 2.08 at 80cm using the envelope feature.. 74

Figure 4-41 Average errors detecting Delrin obstructions position as function of obstruction size in water-filled PVC tube. Both features results in similar error values detecting the Delrin obstructions positions along the PVC tube. The error increases up to 0.53 ± 1.12 cm as the obstruction size decreases at 20% size using the envelope feature. 75

Figure 4-42 Average errors detecting Delrin obstructions size in water-filled PVC tube, using the envelope detection and time-axis projection. For positions of 45cm and closer both methods underestimates the obstruction size up to -5% , and for 50cm to 90cm the obstruction size is overestimated up to 5% 76

Figure 4-43 Average errors detecting Delrin obstructions size as function of obstruction size in water-filled PVC tube. The time-axis projection results with less error in detecting the Delrin obstruction size in the PVC tube. Using both methods the error increases for 20% obstruction size, up to 5.46 ± 6.52 % using the envelope feature. 76

Figure 4-44 Reflection produced by an 100% S.S. obstruction in a water-filled copper tube, located at 15 cm (a), 55 cm (b) and 95 cm (c) from the hydrophone, using an acoustic pulse of 200 KHz with 20 μ s of duration. ****Hacer Update**** 77

Figure 4-45 Calculated velocities using the onset detection algorithm and Equation 4.1. Each velocity belongs to a reflection produced by an obstruction located in the water-filled copper tube..... 78

Figure 4-46 Algorithm accuracy using signal envelope and time-axis projection to detect S.S. obstruction size, position and type in copper tube. The obstruction type (orange line) was estimated with more accuracy using the signal envelope feature, while the time-axis projection decreases to 85.3% of accuracy for 20% obstruction. The envelope feature results with higher accuracy than time-axis projection, detecting the obstruction type, size and locations as function of S.S. obstruction size. 80

Figure 4-47 Average errors detecting S.S. obstruction position in water-filled copper tube, using the envelope detection and time-axis projection. As the obstruction position increases the average location error also increases, with a maximum error of -2.6 ± 5.97 cm at 90cm. Both methods show very similar error results. 80

Figure 4-48 Average errors detecting S.S. obstructions position as function of obstruction size in water-filled copper tube. Both methods show very similar error results, where the average error varies from -0.80 ± 1.92 cm for 100% S.S. obstruction to 1.06 ± 1.71 cm for 20% S.S. obstruction..... 81

Figure 4-49 Average errors detecting S.S. obstruction size in water-filled copper tube, using the envelope detection and time-axis projection. Time-axis projection results on higher errors detecting the obstruction size in the copper tube than using the signal envelope. 82

Figure 4-50 Average errors detecting S.S. obstructions size as function of obstruction size in water-filled copper tube. The signal envelope results on lower errors detecting the obstruction size than using time-axis projection. 82

Figure 4-51 Algorithm accuracy using signal envelope and time-axis projection to detect Delrin obstruction size, position and type in copper tube. The obstruction type (orange line) was estimated with an accuracy of 100% using the signal envelope feature, while the time-axis projection accuracy decreases for small Delrin obstructions. For the obstruction size and position estimation, the accuracy decrease as the obstruction size decreases. Signal envelope (solid lines) results with higher accuracy than time-axis projection, detecting Delrin obstructions type, size and position. 83

Figure 4-52 Average errors detecting Delrin obstruction position in water-filled copper tube, using the envelope detection and time-axis projection. As the obstruction position increases the average location error also increases, with a maximum error of -9.8 ± 12.41 cm at 90cm. Both methods show very similar error results. 84

Figure 4-53 Average errors detecting Delrin obstructions position as function of obstruction size in water-filled copper tube. Both methods show very similar error results, where the average error increases to 3.76 ± 2.69 cm for 60% and 1.73 ± 7.11 cm for 20% Delrin obstructions. 85

Figure 4-54 Average errors detecting Delrin obstruction size in water-filled copper tube, using the envelope detection and time-axis projection. As the obstruction distance increase the estimation error star to increase using both methods. 86

Figure 4-55 Average errors detecting Delrin obstructions size as function of obstruction size in water-filled copper tube. The signal envelope results on slightly lower errors detecting the obstruction size than using time-axis projection. 86

Figure 4-56 Experimental setup of the flexible Vinyl tubes configuration used for measurements. 87

Figure 4-57 Water-filled vinyl tube configuration surrounded by water with a layer of air in between. A 100 % Delrin obstruction located at 12cm from the hydrophone in the vinyl tube. 87

Figure 4-58 Reflection due to a 100% S.S. obstruction located at 9cm (a), 12cm (b) and 15cm (c) from the Hyd. in a 1cm diameter vinyl tube and using an acoustic pulse with frequency of 300 KHz and 20 μ s. 88

Figure 4-59 Calculated velocities using the onset detection algorithm and Equation 4.1. Each velocity belongs to a reflection produced by an obstruction located in the water-filled vinyl tube. The average propagation velocity found experimentally in the vinyl tube was 1312.7 m/s. 88

Figure 4-60 Algorithm accuracy using signal envelope and time-axis projection to estimate S.S. obstruction size, position and type in vinyl tube. The obstruction type (orange line) was estimated with accuracy over 95% using the signal envelope and time-axis projection feature. For the obstruction size and position estimation, the envelope results with higher accuracies than using the time-axis projection. 90

Figure 4-61 Average errors detecting S.S. obstruction position in water-filled vinyl tube, using the envelope detection and time-axis projection. As the obstruction position increases the average location error also increases, with a maximum error of -2.4 ± 2.57 cm at 30cm. Both methods show very similar error results. 91

Figure 4-62 Average errors detecting S.S. obstructions position as function of obstruction size in water-filled vinyl tube. Both methods show very similar error results, where the average error varies from -0.82 ± 1.43 cm for 60% S.S. obstruction to 0.9 ± 1.88 cm for 20% S.S. obstruction. 91

Figure 4-63 Average errors detecting S.S. obstruction size in water-filled vinyl tube, using the envelope detection and time-axis projection. As the obstruction position increases the average error and standard deviation estimating the obstruction size also increases, more notable using the time-axis projection. At 30cm the error using the time-axis projection was -5.2 ± 18.84 % and with the signal envelope -1.2 ± 6.23 % 92

Figure 4-64 Average errors detecting S.S. obstructions size as function of obstruction size in water-filled vinyl tube. The signal envelope results on lower errors detecting the obstruction size than using time-axis projection. As the obstruction size decreases the error increases up to 7 ± 11.24 % for the 20% S.S. obstruction using the time-axis projection 93

Figure 4-65 Algorithm accuracy using signal envelope and time-axis projection to estimate Delrin obstruction size, position and type in vinyl tube. The obstruction type (orange line) was estimated with accuracy of 100% using the signal envelope and over 95% using time-axis projection feature. For the obstruction size and position estimation, the envelope results with higher accuracies compared to the time-axis projection. 94

Figure 4-66 Average errors detecting Delrin obstruction position in water-filled vinyl tube, using the envelope detection and time-axis projection. As the obstruction position increases the average location error also increases, with a maximum error of -2.46 ± 3.60 cm at 30cm using time-axis projection. Signal envelope shows lower error estimating the Delrin obstruction position. 95

Figure 4-67 Average errors detecting Delrin obstructions position as function of obstruction size in water-filled vinyl tube. Both methods show similar error values except for 40% Delrin obstruction, where the time-axis projection error was 1.46 ± 2.34 cm and -0.5 ± 1.58 cm for the signal envelope. 95

Figure 4-68 Average errors detecting Delrin obstruction size in water-filled vinyl tube, using the envelope detection and time-axis projection. As the obstruction position increases the average error and standard deviation estimating the obstruction size also increases, more notable using the time-axis projection. At 30cm the error using the time-axis projection was -3.6 ± 27.1 % and with the signal envelope 2.8 ± 14.3 % 96

Figure 4-69 Average errors detecting Delrin obstructions size as function of obstruction size in water-filled vinyl tube. The signal envelope results on lower errors detecting the obstruction size than using time-axis projection. Time –axis projection error is higher for large and small Delrin obstructions. 97

LIST OF TABLES

Table 2-1 Inflection points of J_m	21
Table 3-1 Characteristic acoustic impedance of the water-filled tubes and obstructions used in the experiments. Taken from [36-39].	42
Table 4-1 Distance estimation using the v_{ave} calculated, the onset detection algorithm and Equation 4.2. The real and estimated distances were compared resulting in an error percentage of 2% or less and a difference of 1.2cm at most.	49
Table 4-2 Accuracy and overall errors using the signal envelope and time-axis projection to estimate obstructions type, size and position in water-filled PVC, copper and vinyl tubes. For the water-filled copper and vinyl tubes, the signal envelope was able to estimate the obstruction type, size and position with higher accuracy and lower error values. For the water-filled PVC tube, the envelope estimates better the position, while the time-axis projection the obstruction size and type.	98

CHAPTER 1

INTRODUCTION

1.1 Clinical Problem

Central venous catheters (CVCs) are narrow polymeric tubes used to provide medications to patients directly into the central venous system. Silicone is one the most commonly used materials for catheter construction because it is inert and non-reactive to body fluids and medications. For patients with chronic illnesses, CVCs provide easy venous access for laboratory tests (measure blood pressure), drug delivery (antibiotics and chemotherapy), and parenteral nutrition. CVCs stay in the body for longer periods of time than normal catheters [1], increasing the possibility of occlusions. Figure 1-1 shows a patient with a multiple-lumen CVC in the jugular vein.



(a)



(b)

Figure 1-1 Central venous catheter of three lumen in a patient jugular vein (a) and a catheter kit with the saline injections (b).

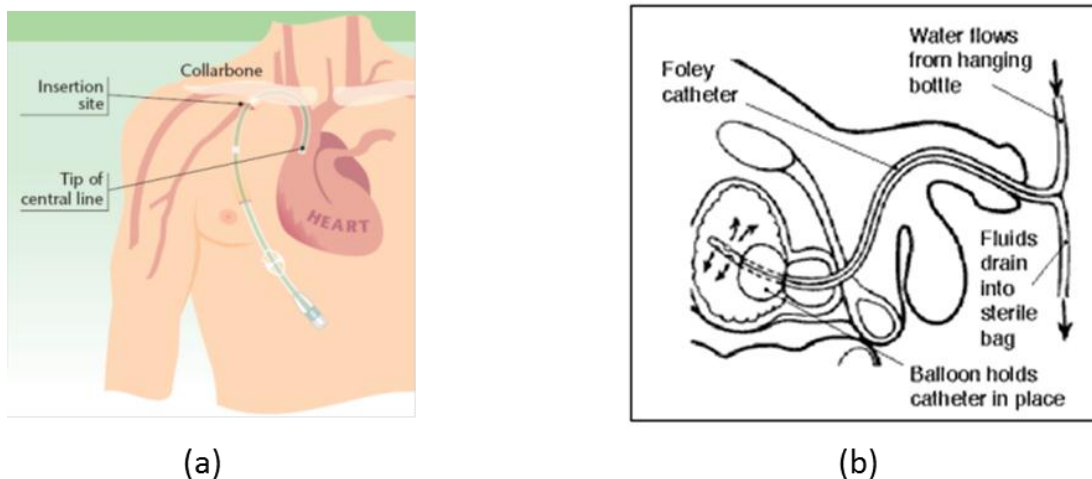


Figure 1-2 Example of a CVC insertion in the superior vena cava (a) and a Foley catheter for urinary extraction (b).

There are different types of catheters and uses for them. A Foley catheter is used to drain urine from the urinary bladder (Figure 1-2b). Peripheral venous catheters are used to provide medications and intravenous fluids (Figure 1-1a, Figure 1-2a), while insulin pumps are utilized to provide insulin or other medications subcutaneously. CVCDs are CVCs used to provide dialysis to patients, as Figure 1-3 shows, and umbilical line catheters to have quick access to central circulation of premature infants.

There are over 5 million CVCs used in the US and 30 million globally [2]. Approximately 25% of CVCs become occluded (blocked) through the deposition of blood clots inside the catheter lumen [3]. These occlusions result in the inability to remove blood for sampling and/or the inability to infuse medications through the catheter into the body. Replacements of occluded catheters result in medical complications for patients and can cost up to \$7,000 per patient [3]. At the time, there exist less than-optimum-methods to diagnose and prevent catheter occlusions. Catheter occlusions diagnostics currently includes the use of saline injections and X-ray. Preventive measures include the use of anticoagulant prophylactic drugs. All these methods are expensive, invasive, difficult to implement, toxic or do not provide sufficient information about the location, nature and severity of the obstruction. As CVCs are primarily inserted in patients receiving life-saving treatments (e.g. chemotherapy), it is critical to find accurate ways for early detection and diagnosis of occlusions. It is also relevant to diminish the use of expensive and toxic prophylactic anticoagulant drugs as a way to improve current treatment.



Figure 1-3 Example of a CVC in a patient receiving hemodialysis.

1.2 Actual Treatments for Occluded Catheters

Current methods for diagnosis and treatments for different types of CVC occlusion are presented next:

- a. *Saline Injections:* Physicians who want to assess the patency of a CVCD do so by injecting saline into the catheter. If there is an obstruction within the catheter's lumen, the physician will note that a higher pressure is required to maintain a specific flow. Although this method is simple, inexpensive and can be performed in the physician's office, it does not provide information about the location, nature or severity of the obstruction.
- b. *X-Rays Fluoroscopy:* If a more detailed assessment of the catheter is desired, then the patient is taken to the hospital and the catheter is examined using x-ray fluoroscopy and a radio opaque dye, as Figure 1-4 presents. This method provides accurate information regarding the severity and location of lumen or tip obstructions, but it is costly and time-consuming for the patient, and exposes the patient to undesired radiation.

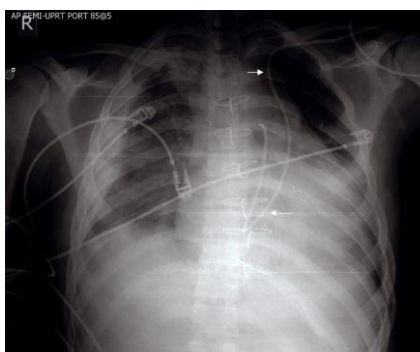


Figure 1-4 Chest X-Ray Fluoroscopy showing the Swan-Ganz catheter with its distal end in the proximal pulmonary artery. [4]

c. *Prophylactic drugs*: Use of drugs with anticoagulation (clot preventing) properties as a preventive measure against CVC occlusions. Two drugs are commonly used as prophylactic measure:

- 1) *Urokinase*: Produced by Microbix, Inc. Urokinase is a human enzyme synthesized by the kidney that directly converts plasminogen to active plasmin. Plasmin formed inside a thrombus by these activators allows them to lyse a thrombus from within. Treatment dosage with urokinase for CVC occlusion is needed to take place every 1-2 weeks in patients for several months. As with any drug, urokinase is expensive and has the potential of side effects, including dizziness, fever, headache, or nausea.
- 2) *CathFlo (Alteplase)*: Produced by Genentech, Cathflo Alteplase is administered for restoration of function to central venous access devices. Cathflo is a tissue plasminogen activator (t-PA) produced by recombinant DNA technology. In clinical trials, Cathflo's most serious adverse events reported after treatment were sepsis, gastrointestinal bleeding, and venous thrombosis [5].

1.3 Acoustic Pulse Reflectometry Method and Principles

Acoustic pulse reflectometry (APR) is a useful, non-invasive measurement method used to determine inner dimensions of ducts with varying cross-sectional area. APR consists on probing the system under investigation with short duration acoustic pulses. As the acoustic pulses travels along the duct, acoustic reflections will be produced due to changes in the duct's acoustic impedance. Reflections are then analyzed in order to determine the duct's composition and dimensions. This technique has been used more than 40 years, and since the 1980's for experiments in cylindrical tubes [6] exhibiting a great outcome. APR has been used from reconstruction of solid cylindrical cavities [7-8] based in the impulse response of a wind instrument [9], to estimation of tube wall compliance [10]. The instrumentation of an APR system plays an important role when recording reliable acoustic signals. The signal processing and analysis of acoustic reflections are vital to accomplish quantitative results. If APR is applied in fluid-filled pipes, the analysis of the acoustic reflections becomes more complex due to multiple propagation modes, velocities, etc.

1.3.1 Brief Summary of Sonar and Pulse-echo Technique

Sound Navigation and Ranging or Sonar, is a technique that uses sound propagation underwater for submarine navigation, communication or detection of other crafts. There are two types of sonar, passive and active. Passive sonar basically listens for sounds made by objects, while active sonar emits pulses of sound and listen for echoes. Sonar is normally used to measure the acoustic location (distance and direction) of an object and the echo characteristics of a target in the water.

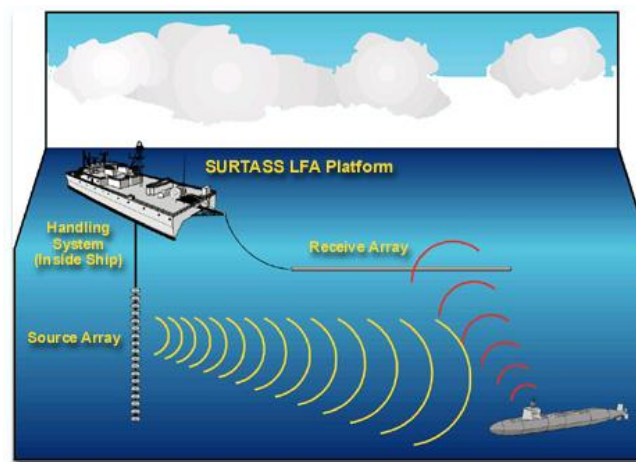


Figure 1-5 Example of the active sonar Surveillance Towed Array Sensor System (SURTASS) Low Frequency Active (LFA) used by the U.S. Navy. [11]

Within the active sonar there are several types of methods to transmit and received acoustic signals. Figure 1-5 presents the Pitch-Catch method, which uses one source array to transmit the acoustic signals and a receiver array. Other method utilized is the Pulse-Echo technique, showed in Figure 1-6, that uses only one acoustic transducer to transmit and received acoustic signals.

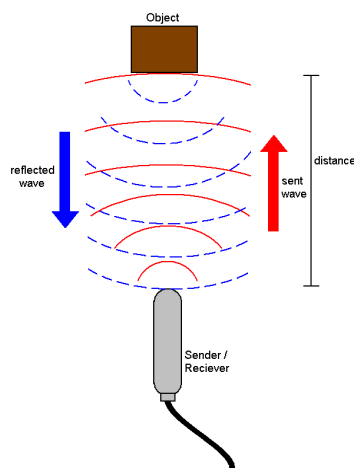


Figure 1-6 Pulse-echo technique diagram.

The objective of this thesis is to develop an algorithm to process and analyze acoustic reflections of obstructed water-filled tubes, which will be used as an analogy of obstructed CVCs. Moreover, the algorithm will provide accurate information about the obstruction location, severity and nature in the water-filled tube. The acoustic reflections will be measured and recorded using an experimental APR setup (Figure 3-1) in Pulse-Echo mode combined with acoustic signal analysis used in Sonar. The algorithms that are going to be developed in this work will be integrated to the next step of the overall investigation, which is the design of an acoustic reflectometer to determine obstructions in CVCs.

1.4 Acoustic Pulse Reflectometry Applications

1.4.1 Biological Applications

Applying acoustic reflectometry to a biological scenario is comparable to the air and liquid-filled tubes problem, since most of the body cavities, such as veins, arteries, respiratory and urinary conducts, have a cylindrical shape. Medical devices like catheters, infusion pumps and breathing tubes [12] can be monitored using this type of technique, to detect obstructions in the lumen or tip of the device. Applications of acoustic reflectometry in the medical devices field could help minimize surgical interventions in patients and add the flexibility of continuous monitoring of their implantable devices. An example of a device that implements acoustic reflectometry method for diagnosis is Ear Check PRO, a device that identifies the presence or absence of Otitis media (infection of the middle ear) with the use of sound waves [13]. APR is also used by the SonarMed Airway Monitoring System [14] which consists in a real-time monitoring system of breathing tubes position and obstructions. Another example is ultrasound imaging, which analyzes acoustic reflections to produce images of organs, vessels, arteries, etc.

1.4.2 Other Applications

Pipeline systems are widely used in oil, gas and chemical industries to provide essential utilities to society (i.e. potable water, petroleum, natural gas, etc.). Most of these pipelines are located underground, requiring expensive monitoring systems to ease in their maintenance. Leakage and blockage detection at these system's tubing is a main concern, since the tube quality is crucial in the production and

safety of any of the industries mentioned previously [15]. Numerous methods have been proposed to monitor pipelines, such as acoustic detection methods, radar and tracer techniques, etc. Recent work proposed by K. A. Papadopoulou *et al.*, evaluated the use of acoustic reflectometry for leakage and blockage detection [16] applied to pipelines filled with natural gas. Papadopoulou was able to detect leakages and blockage as small as one per cent of the pipeline diameter [16].

1.5 Previous Work in Air and Liquid Sound Propagation

There are different studies that investigate how acoustic waves travel in cylindrical waveguides filled with gas or liquid. M.J.S. Lowe [17] has studied defect detection in air and water filled pipes surrounded by liquid and air using guided waves. Lowe's studies also involved acoustic propagation modes properties due to the excitation source frequency. As a result of these studies, the computer software *Disperse* was developed by Lowe *et. al.* at the Imperial College. This software predicts the dispersion curves of systems with either flat or cylindrical geometries, having an arbitrary number of layers. Figure 1-7 shows a comparison of the group velocities for the different propagation modes between a copper tube filled with air (a) and water (b), performed by Aristegui and Lowe [18]. It is observed that in the water-filled tube more propagation modes are generated compared to the air-filled tube.

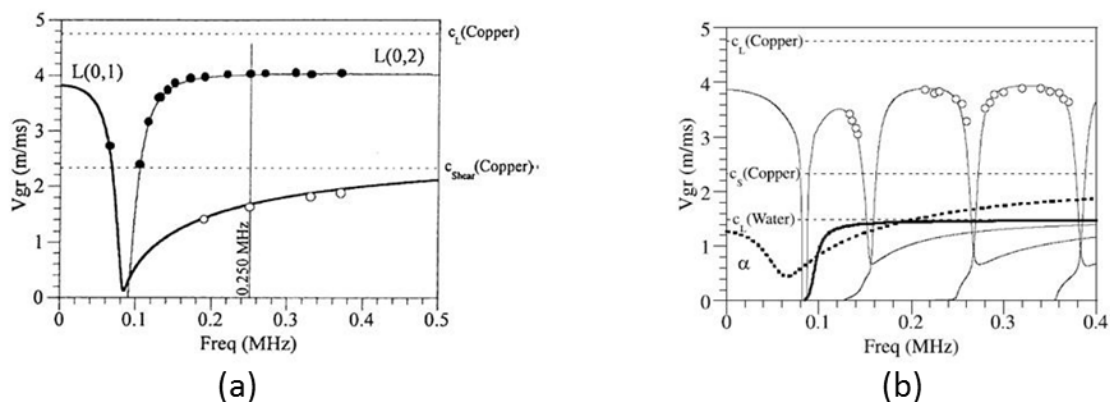


Figure 1-7 Group velocity dispersion curves for a copper tube filled with air (a) and filled with water (b). A comparison between Disperse predictions (—) and experimental results (o, •) presented by [18].

Another acoustic propagation study in cylindrical elastic tubes, similar to Lowe's research was performed by Elvira-Segura [19N]. This study consisted of comparing different numerical propagation theories, such as Weston, Kirchhoff and general theory, to calculate experimental phase velocity and attenuation coefficients. Elvira-Segura also studied how the phase velocity and attenuation of propagation modes change by varying the water-filled tube diameter. Figure 1-8 presents the phase velocity calculated using general theory in an aluminum tube of 2cm radius.

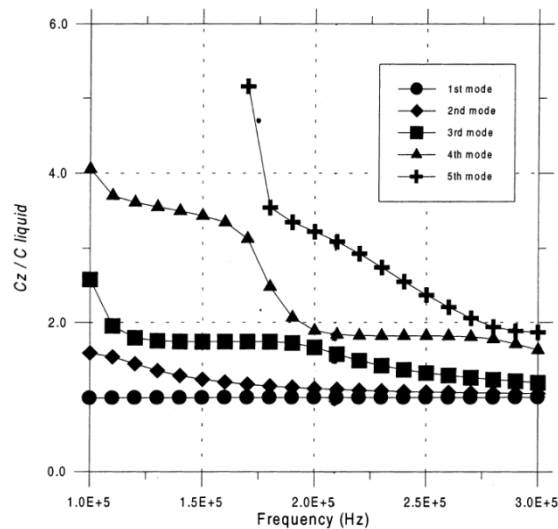


Figure 1-8 Phase velocity of the first five propagation modes in an aluminum tube of 2cm radius as a function of frequency [19].

Elvira-Segura based his analytic work in different theories; one of these was performed in the 1990's by L. Dywnn Lafleur [20]. Lafleur studied the propagation modes of liquid-filled elastic waveguides. Analytic equations for sound propagation were solved to obtain the dispersion and phase velocity curves of aluminum and PVC water-filled tubes. The experimental setup used by Lafleur to study sound propagation in different tubes is presented in Figure 1-9.

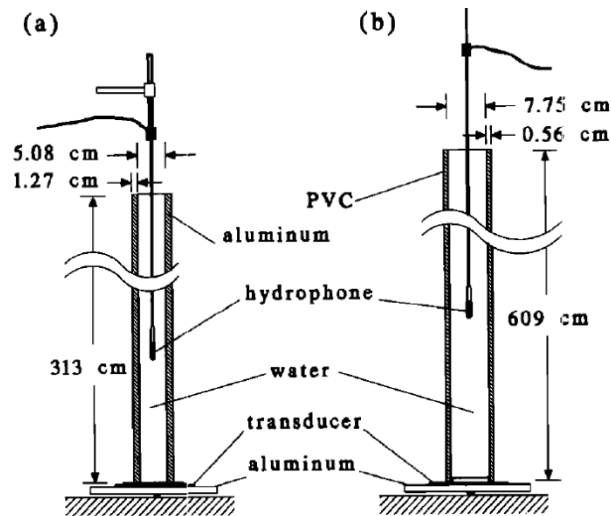


Figure 1-9 Experimental setup for sound propagation studies performed by Lafleur in aluminum tube (a) and PVC tube (b). [20]

1.6 Objectives

The main objective of this research is to develop the algorithms necessary to determine obstruction position, severity and nature, in water-filled tubes. An acoustic reflectometry system, operated in pulse-echo mode, was designed to record acoustic reflections in liquid-filled tubes. These waveforms were processed and analyzed in MATLAB, where an algorithm was developed to determine the position, size and nature of the obstruction. The experiments were performed in water-filled tubes made of copper, PVC or vinyl, and surrounded by water for vinyl tube. Since these tubes have different diameter sizes, the frequency of the incident pulse was changed to achieve wave propagation along the tubes. Signal processing techniques such as onset detection, spectrograms and envelope detection was performed in different frequency ranges to achieve the obstruction characterization in the mentioned tubes configuration. The specific objectives are:

1. Develop an algorithm to detect obstructions in water-filled tubes made of copper, PVC or vinyl.
2. Locate obstruction position within a tube lumen with a precision of ± 5 mm.
3. Determine obstruction size with a precision of 20%.
4. Identify the nature (discrete values of density) of lumen obstructions.

1.7 Outline

The chapters of this document are organized as follows:

Chapter 1 presents the importance of defect detection in industry, the use of acoustic reflectometry to achieve defect detection and how this method can be employed in biological applications. Chapter 1 also presents a brief description of previous studies on sound propagation in liquid-filled tubes and Sonar techniques. The motivation and objectives for this work are also established in this chapter. Chapter 2 presents the theoretical background of sound propagation in waveguides, reflections in lossless and lossy tubes and propagations modes in circular waveguides. It also outlines the sonar and pulse-echo technique along with the signal processing used for object recognition. Chapter 3 describes the pulse-echo experimental setup constructed to transmit short acoustic pulses into water-filled tubes, to record obstruction reflections and how these are processed in MATLAB using a signal processing framework utilized in object recognition. Chapter 3 also explains the experimental procedure performed in water-filled PVC, copper and vinyl tubes. Chapter 4 presents the results obtained using the signal envelope and time-axis projection to estimate obstructions position, size and type, located in water-filled PVC, copper and vinyl tubes. It also presents a comparison between the accuracy and average errors using the signal envelope and time-axis projection to estimate the obstructions position, size and type for each tube. Chapter 5 states the conclusions and recommendations based on this research.

CHAPTER 2

THEORETICAL BACKGROUND

The purpose of this chapter is to present the sonar technique and how it is used for object recognition in underwater applications by means of a pulse-echo system. This chapter also provides theoretical background in acoustics, sound propagation and acoustic reflections in waveguides. The first part of the chapter presents the concepts and previous work in sonar and pulse-echo technique. The second part introduces the general principles of acoustic reflections and sound propagation in waveguides. The last part presents the signal processing methods and framework used for object and acoustic waveforms recognition.

2.1 Sonar and Pulse-Echo Technique

Some animals, like dolphins and bats, have used sound for communication and object detection over thousands of years. The use of sound by humans to detect underwater objects was initially studied by Leonardo Da Vinci in 1490 [21] where a tube inserted into the water was used to hear ships at long distances. Since then, many patents and technologies have been developed using acoustic waves to detect underwater objects. Sonar is used in military applications such as, anti-submarine warfare, mine applications and ship identification, while Sonar non-military applications include animal research, ocean current mapping, drilling applications, etc.

Sonar is affected by the variations of the sound speed, which is determined by the water's bulk modulus and mass density. The bulk modulus is altered by water temperature, impurities and pressure. For example, in fresh water sound travels more slowly than in sea water, and higher pressure increases the sound speed. There exists a channel in the deep ocean, called SOFAR channel (Sound Frequency and Ranging channel) or deep sound channel, where the vertical sound speed profile is minimal, as Figure 2-1

presents, acting as a waveguide for sound that is caused by changes in the water density. The deep sound channel provides extremely low propagation losses resulting on sound waves traveling within the channel thousands of miles before dissipating.

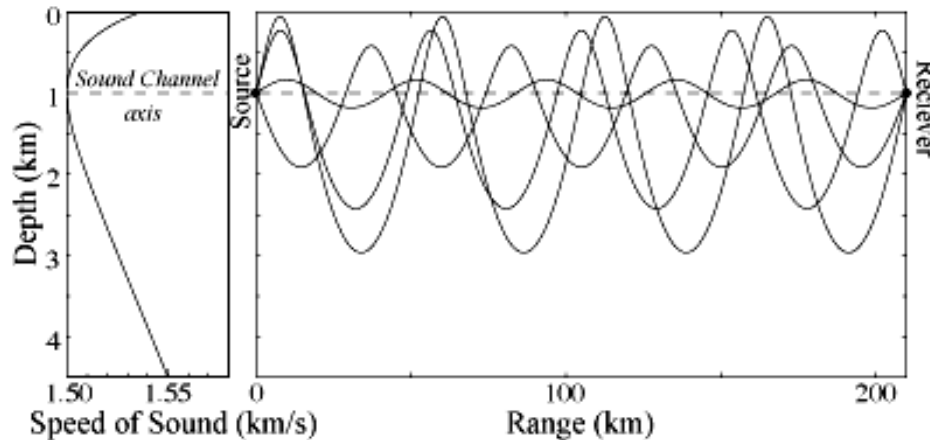


Figure 2-1 Sound speed as a function of depth. The deep sound channel axis is between 600-1200 meters below the sea surface.[22]

A common type of sonar is the active sonar, which uses a sound transmitter and a receiver. If both are located in the same place it is a monostatic operation, but if they are separated it is a bistatic operation. Figure 1-6 presents an example of active sonar that creates pulses of sound and listens for reflections of the pulse produced by an object. This type of system that uses only one transducer to receive and transmit pulses is also called Pulse-Echo system. The pulses are created using a signal generator, amplifier and an acoustic transducer. Figure 2-2 shows the components of a Pulse-Echo system. The signal generator creates the incident pulse at a determined pulse width, carrier frequency, modulation and amplitude. The transducer should be able to transmit and receive acoustic signals. The receiver/transmitter switch simply toggles the connection of the transducer to receiver and transmitter channel. Finally, the receiver channel amplifies and filters the reflection signal in order to display it on a monitor, to then be analyzed using digital signal processing techniques.

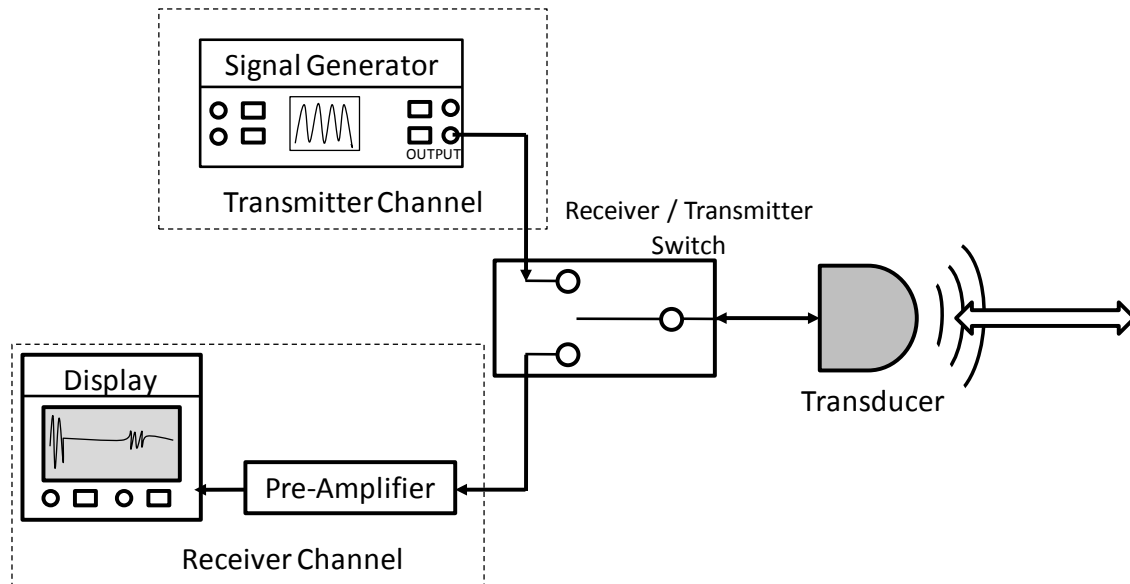


Figure 2-2 Pulse-Echo general components diagram.

Pulse-Echo technique is a common measurement method used in underwater applications. In an experiment by R. Martinez *et. al.*, a comparison between Pulse-Echo and Through-Transmission technique was performed to measure ultrasonic attenuation in pure water [23]. Attenuation measurements in distilled and degasified water were made using both techniques at 1 MHz and 25°C, resulting on similar attenuation coefficients at long distances from the transducers. Aristegui [18] also used an experimental setup using the Pulse-Echo technique to guide waves in fluid-filled pipes surrounded by different fluids. Figure 2-3 presents this setup where a copper pipe is inside a Perspex pipe and both pipes are filled with fluids, resulting on a copper pipe filled and surrounded by a fluid. A Pulse-Echo measurement example, performed by B. T. Sturtevant, is presented in Figure 2-4. Sturtevant used the Pulse-Echo technique to measure the bulk acoustic wave phase velocity and the importance of piezoelectric couplant.

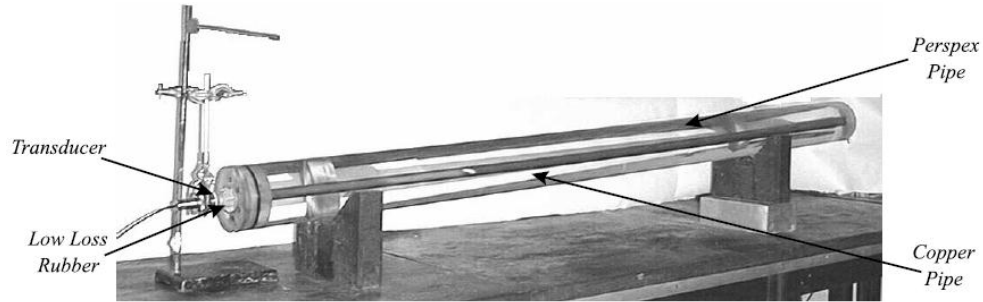


Figure 2-3 Experimental setup by Aristegui to excite axisymmetric modes along a fluid-filled pipe surrounded by a fluid [18].

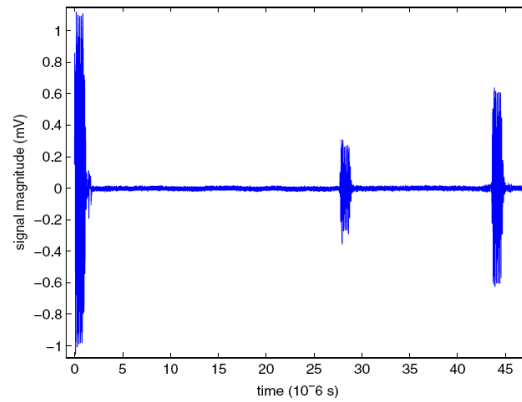


Figure 2-4 Waveform from Sturtevant's Pulse-Echo system, where the initial pulse and two reflections are recorded [24].

2.2 Reflections in Lossless Rigid Tubes

A reflection wave is produced when a sound wave travels along a tube and reaches a change in acoustic impedance Z . The acoustic impedance is defined as the ratio of acoustic pressure in Pa to volume velocity in m^3/s

$$\mathbf{Z} = \frac{p}{U} \left[\frac{\text{Ns}}{\text{m}^5} \right] \quad (2.1)$$

For plane waves traveling in rigid lossless tubes the acoustic impedance is equal to the characteristic impedance of the tube

$$\mathbf{z}_0 = \frac{\pm \rho_0 c}{S} \quad (2.2)$$

where ρ_0 is the density of the fluid, c is the wave propagation velocity, S is the cross sectional area of the tube, and the \pm sign depends on the propagation direction of the wave.

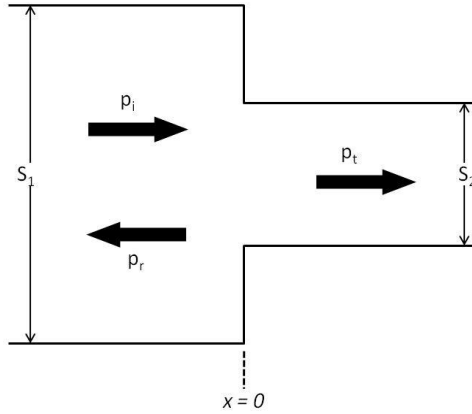


Figure 2-5 Portion of a tube with a change in cross-sectional area at $x=0$ from S_1 to S_2 , where an incident wave traveling towards $x=0$ is divided into a reflection wave and a transmitted wave.

Equation 2.2 shows that a variation in cross sectional area (S) will produce a change in acoustic impedance resulting in an acoustic reflection. Figure 2-5 shows an incident wave p_i traveling along the tube with cross sectional area S_1 , and reaches a change in cross sectional area (S_1 to S_2). In this point $x=0$, p_i generates a reflection wave p_r which travels in the opposite direction of the incident wave and a transmitted wave p_t that keeps traveling along the cross sectional area S_2 .

There are two conditions that must be satisfied for all times and points in a boundary: continuity of pressure and continuity of normal velocity [25]. First, continuity of pressure means that the acoustic pressures in both sides of the boundary are equal, and continuity of normal velocity states that the particle velocities normal to the boundary are equal as well. The boundary condition that represents continuity of pressure and normal particle velocity is,

$$p_i(x_0, t) + p_r(x_0, t) = p_t(x_0, t), \quad \text{at } x = 0 \quad (2.3)$$

$$u_i(x_0, t) - u_r(x_0, t) = u_t(x_0, t), \quad \text{at } x = 0 \quad (2.4)$$

To calculate the reflection coefficient Equation 2.3 and 2.4 were substituted in Equation 2.1, resulting in

$$R(x_0) = \frac{p_r}{p_i} = \frac{z_1 - z_2}{z_1 + z_2} \quad (2.5)$$

If the fluid inside the tube is the same (equal $\rho_0 c$ along the tube), Equation 2.5 can be simplified to

$$R(x_0) = \frac{p_r}{p_i} = \frac{S_1 - S_2}{S_1 + S_2}, \quad (2.6)$$

showing that is function of the cross sectional area of both sides of the tube.

Analyzing Equation 2.6, there can be three different tube configuration cases. First $S_1 = S_2$ (tube with the same cross sectional area), resulting in a reflection coefficient $R = 0$. Second, $S_1 > S_2$ where the cross sectional area of the tube decreases (large to small configuration). This will result in a positive reflection coefficient, which can be visualized as a scaled version of the incident wave (same phase as the incident pulse). Finally the third case is $S_1 < S_2$, where the cross sectional area of the tube increases. Opposite to the second case, this will result in a negative reflection coefficient, which means a scaled version of the incident pulse, but inverted in amplitude.

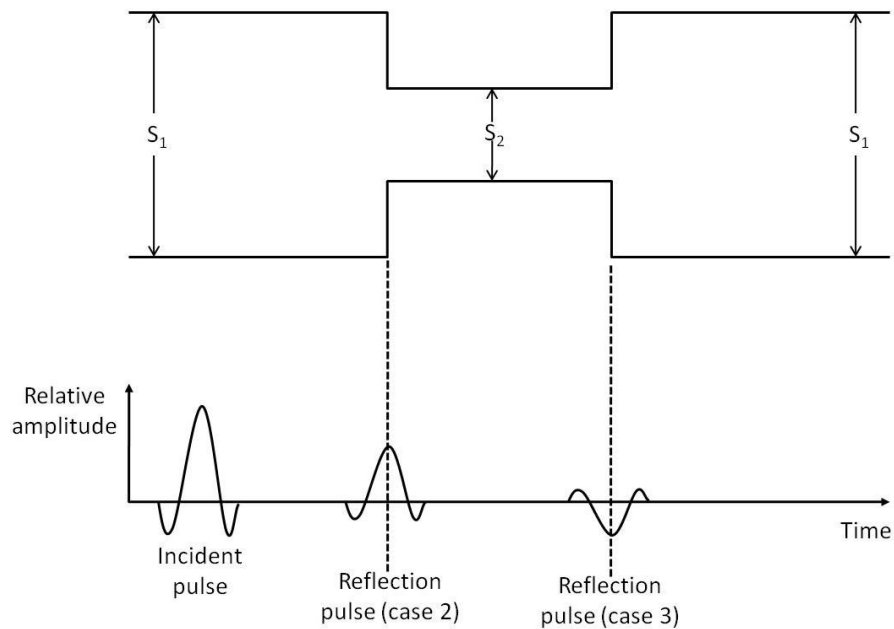


Figure 2-6 Two changes in cross-sectional area in a tube, where $S_1 > S_2$ creating a reflection with the same phase of the incident wave (Case 2) and $S_2 < S_3$ creating a reflection with the negative phase of the incident wave (Case 3).

2.3 Acoustic Losses in Rigid Tubes

In the previous section no dissipation of acoustic energy was considered. When losses are not considered the pressure amplitude and wave phase velocity remains constant. In some situations dissipation takes place very slowly and can be ignored, but its nature and mathematical formulation will now be discussed.

Acoustic dissipation can be divided into losses in the medium and at the boundaries of the medium. The losses in the medium are primarily due to viscous and heat conduction losses. These losses are called absorption processes, and are characterized by a relaxation time (τ), which measures the elapsed time for a process to be completed. If the acoustic pressure (p) and the condensation (s) are in phase, acoustic losses are ignored and the equation that states its relationship is

$$p = \rho_0 c^2 s \quad (2.7)$$

Now acoustic losses are considered and Equation 2.7 is modified to introduce a delay time between a change in pressure and equilibrium condensation [25], resulting in

$$p = \rho_0 c^2 \left(1 + \tau \frac{\partial}{\partial t}\right) s \quad (2.8)$$

as first stated by Stokes.

Using the relaxation time, the wave equation is rewritten as

$$\left(1 + \tau \frac{\partial}{\partial t}\right) \nabla^2 p = \frac{1}{c^2} \frac{\partial^2 p}{\partial t^2} \quad (2.9)$$

And, for harmonic acoustic waves, as

$$(\nabla^2 + \mathbf{k}^2)p = 0 \quad (2.10)$$

where

$$\mathbf{k} = \frac{\omega}{c} \frac{1}{\sqrt{1+j\omega\tau}} \quad (2.11)$$

For a plane wave traveling in the + x direction we have

$$p = P_0 e^{j(\omega t - kx)} \quad (2.12)$$

where P_0 is the pressure amplitude at $x=0$.

Introducing losses in the wave number equation, it is rewritten as,

$$\mathbf{k} = k - j\alpha \quad (2.13)$$

where α is the absorption coefficient. Combining equations 2.11 and 2.13, gives

$$\alpha = \frac{\omega}{c} \frac{1}{\sqrt{2}} \left[\frac{\sqrt{1+(\omega\tau)^2}-1}{1+(\omega\tau)^2} \right]^{1/2} \quad (2.14)$$

$$k = \frac{\omega}{c} \frac{1}{\sqrt{2}} \left[\frac{\sqrt{1+(\omega\tau)^2}+1}{1+(\omega\tau)^2} \right]^{1/2} \quad (2.15)$$

where a dependency in frequency (ω) is observed.

Replacing \mathbf{k} of Equation 2.14 in 2.12, a propagation wave with losses is obtained,

$$p = P_0 e^{-\alpha x} e^{j(\omega t - kx)} \quad (2.16)$$

with a wave phase speed of

$$c_p = \frac{\omega}{k} \quad (2.17)$$

Substituting Equation 2.16 in 2.18, wave phase speed results in

$$c_p = c\sqrt{2} \left[\frac{1+(\omega\tau)^2}{\sqrt{1+(\omega\tau)^2}+1} \right]^{1/2} \quad (2.18)$$

which reveals that c_p is function of frequency also known as a dispersive propagation. Equation 2.17 shows that as a wave travels a farther distance its amplitude decays by $P_0 e^{-\alpha x}$. Since wave propagation in fluid-filled tubes has different propagation modes, each one has a specific phase velocity and acoustic losses.

2.4 Sound Propagation in Waveguides with Constant Cross Sectional Area

Propagation of acoustic waves in confined boundaries exhibits great complexity due to different reasons such as the frequency range in which sound propagates, different propagation modes, velocity and attenuation of each mode, etc. These confined boundaries are known as waveguides. A waveguide is a physical structure to guide sound waves, i.e. ducts, pipes, tubes, etc.

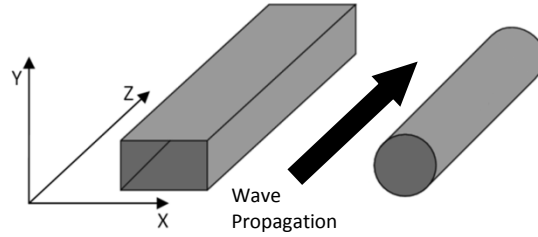


Figure 2-7 Rectangular and circular waveguides shapes.

Considering a rectangular waveguide with constant cross sectional area (Figure 2-7) and assuming the side walls to be rigid, if an acoustic source is located at $z = 0$, the absence of a boundary in the z direction allows the acoustic energy generated by the source to travel along the waveguide. With these assumptions established an appropriate solution for the acoustic pressure is

$$p_{lm} = A_{lm} \cos k_{xl}x \cos k_{ym}y e^{j(\omega t - k_z z)} \quad (2.19)$$

where,

$$\left(\frac{\omega}{c}\right)^2 = k^2 = k_{xl}^2 + k_{ym}^2 + k_z^2 \quad (2.20)$$

and,

$$k_{xl} = \frac{l\pi}{L_x}, \quad l = 0, 1, 2, \dots \quad (2.21)$$

$$k_{ym} = \frac{m\pi}{L_y}, \quad m = 0, 1, 2, \dots \quad (2.22)$$

From Equation 2.21 it can be easily seen that

$$k_z = \sqrt{\left(\frac{\omega}{c}\right)^2 - k_{xl}^2 - k_{ym}^2} \quad (2.23)$$

In Equation 2.20, ω can have any value, so p_{lm} is a solution for all values of ω [25]. The transverse component k_{ml} for this rectangular waveguide is defined as

$$k_{ml} = \sqrt{k_{xl}^2 + k_{ym}^2} \quad (2.24)$$

With this transverse component defined, Equation 2.24 can be rewritten as

$$k_z = \sqrt{\left(\frac{\omega}{c}\right)^2 - k_{ml}^2} \quad (2.25)$$

In order to have wave propagation in the positive z direction, ω/c needs to be greater than k_{ml} , making k_z real. The eigenfunction associated to a specific k_{ml} is called a propagation mode. The cutoff frequency of a propagation mode (l, m) is given by the limit where k_{ml} remains real,

$$\omega_{lm} = ck_{ml} \quad (2.26)$$

If the excitation frequency is lower than the cutoff, k_z has an imaginary value. This mode is called an evanescent mode, which means that no energy or not an appreciable energy is propagated along the waveguide. From Equation 2.20 is seen that for a particular mode the phase velocity and group velocity are

$$c_p = \frac{\omega}{k_z} = \frac{c}{\sqrt{1 - \left(\frac{k_{lm}}{k}\right)^2}} = \frac{c}{\sqrt{1 - \left(\frac{\omega_{lm}}{\omega}\right)^2}} \quad , \quad (2.27)$$

$$c_g = c \sqrt{1 - \left(\frac{\omega_{lm}}{\omega}\right)^2} \quad (2.28)$$

The group speed indicates how fast the energy of a wave propagates in the z direction.

Applying this theory of rectangular waveguides to circular waveguides of radius $r = a$ results in

$$p_{lm} = A_{lm} J_m(k_{lm}r) \cos(m\theta) e^{j(\omega t - k_z z)} \quad (2.29)$$

where r, z, θ are the cylindrical coordinates and J_m the m order Bessel function. After finding the values of k_{ml} , all the equations developed for a rectangular waveguide can be used by substituting k_{ml} for the circular waveguides presented in the next section. The values of j'_{ml} can be found at Bessel Functions Tables to calculate the cutoff frequencies for the different propagation modes (l, m) of a pipe of radius a .

2.5 Bessel Functions

The solutions of the differential equation

$$\left[x^2 \frac{d^2}{dx^2} + x \frac{d}{dx} + (x^2 - n^2) \right] f(x) = 0 \quad (2.30)$$

are the Bessel functions of the first kind $J_n(x)$ for all x , and Bessel functions of the second and third kind for all x greater than zero. These are oscillating functions whose amplitude decrease as x increases.

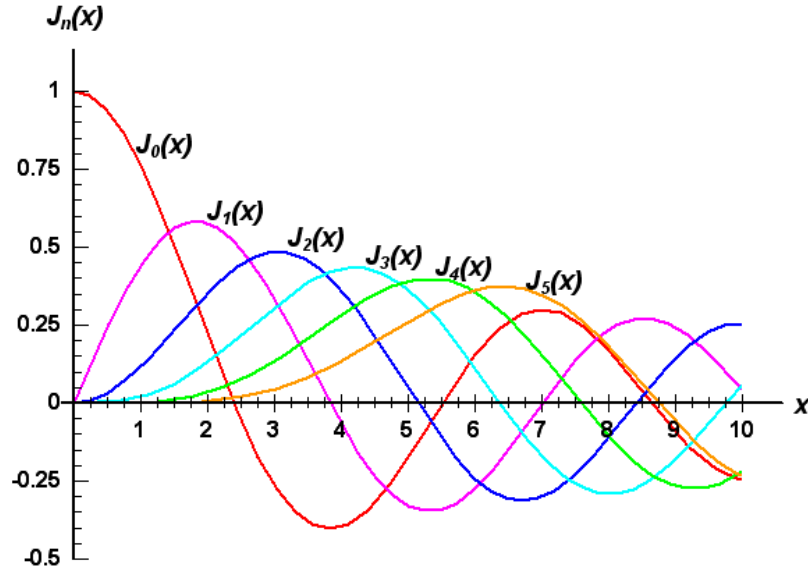


Figure 2-8 Bessel functions of the first kind.

Equation 2.30 is a general solution of the three-dimensional acoustic wave equation in cylindrical coordinates where J_m is the m order Bessel function. Another useful property of the Bessel function is its inflection points, which are used to calculate the cutoff frequencies of the different propagation modes explained in the next section.

Table 2-1 Inflection points of J_m

$$j'_{mn}$$

m \ n	1	2	3	4	5
0	0	3.83	7.02	10.17	13.32
1	1.84	5.33	8.54	11.71	14.86
2	3.05	6.71	9.97	13.17	16.35
3	4.20	8.02	11.35	14.59	17.79
4	5.32	9.28	12.68	15.96	19.20
5	6.41	10.52	13.99	17.31	20.58

2.6 Propagation Modes

To determine the cutoff frequencies of the propagation modes for circular waveguides, the transverse component is redefined as

$$k_{ml} = \frac{j'_{ml}}{a} \quad (2.31)$$

where j'_{ml} are the zeros of dJ_m . The cutoff frequency now is,

$$\omega_{lm} = j'_{ml} \frac{c}{a} \quad (2.32)$$

It can be observed that when the frequency increases, more modes propagate along the waveguide, causing acoustic energy to travel at different velocities, as each mode has a propagation velocity, and consequently complicating the analyses of reflections of the waveguide. On the other hand, when a low frequency is applied by the source, the modes that travel in the z direction are plane waves due to rigid boundaries. An example of vibration modes in a circular membrane is shown in Figure 2-5, labeled by the pair (m, n) . The integer m indicates the number of radial nodal lines and n the number of azimuthal nodal lines. Also, the modes are grouped by their shapes, such as longitudinal, transverse or plate.

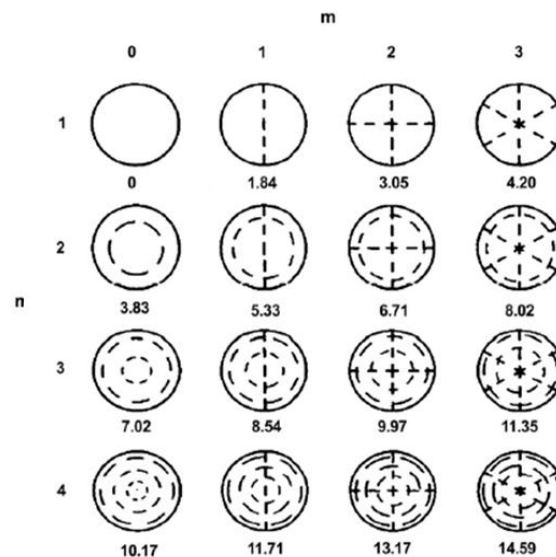


Figure 2-9 Vibrating modes (m, n) of a circular membrane [15].

2.7 Acoustic Signal Processing

One of the most common applications of sonar and radar is to locate the position of a particular object. This is achieved by transmitting a short acoustic pulse and measuring the time it takes for the reflection to return. The object distance will be one half the product of the signal round trip and the speed of the signal. Figure 1-6 shows an example of how the acoustic pulse travels from the transducer to the object and the reflection towards the transducer. The Pulse-Echo technique is frequently used in this type of measurements.

Object detection and recognition using underwater sonar images is a key technology [26]. The analysis of the sonar images are based in feature selection and extraction. The purpose of features selection is to find noticeable characteristics to differentiate an object from other. Thus, features extracted from similar objects should be very alike while features of different object should be reasonably distinct.

An object recognition experiment performed by M. Ihsan consists in extracting the average envelope, as shown in Figure 2-10, of the time-domain reflection generated by a plastic bottle at 100cm from the sonar [27]. A fuzzy ARTMAP neural network was utilized to recognize and classify the objects at varying distances using the average envelope. M. Ihsan also extracted the average PSD of the reflection as a feature to be also used in the recognition and classify process. Figure 2-11 presents the accuracy of the Ihsan's recognition algorithm as a function of distance.

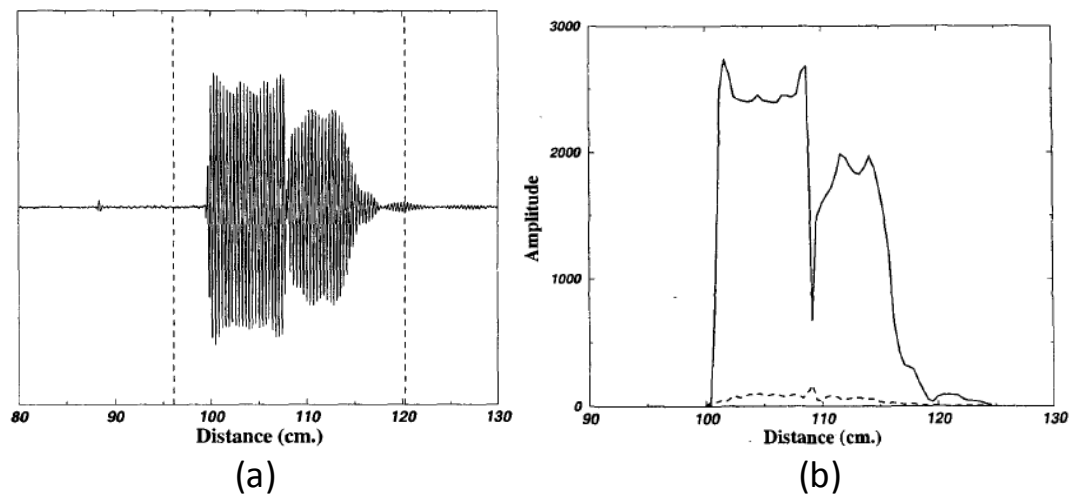


Figure 2-10 Measurements of the Polaroid sonar used by M. Ihsan [27]. (a) Typical sonar echo after a bandpass filter is applied. (b) Average envelope functions of the echo produced by a plastic bottle at 100 cm from the sonar.

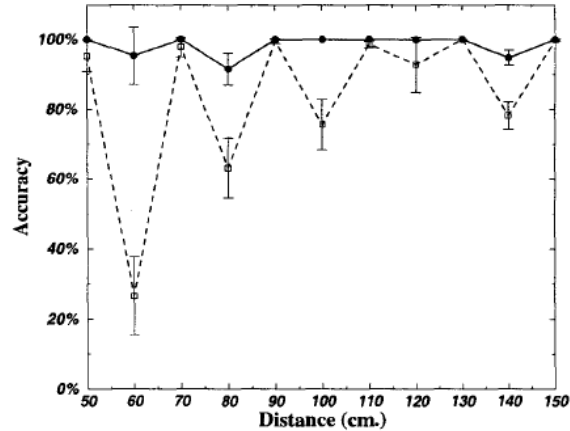


Figure 2-11 Average recognition accuracy as a function of distance using the envelope (solid line) and PSD (dashed line) [27].

2.7.1 Acoustic Signature and Recognition Framework

The technique used to recognize vehicle, submarines and ships by the sound they make, is known as acoustic signature. The acoustic signature describes a combination of acoustic emissions, such as, noise generated by engines, fuel pumps, air conditioning systems, propeller shafts or noise generated by the movement of water displaced by a moving vessel. These emissions depends on the vehicle dimensions, machinery and displacement, therefore different vehicles will have different acoustic signatures. In modern naval mines, such as the CAPTOR mine [28], this technique is used to distinguish the acoustic signatures between friendly vessels and possible enemy vessels. Studies performed by Mario Munich [29] and Salvador Santiago [30], used acoustic signatures to recognize nine different ground vehicles and two oceanographic ships, respectively.

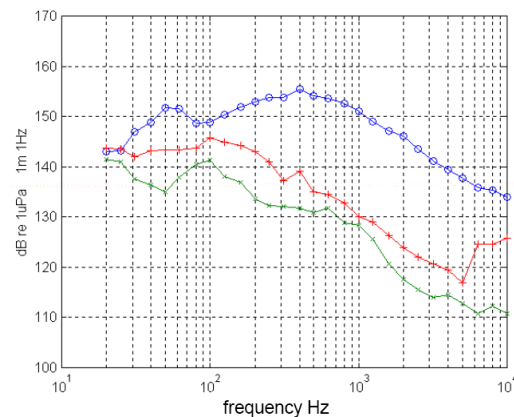


Figure 2-12 Acoustic signatures of the ships Cornide de Saavedra (blue), Vizconde de Eza with keel down (green) and keel retracted (red). Speed 4 knots [30].

Acoustic signature is based on extracting characteristic patterns or features of the signals and using them for recognition. Figure 2-12 presents an example of the feature used by Salvador in [30], which is the Fast Fourier Transform (FFT) from two different ships recordings. Figure 2-13 shows the two steps usually performed in recognition of acoustic signatures. First is the feature extraction block, composed by the front-end and the extraction of the features. At the front-end the signal is pre-processed with digital filters and transforms, such as Discrete Fourier Transform (DFT), wavelet, etc. Some feature extraction examples are envelope detection, pitch, bass, frequency modulation, spectral flatness, etc. Once the features are extracted and organized, a comparison with a features database is performed.

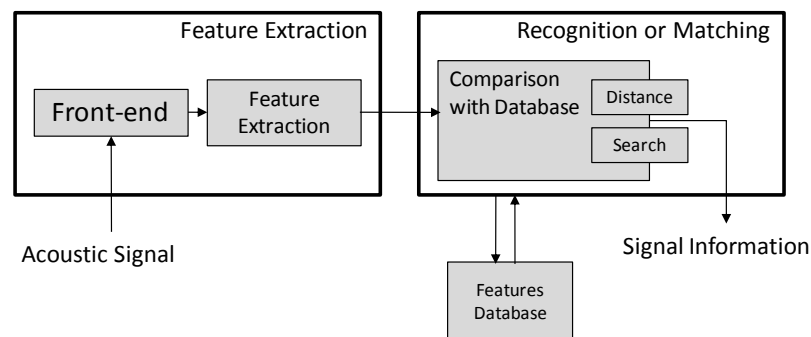


Figure 2-13 Framework used in acoustic signature recognition [29] and audio identification [31].

In [29] three recognition techniques were studied, Gaussian mixture models (GSM), hidden Markov models (HMM) and the proposed method, log-magnitude of the short term Fourier transform of the acoustic signature. Experimental results show that the proposed method outperforms GSM and HMM by 50%. For audio identification the common model for comparing features are distance metrics [31], such as, the Euclidean distance, Nearest Neighbor and Manhattan distance.

The pulse-echo technique used in sonar for underwater object recognition was presented in this chapter, along with the acoustic propagation theory in lossless and lossy tubes. This theoretical background leads to the sounds propagation in waveguides with constant cross sectional area. Combining this with acoustic signal processing, a framework utilized for acoustic signature recognition was presented and employed in the algorithm developed to identify obstructions in the water-filled tubes, as next chapter explains.

CHAPTER 3

MATERIALS AND METHODS

The purpose of this chapter is to describe the experimental setup, signal processing and analysis procedures and experimental design performed in this research. The first section of this chapter shows the components of the experimental pulse-echo setup employed to perform acoustic measurements in water-filled tubes. The second part presents the signal processing framework used in audio recognition and how was utilized to process and analyze acoustic reflections. The last part of this chapter explains the procedure of the experiments performed, such as, wave propagation in copper, PVC and vinyl tubes, obstructions used, recording waveforms, etc.

3.1 Experimental System Setup

In order to measure acoustic reflections in water-filled pipes made of copper, PVC and vinyl, some experimental setups were investigated. Figure 3-1 depicts the experimental setup built in the laboratory, capable of generating acoustic pulses and recording reflections due to obstructions inside the water-filled tube.

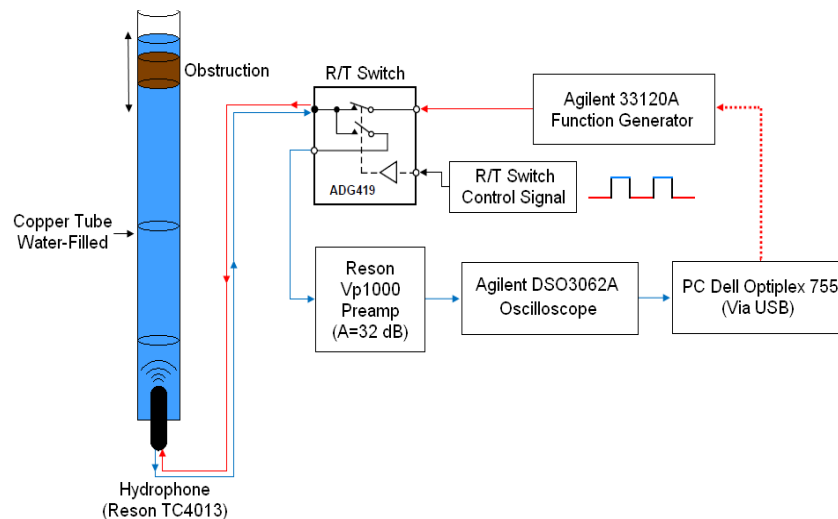


Figure 3-1 Block diagram of experimental device used to measure acoustic reflections in a water-filled tube.

A function generator (Agilent 33120A) was used to generate the excitation signals for the hydrophones. These excitation signals were modulated pulses created in MATLAB. Figure 3-2 shows the process to construct the modulated pulses used for the experiments. To achieve sound propagation in water-filled tubes, different acoustic pulses were tested by varying the pulse frequency and duration.

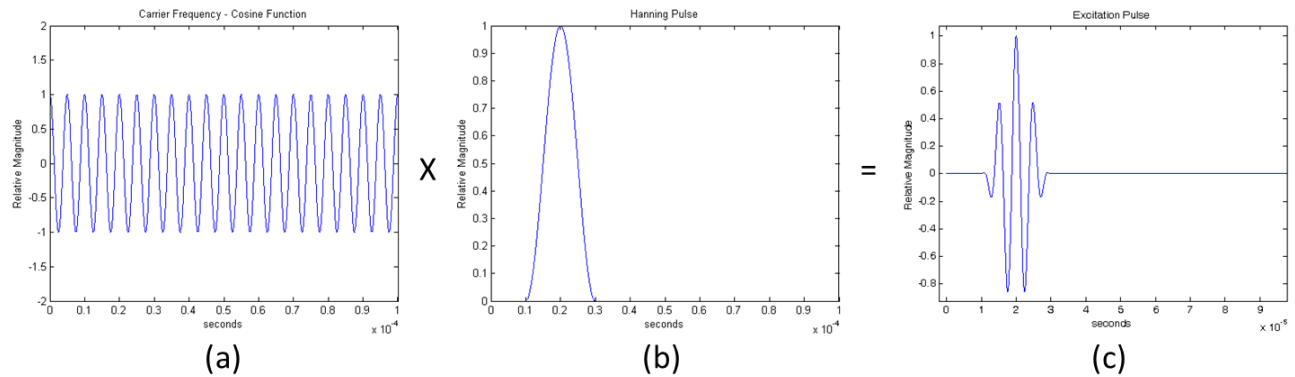


Figure 3-2 Process to create an excitation pulse that will be sent through the hydrophone to the water-filled tube.

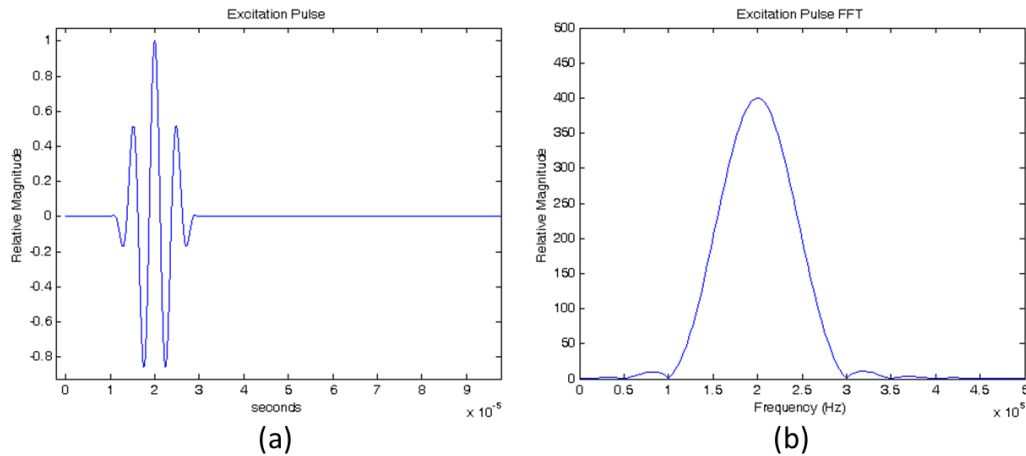


Figure 3-3 Acoustic pulse (a) created in MATLAB with its Fast Fourier Transform (b).

Figure 3-3 shows an incident acoustic pulse (a) with frequency of 200 kHz and 20 μ s of duration, and the pulse FFT (b) calculated with MATLAB, which was expected due to the nature of the Hanning pulse (Figure 3-2b). The equation of a Hanning pulse [32] centered at $t = 0$, is defined by

$$g(t) = \frac{A}{2} [1 + \cos(\pi B_T t)] , \text{ for } -T \leq t \leq T \quad (3.1)$$

where $B_T = \frac{1}{T}$, and its Fourier transform is given by

$$G(f) = \frac{A \sin(2\pi f / B_T)}{2\pi f (1 - 4f^2 / B_T^2)} \quad (3.2)$$

The pulse FFT can be verified by calculating the value of B_T . The duration of the acoustic pulse used in the experiments was 20 μ s, which results in

$$B_T = \frac{1}{T} = \frac{1}{10\mu s} = 100\text{kHz}$$

The cosine has a frequency of 200 kHz, which is the center frequency of the pulse FFT in Figure 3-3b. As indicated in Figure 3-3b the pulse FFT has its first nulls at

$$200\text{ kHz} \pm B_T = 200\text{ kHz} \pm 100\text{ kHz},$$

so the transmission bandwidth of the pulse is essentially from 100 kHz to 300 kHz.



Figure 3-4 Reson TC4013 hydrophone used in the experiments as projector and receiver.

A Reson TC4013 hydrophone was used in the experimental setup to transmit and receive acoustic pulses. This is also known as pulse-echo mode (Figure 1-6), where a single acoustic transducer is used. Pulse-echo methods are used in radar and sonar applications, where a single transducer is used to generate and record sound waves.

In order to transmit and receive acoustic pulses using a single hydrophone, a T/R switch (ADG419) was utilized as Figure 3-1 presents. Figure 3-5 shows the block diagram of the SPDT ADG419 switch employed in the experimental setup. The switch circuit allows the hydrophone (D-pin) to be connected with the signal generator (S2-pin) to transmit the acoustic pulse. After that, the switch changes the hydrophone connection to an Agilent DSO3062A oscilloscope (S1-pin) where the reflection measurements are visualized in a monitor. The switching times and durations were managed by a control

signal connected to the IN-pin input of the switch. When reflections were recorded, signal conditioning techniques were employed to obtain a good quality reflection signal.

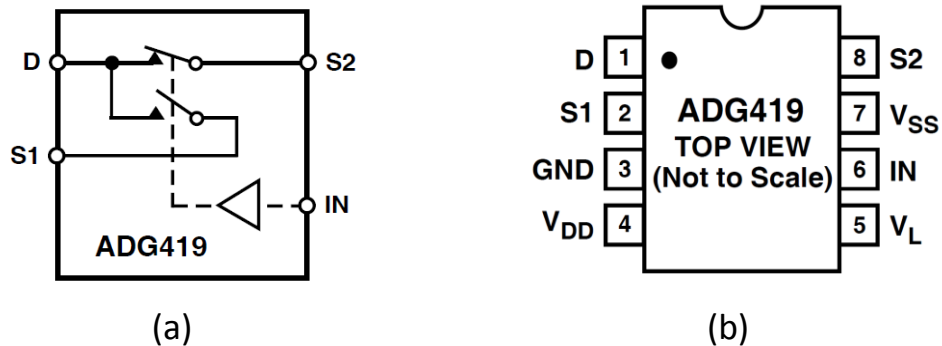


Figure 3-5 Functional block diagram (a) of the SPDT switch ADG419 and a top view of its pin configuration.



Figure 3-6 Reson VP-1000 signal amplifier and analog filter.

As presented in Figure 3-1 a Reson VP-1000, shown in Figure 3-6, pre-amplifier and filter was used to amplify the reflections, and a filter to eliminate low frequency components. Once the reflections were measured and amplified, the oscilloscope was connected to a computer (Dell OptiPlex 775) to transfer the reflection signal. After the data was stored, it was processed and analyzed using MATLAB where signal processing techniques were implemented to determine obstruction type, size and position inside the water-filled tube. Figure 3-7 illustrates the connection diagram of the complete experimental setup previously explained. A resistance (R) was connected to ground in the receiver channel making the T/R switch grounded when switching, thus reducing an electric crosstalk. Finally, Figure 3-8 illustrates the actual experimental setup built for the experiments in the *Biomedical Instrumentation Research Laboratory*.

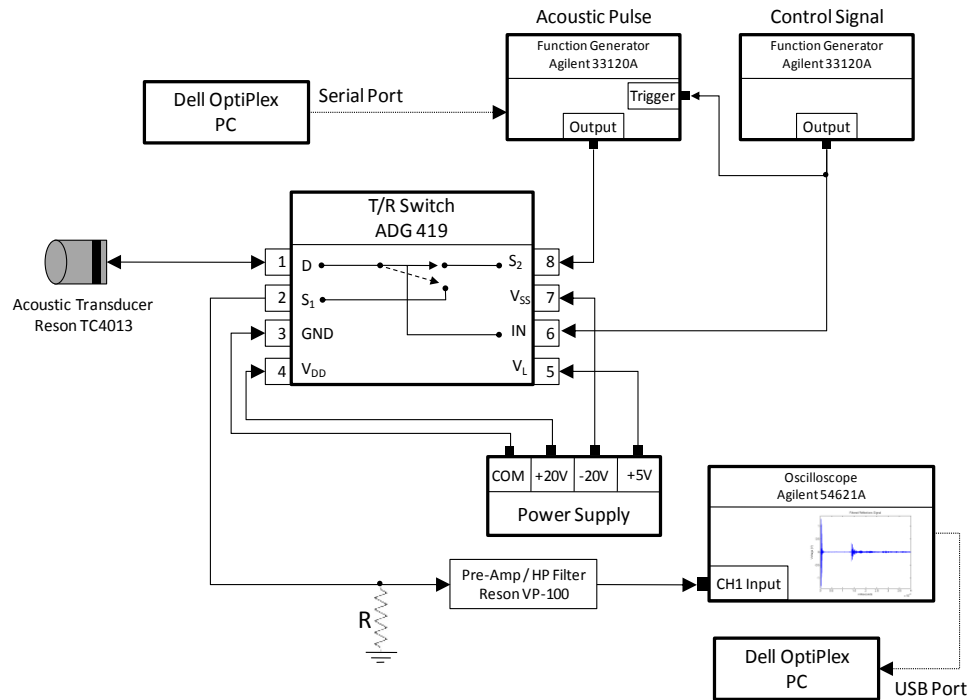


Figure 3-7 Connection diagram of the experimental setup used to record acoustic reflections of water-filled tubes.

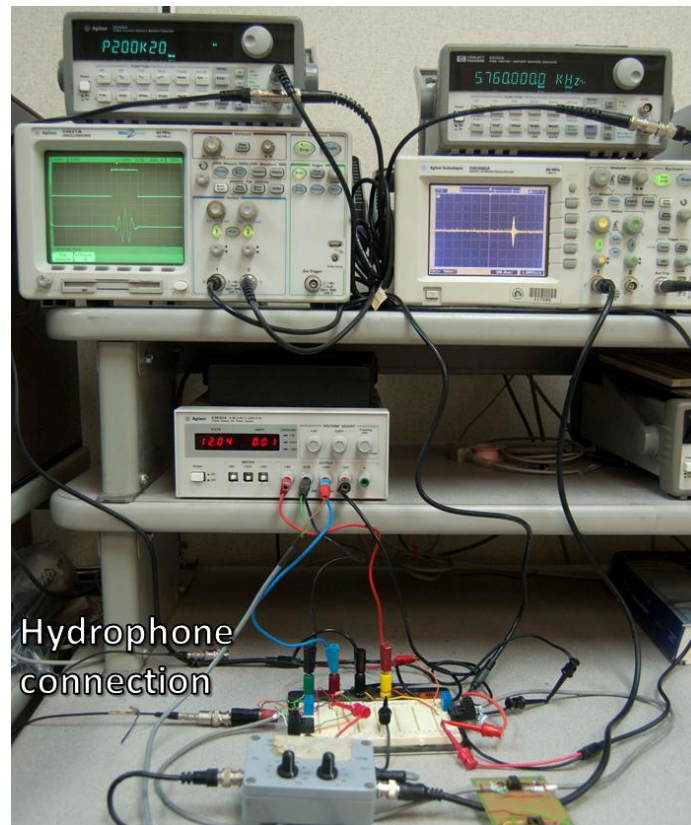


Figure 3-8 Photo of the experimental setup used to create and record acoustic reflections produced by obstructed water-filled tubes made of copper, PVC and vinyl.

3.2 Signal Processing and Analysis

Figure 3-9 presents the general procedure of the algorithm that was developed to process, analyze and classify acoustic reflections in water-filled tubes. This type of framework is used in audio identification [31, 33] and object recognition [26-27], where the fundamental processes are signal feature extraction and signal matching. The signal feature extraction derives a set of acoustic signal characteristics. Given a signal feature derived from an acoustic reflection, the signal matching algorithm searches a database of signal features to find the best match. The steps of the overall procedure are described below in detail.

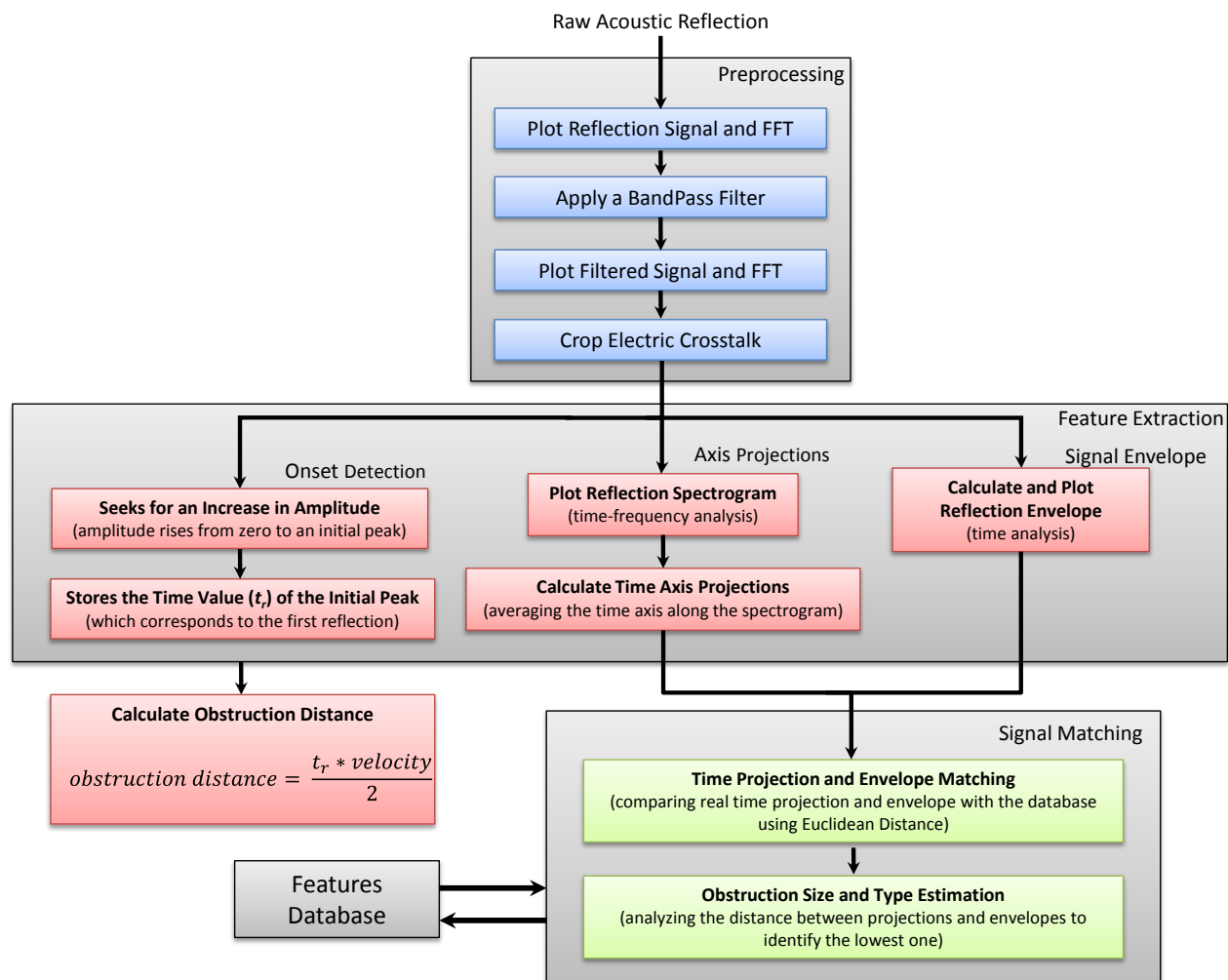


Figure 3-9 Flow chart of the algorithm for acoustic reflections signal preprocessing (blue), feature extraction (red) and signal matching (green).

The first step in the acoustic reflections signal processing was to read the raw reflection data from the oscilloscope and transfer it to the computer via USB connection. This raw data was stored in the PC in a text file, which was opened in MATLAB for analysis.

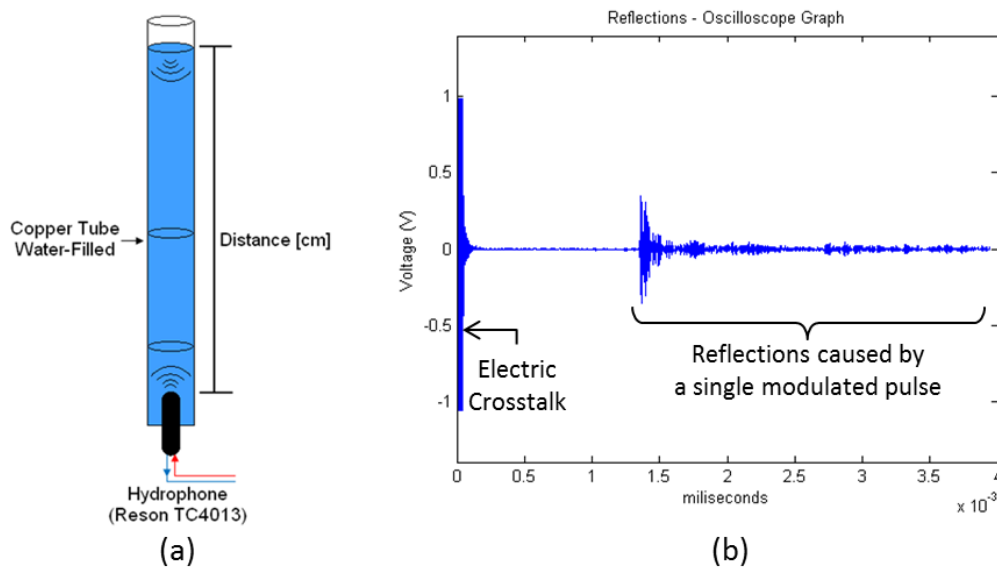


Figure 3-10 Example of a reflection recorded by the pulse-echo measuring system in a water-filled copper tube of 2.54cm (1 inch) diameter and 1.3 meters long (a). The incident acoustic pulse is $20\mu\text{s}$ and 200 kHz of frequency. The reflection belongs to the water/air interface at the top-end of the tube (b).

Figure 3-10 shows an example of the raw reflection data plotted in MATLAB, which belongs to the water/air interface at the top end of the tube. The reflection is produced by the change in acoustic impedance between water and air. It is notable to remark an electric crosstalk created by the T/R switch. When the incident pulse is sent and passes through the switch it interferes with the receiving signal. Since the receiving channel is amplified by the Reson VP-1000 amplifier, the incident pulse is saturated at power supply voltages creating the electric crosstalk. The electric crosstalk is not useful for signal processing thus this part of the signal was cropped for further analysis.

Once the raw data was obtained, a FFT of the reflection wave was performed (Figure 3-11a) to observe if its spectrum was in the same range of the incident signal presented in Figure 3-3b. Next a digital bandpass filter was applied to the reflections signals to reduce noise. The cutoff frequencies of the bandpass filter were 100 kHz and 300 kHz since this was a 200 kHz pulse with ± 100 kHz of bandwidth.

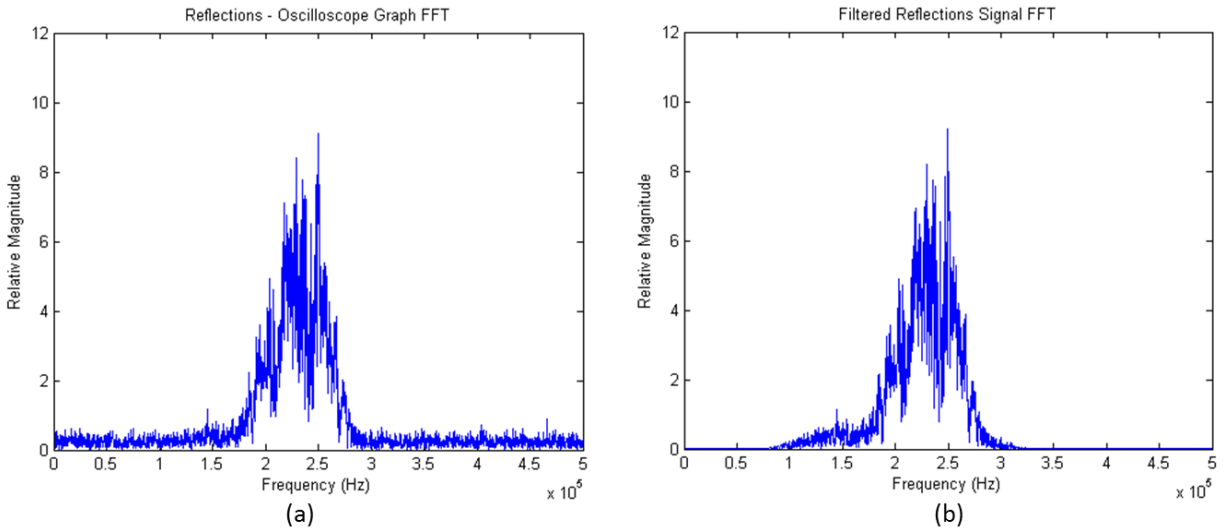


Figure 3-11 FFT of the reflection raw data (a) and after the bandpass filter is applied (b) with cutoff frequencies of 100 kHz and 300 kHz.

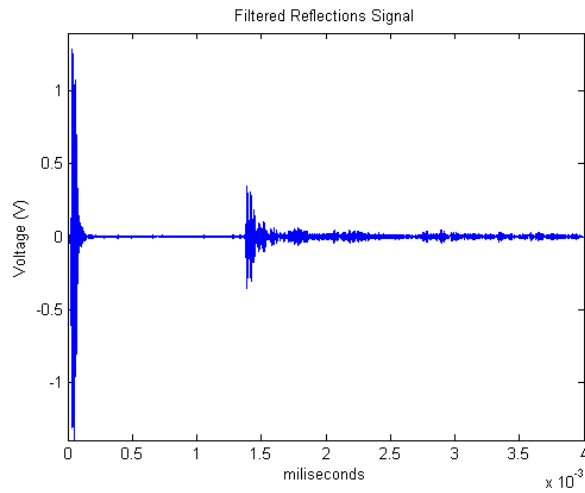


Figure 3-12 Reflection signal of the water/air interface after the bandpass filter is applied.

Figure 3-12 shows the reflection wave after the bandpass filter is applied, where a reduction in the signal noise can be observed when compared to Figure 3-10b. Now with this filtered time signal achieved, the algorithm proceeded to analyze the acoustic reflections signals. The most common transformation used in audio identification is the FFT [31, 33-34]. In [34] Richly et al. revealed that the DFT is generally less sensitive to time-shifting. The main idea of linear transforms is to convert a set of measurements to a new set of features which are stored in a database.

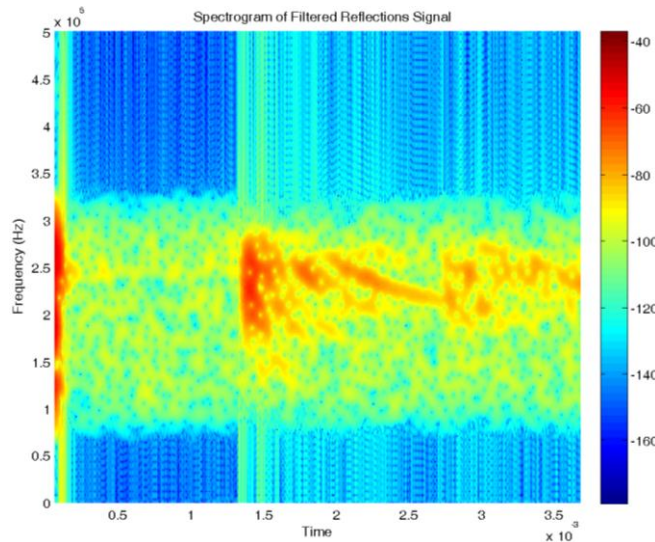


Figure 3-13 Spectrogram of the filtered reflection signal of the water/air interface, where an increased in PSD is observed at 1.5 ms which belongs to the reflection and at 0 ms due to the electric crosstalk.

Spectrograms are images that show how the power spectrum density (PSD) of a signal changes as time elapses. The horizontal axis represents time, while the vertical axis is the frequency. The third axis indicates the PSD amplitude of a particular frequency at a particular time, represented by the color of each point in the image. Figure 3-13 shows the spectrogram from the acoustic reflection signal in Figure 3-12. It is observed an increment in PSD at $t=0$ ms which is the electric crosstalk and approximately at 1.4 ms the first reflection. Since spectrograms are images, these can be represented as a m -by- n matrix A ,

$$A = \begin{bmatrix} a_{1,1} & a_{1,2} & \dots & a_{1,n} \\ a_{2,1} & a_{2,2} & \dots & a_{2,n} \\ \vdots & \vdots & \ddots & \vdots \\ a_{m,1} & a_{m,2} & \dots & a_{m,n} \end{bmatrix}$$

where m (rows) are discrete frequency values, n (columns) are discrete time values and $a_{m,n}$ is the PSD value at $m \times n$. These discrete values are established by the parameters used in the spectrogram. Two reflection signal features were extracted from the spectrogram by projecting the time and frequency axis. The time axis projection was calculated averaging each column, as described by

$$P_{Time}[i] = \frac{1}{m} \sum_{i=1}^m A_{i,n}. \quad (3.3)$$

Therefore the frequency axis projection, averaging each row by

$$P_{Freq}[i] = \frac{1}{n} \sum_{i=1}^n A_{m,i} \quad (3.4)$$

Figure 3-14 illustrates the spectrogram frequency (a) and time (b) axis projections. For these projections the electric crosstalk was cropped in order to just analyze the reflection measured. In the frequency axis projection (Fig. 3-14a) the overall bandwidth of the reflection is observed, where a maximum PSD value occurs approximately at 250 kHz. Meanwhile the time axis projection (Fig. 3-14b) shows the increments of PSD as time elapses, making evident the time when a reflection occurs.

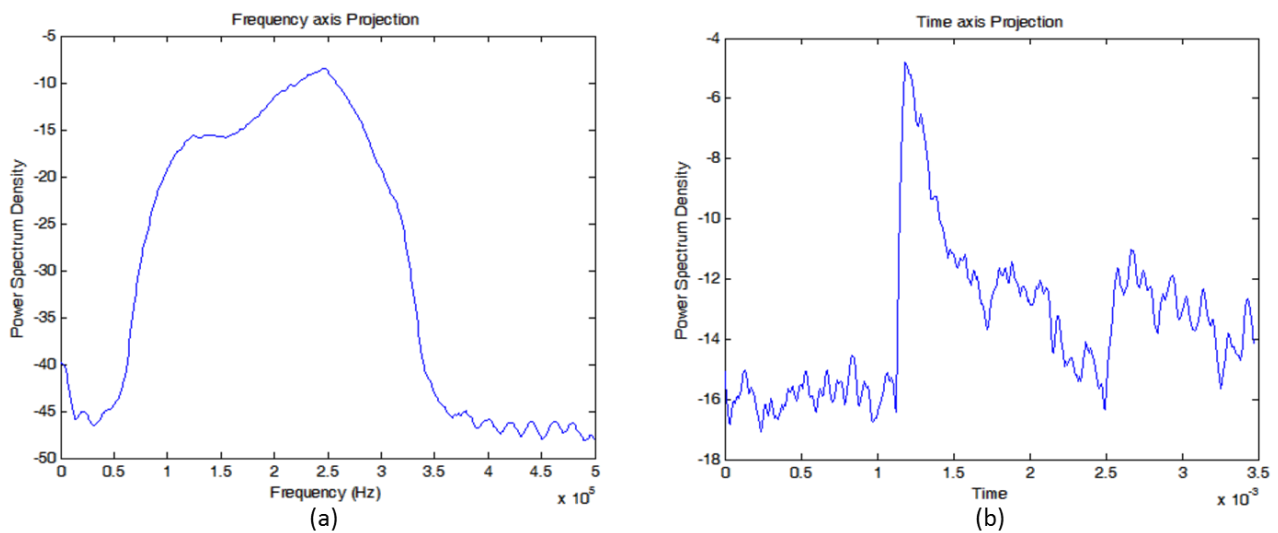


Figure 3-14 Projections of the spectrogram (Figure 3-11) frequency axis (a) and time axis (b) using Equation 3.3 and 3.4.

As mentioned before the reflection from where these plots are taken is from the water/air interface at the top of the tube. When an obstruction is introduced in the tube, the projections vary in intensity and shape, leading to the creation of a projection database. The procedure used to create the projection database was used to process unknown acoustic reflections. Once unknown signals are processed, these were compared with the database using distance metrics. Acoustic signature matching is commonly calculated using a distance measurement between feature vectors rather than a direct binary match. The distance metric that was implemented in the projection matching algorithm was the Euclidean distance,

$$d(P_{database}, Q_{unknown}) = \sqrt{\sum_{i=1}^n (P_i - Q_i)^2} \quad (3.5)$$

used in [35]. Others distance metrics methods used in audio matching presented in [31] are the Nearest Neighbor, Manhattan distance and another error metric called Exponential Pseudo Norm. The Euclidean distance was used among the other distance metrics by its simplicity to be calculated and convention calculating the distance between two points. While distances are calculated, these are accumulated to decide if there is a correct identification, seeking the lowest distance.

Another feature that was extracted from the acoustic signal is the reflection onset. Onset detection is a method used in signal processing to measure increments of amplitudes in time-domain signals or increments of spectral density in the frequency-domain. An onset detection algorithm was developed to measure the time (t_r) when an amplitude increment occurs in the time-domain reflection signals. From Figure 3-12 and 3-14b, the time at which the first reflection occurs is easily observed and by knowing the distance from the hydrophone to the water/air interface, the velocity of the first propagation mode can be estimated by

$$v = \frac{d_{obs}}{t_r/2} \quad (3.6)$$

The term $t_r/2$ is used instead of t because the acoustic wave travels back and forth along the tube and only one way is needed to calculate the velocity. Applying Equation 3.6, the velocity was estimated for different obstruction distances along the tube, varying d_{obs} while the onset detection algorithm finds t_r . Averaging the velocity for different obstructions distances, Equation 3.6 can now be utilized to estimate the distance of an obstruction. The onset detection algorithm estimates when the first reflection occurs (t_r), then using the average velocity and solving Equation 3.3 in terms of d_{obs} ,

$$d_{obs} = \frac{t_r v}{2} \quad (3.7)$$

the obstruction distance was estimated.

In [31] some other features used in audio identification are presented, which are Envelope Detection, Spectral Flatness, Filter bank Energies and Discrete Cosine Transform.

3.3 Experimental Design

The experiments were performed in the setup presented in Figure 3-1. Once the system was connected and properly synchronized, acoustic propagation experiments were performed. First, adequate acoustic propagation in the water-filled tubes is required in order to record a reflection. To achieve propagation, the duration and frequency of the acoustic pulse were varied until a reflection with adequate amplitude was obtained. Figure 3-15 shows the tubes used in the experiments, which were made of copper, PVC and vinyl, with a diameter of 2.54 cm for copper and PVC tubes, and 1cm for the vinyl tube. Since the propagation in tubes depends on its radius, different incident pulses were tested for propagation along the tubes. The carrier frequency of the acoustic pulses was varied from 50 kHz to 300 kHz in increments of 50 kHz, with pulse duration of 10, 20 and 30 μ s for each frequency value.

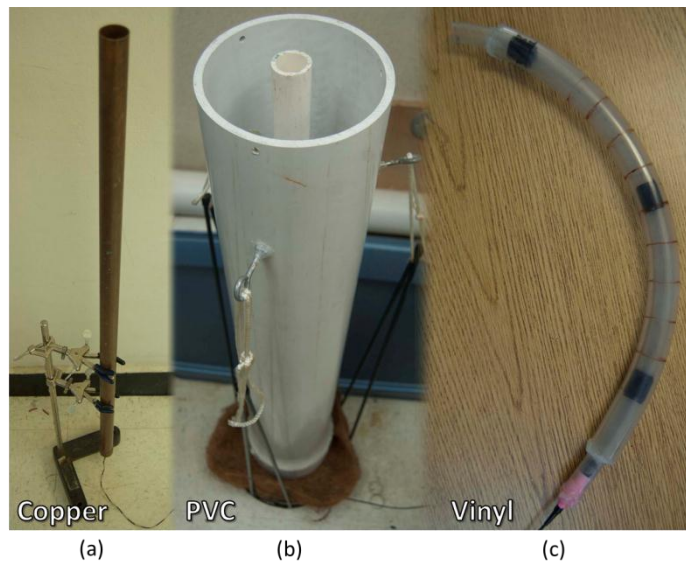


Figure 3-15 Three different tubes used for the experiments, (a) copper, (b) PVC and (c) vinyl.

When acoustic propagation was achieved, reflection measurements were recorded first by varying the obstruction location in the water-filled tubes as shown in Figure 3-16. A stainless steel (S.S.) obstruction of the size of the inner diameter of the tube was located at 5 cm from the hydrophone, and moved with an increment of 5 cm until the water/air interface (at 1 meter from the hydrophone) was reached. The distance measurements were used to calculate the average velocity of the fastest propagation

mode. Then the obstruction location was estimated using Equation 3.7 and the onset detection algorithm. The obstruction position measurements were performed first in the PVC and copper tubes, to test the resolution of this method which estimates the obstruction location.

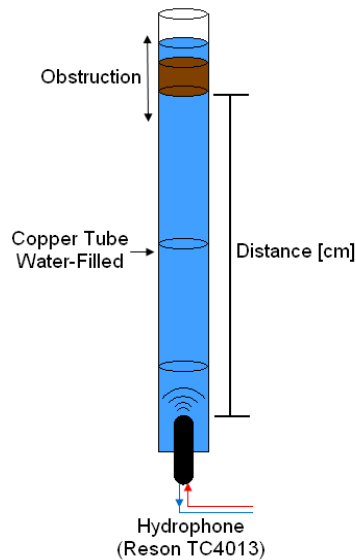


Figure 3-16 Varying obstruction position along the water-filled copper tube.

Next, the S.S. obstructions size was varied as presented in Figure 3-17 and the reflections produced by these obstructions were recorded. Each obstruction was located as mentioned before, starting at 5 cm from the hydrophone and moved along the tube. This measuring procedure was repeated 5 times to have different signals of the same situation (obstruction position and size). Using the 5 measurements for each obstruction position and size, an average signal envelope and spectrogram time-axis projections was calculated using the algorithm presented in Figure 3-9. The average time-axis projections and signal envelopes were used to create the database for S.S. obstructions location and size. The signal matching algorithm compared an unknown reflection projection and envelope with the projection and envelope database to find the best matching signal. Finally, the algorithm displayed the name of the matching signal indicating the obstruction position and size.

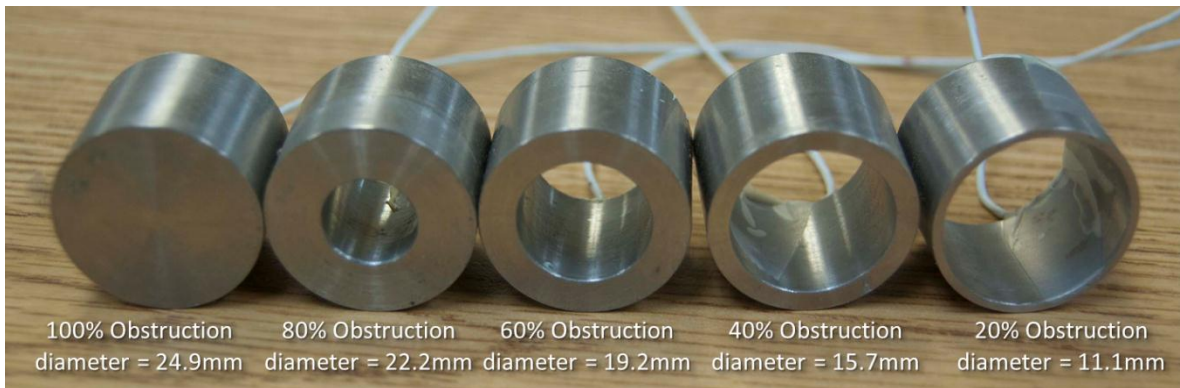


Figure 3-17 Stainless Steel obstructions used with different diameters.

The matching and onset algorithm was first used in the PVC and copper tubes to verify its precision estimating the obstruction position and size. Once achieving this, a third obstructions parameter which is the density (ρ) or type was varied. The type of the obstruction was varied by changing its material (density), starting with stainless steel obstructions (8.03 g/cm^3) as already mentioned. The other obstruction type used was Delrin (Polyoxymethylene), presented in Figure 3-18, with a density of 1420 kg/m^3 . As measured with S.S. obstructions, the Delrin obstructions positions and size were varied along the PVC and copper tube, recording 5 measurements for each case. Then using the feature extraction algorithm, a features database was created for Delrin obstructions. Lastly, the signal matching algorithm was used to estimate the obstruction position, size and type in the water-filled PVC and copper tubes.

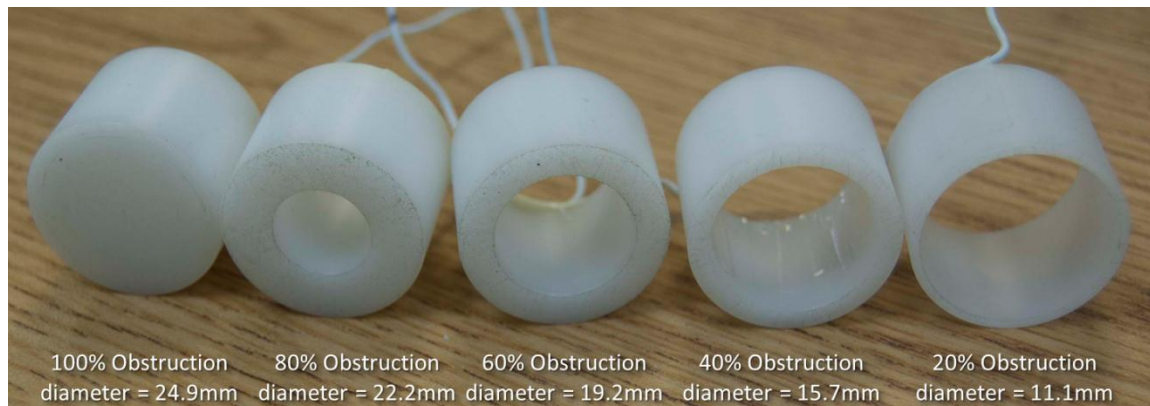


Figure 3-18 Delrin obstructions used with different diameters

Once the feature extraction and signal matching algorithms have been tested to estimate obstructions position, size and type in the PVC and copper tubes, these were tested in a special configuration of water-filled vinyl tube to estimate obstructions. Figure 3-19 shows the special vinyl tubes configuration used, which consist of a water-filled vinyl tube with a diameter of 5/8 inch inside a 1 inch vinyl tube. This creates a layer of air between the tubes, which kept the acoustic wave traveling inside the inner vinyl tube. The vinyl tubes configuration was surrounded by water, as Figure 3-19 presents, which resembles a catheter being used on a patient.

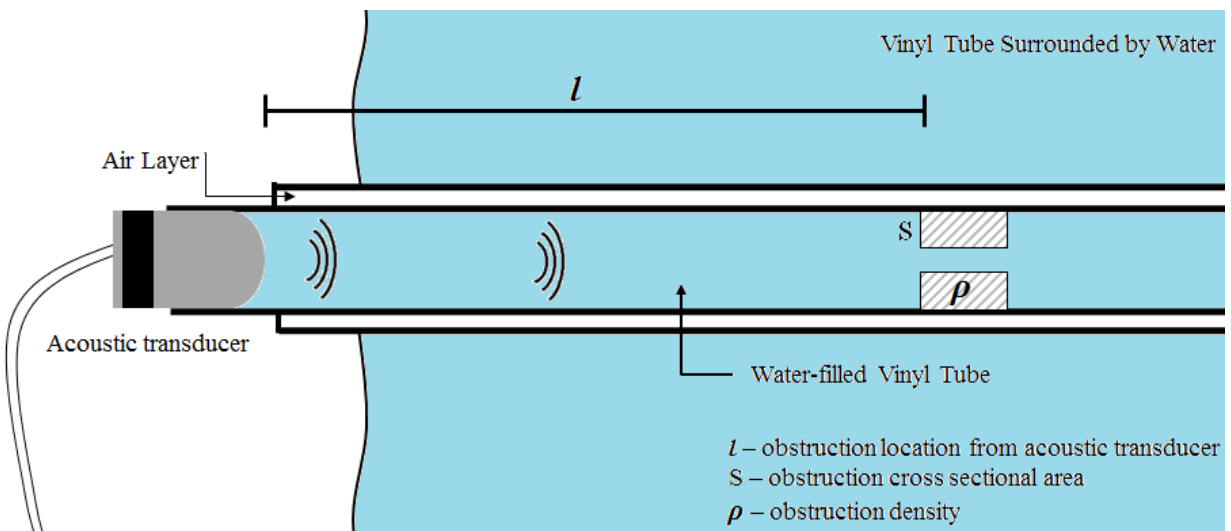


Figure 3-19 Experimental setup for the measurements in water-filled vinyl tube varying obstruction location, size and density.

Since the inner diameter of the vinyl tube is 1.5 cm of diameter, the obstructions shown in Figure 3-17 cannot be used. Figure 3-20 shows the obstruction used for the vinyl tube experiments made of S.S. and Delrin. The same procedures were implemented for this tube, which consists of, five measurements for each obstruction type, size and position along the vinyl tube. The reflection waves recorded were analyzed using the signal matching algorithm to estimate the obstruction position, size and type.



Figure 3-20 Stainless Steel and Delrin obstructions used for the 1.5 diameter vinyl tube.

Table 3-1 shows the characteristic acoustic impedance (Z_0) of the S.S. and Delrin obstructions, the PVC, copper and vinyl tubes used in the experiments. It is important to point out that the acoustic impedance of water and silicone rubber, the material used for catheters construction, are very similar. This similarity makes the catheter wall acoustically transparent, causing an acoustic wave traveling inside the catheter to disperse to all directions outside the catheter if it is inside a patient. Consequently, no acoustic wave reaches an obstruction in order to be detected by the system. For this reason the configuration used for the vinyl tubes was implemented. The large change of acoustic impedance from the water-filled vinyl tube to the air layer makes the acoustic waves to be retained in the water-filled vinyl tube. As a result, reflections produced by obstructions can be analyzed to estimate obstruction position, size and type.

Table 3-1 Characteristic acoustic impedance of the water-filled tubes and obstructions used in the experiments. Taken from [36-39].

	Wave propagation speed (m/s)	Density (ρ) (kg/m³)	Characteristic Acoustic Impedance (Z_0) (MRayl)
Air	343.2	1.145	0.000392
Water	1480	~1000 at 20°C	1.48
Delrin Obstructions	2430	1420	3.45
Stainless Steel Obstructions	4515	8030	36.23
PVC Tube	2380	1380	3.27
Copper Tube	3810	8940	34.06
Vinyl Tube	2230	1100-1300 flexible tubes	2.96
Silicone Rubber (material used for catheters)	0.974	1380	1.34

CHAPTER 4

EXPERIMENTAL RESULTS

The purpose of this chapter is to present and discuss the results obtained by analyzing the reflections produced by stainless steel and Delrin obstruction located in water-filled PVC, copper and vinyl tubes, in order to identify the obstruction type, size and location extracting the reflection signal envelope and time-axis projection. The first part of the chapter presents step by step how the acoustic propagation, propagation velocity estimation, feature extraction and database creation, and finally the signal matching results for obstructions located in water-filled PVC tube were achieved. The second part shows the signal matching algorithm results when estimating obstruction position, size and type in the water-filled copper tube. The third part presents the signal matching results for obstructions characterization in water-filled vinyl tube. The last section of the chapter shows a comparison between the accuracy and error estimating obstruction position, size and type using the signal envelope and time-axis projection for each water-filled tube.

4.1 PVC Tube Measurements

A PVC tube of 1 meter long, with a diameter of 2.54 cm (1 inch), was used for the experiments. Figure 4-1 shows the water-filled PVC tube with an 80% stainless steel obstruction, located 75cm away from the bottom part of the tube where the hydrophone is placed. The next section describes how acoustic propagation was achieved, in the water-filled tube.

4.1.1 Wave Propagation in PVC Tube

To achieve wave propagation in the water-filled PVC tube, of 1 inch diameter, different acoustic pulses were tested with variations in duration and modulated carrier frequency. From Equation 2.33, the

first propagation mode for the PVC tube will be approximately at 36 kHz, being the starting point to test different pulses in the experimental setup. The carrier frequencies of the pulses were varied from 50 kHz to 300 kHz in 50 kHz steps. The pulse duration was also varied between 10 μ s, 20 μ s and 30 μ s. For lower frequency values the duration should be longer, in order to allow sufficient cycles of the modulated pulse to be transmitted. In the other hand, short pulses have a wider bandwidth than longer pulses, and as the pulse duration increases the spatial size of the pulse similarly increase. This leads to the use of durations between 10 and 30 μ s, which results in pulses with sizes from 1.5cm to 4.5cm.



Figure 4-1 Water-filled PVC tube used for the experiment and measurements. An 80% stainless steel obstruction is located at 75cm from the bottom part of the PVC tube where the hydrophone is located.

Figure 4-2 shows the reflections recorded using different modulated pulses in the water-filled PVC tube with a 100% stainless steel (S.S.) obstruction at 60cm from the hydrophone. For frequencies below 100 kHz no propagation was achieved using the pulse-echo system. The pulse duration of the 50 kHz and 100 kHz pulses was set to 20 μ s, but for these frequencies the acoustic pulses did not propagate along the tube and consequently no reflections were produced inside the tube. For incident pulses of 150 kHz and over, the wave propagation in the water-filled PVC tube was achieved. Figure 4-2d presents the reflection recorded using a 200 kHz pulse with duration of 20 μ s, where it is observed that this reflection has greater amplitude than reflections using 250 kHz - 10 μ s and 300 kHz - 20 μ s pulses. Figure 4-2g shows the greatest reflection amplitude, but the incident pulse is 300 kHz and 30 μ s resulting in more propagation modes transmitted due to the greater value of frequency components. For this reason the incident pulse chosen for the experiments was the 200 kHz pulse with duration of 20 μ s.

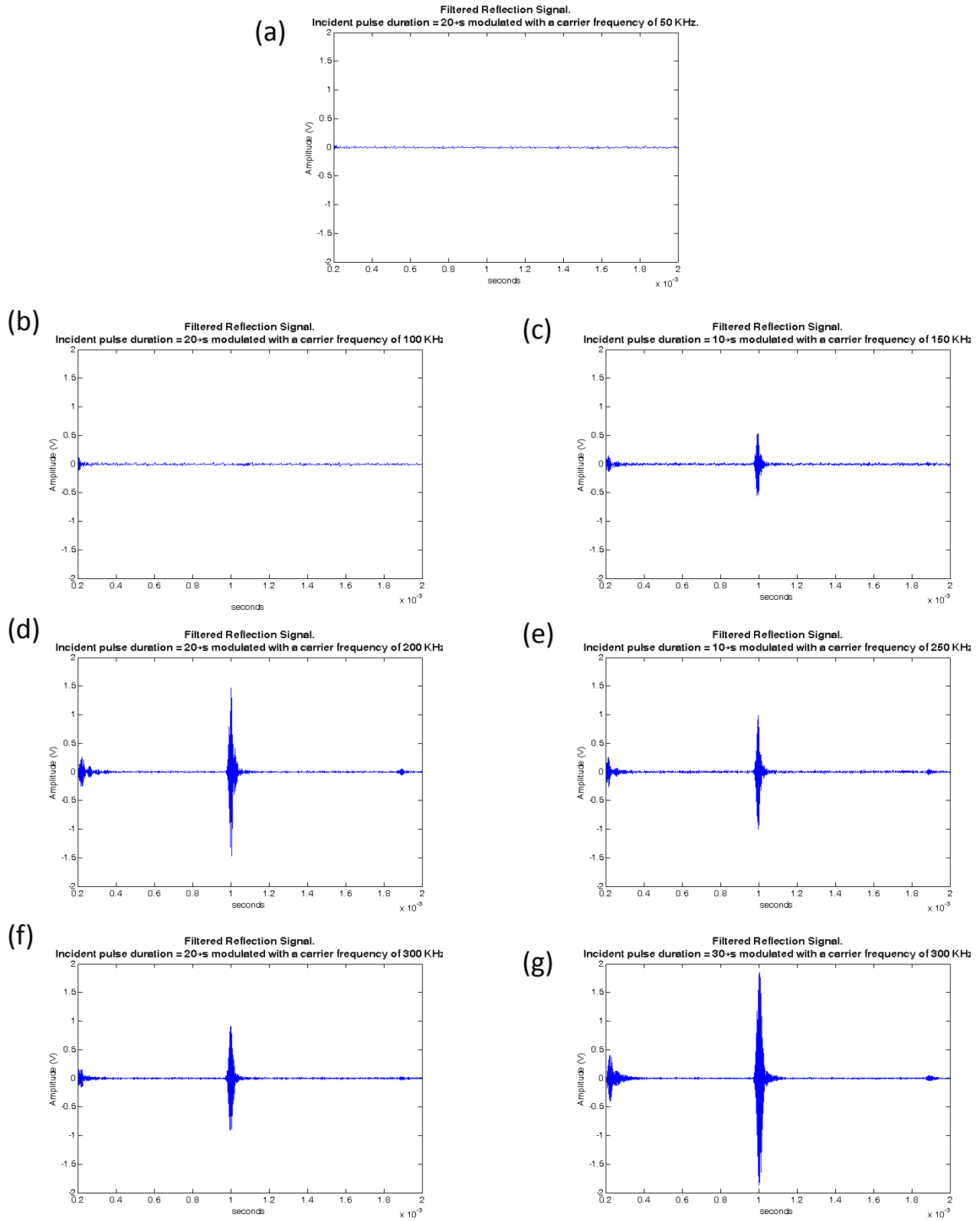


Figure 4-2 Acoustic reflections due to a 100% S.S. obstruction located at 60cm from the hydrophone. The incident pulse carrier frequency and duration was varied from (a) 20 μ s and 50 kHz, (b) 20 μ s and 100 kHz, (c) 10 μ s and 150 kHz, (d) 20 μ s and 200 kHz, (e) 10 μ s and 250 kHz, (f) 20 μ s and 300 kHz and (g) 30 μ s and 300 kHz.

4.1.2 PVC Reflection Analysis

A modulated acoustic pulse of 20 μ s of duration and frequency of 200 kHz was used as the probing signal. A stainless steel obstruction was placed in the tube lumen and its position varied along the tube with 5 cm increments. The obstruction was initially placed at a distance of 5 centimeters from the hydrophone. Figure 4-3 presents the acoustic reflections recorded when a 100% S.S. obstruction was located at 15cm, 55cm and 95cm respectively. As seen from Figure 4-3, the time at which reflections initially occur increases with increasing separation distance, as expected. The reflection signals of obstructions located from 5cm to 95cm were processed in MATLAB using the framework presented in Figure 3-9.

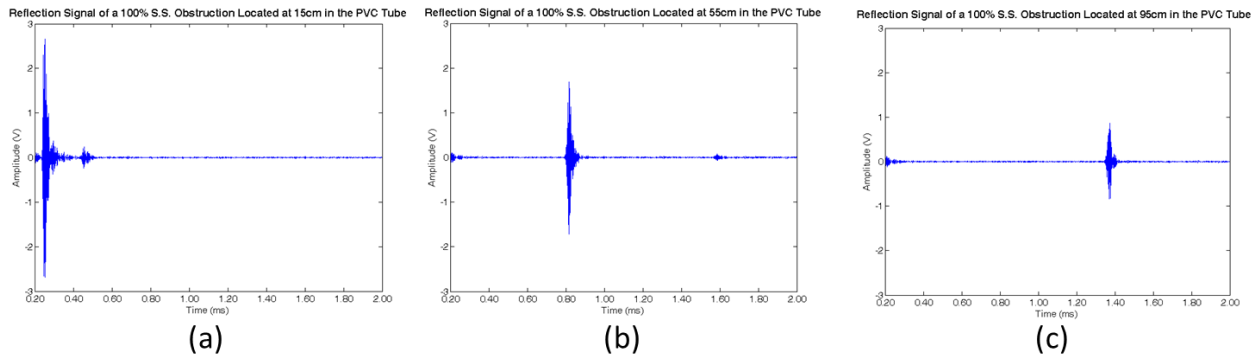


Figure 4-3 Reflection produced by a 100% S.S. obstruction in a water-filled PVC tube, located at 15cm (a), 55cm (b) and 95cm (c) from the hydrophone, using an acoustic pulse of 200 kHz with 20 μ s of duration.

4.1.2.1 Onset Detection in PVC Tubes

The onset detection algorithm was used to find the propagation velocity of the acoustic pulse in the water-filled tube. The propagation velocity is calculated by modifying Equation 3.6, given that waveforms are in samples, results in

$$v = \frac{2d_{obsfs}}{n} \quad (4.1)$$

where f_s is the sampling frequency, d_{obs} the distance of the obstruction and n the sample number when the first echo is produced. The onset detection algorithm estimated the value of n for each reflection waveform. This estimation was performed by establishing an onset threshold of ± 0.06 V, sufficiently small that the system floor noise amplitude cannot reach it. Thus the algorithm only measured the time when the reflection's amplitude overpasses the ± 0.06 V thresholds. Figure 4-4 shows the reflection produced by a 100% S.S. size obstruction located at 75cm from the hydrophone in the PVC tube, where at 1.13 ms the reflection crosses the onset thresholds. This time is then used in Equation 4.1 to calculate the velocities at different obstruction positions along the tube.

Onset Detection of a Reflection produced by an Obstruction of 100% size located at 75cm from the Hyd. in a PVC Tube

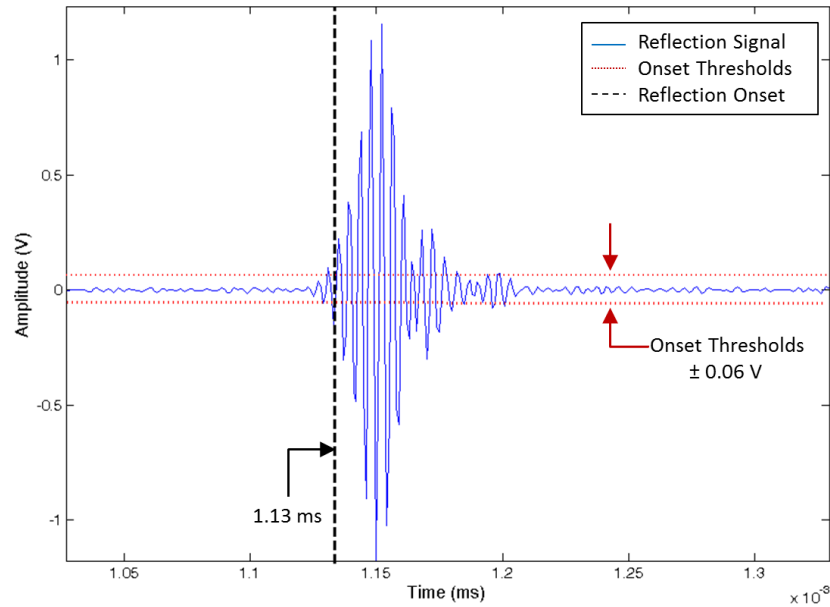


Figure 4-4 Reflection Onset Detection example of a 100% S.S. obstruction located at 75cm from the hydrophone in the PVC tube. The onset detection measures the time when reflections overpasses the threshold limits, in this case results in 1.3ms

Figure 4-5 shows the velocities calculated using Equation 4.1 and n , estimated with the onset algorithm. From this figure it can be state that the velocities are close from each other and in the vicinity of 1497 m/s which is the velocity of sound in fresh water.

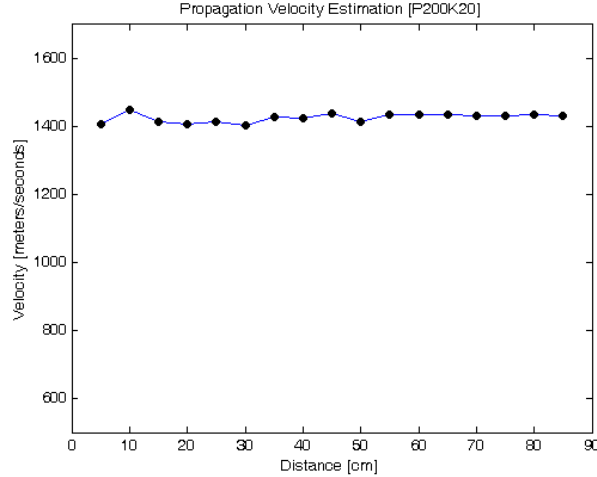


Figure 4-5 Calculated velocities using the onset detection algorithm and Equation 4.1. Each velocity belongs to a reflection produced by an obstruction located in the water-filled PVC tube.

The average velocity (v_{ave}) of Figure 4-5 is 1428 m/s, similar to the sound velocity in water. This v_{ave} is used in the Equation 4.1, and solving for the obstruction distance results in

$$d_{obs} = \frac{v_{ave} n}{2f_s} \quad (4.2)$$

Using Equation 4-2 and the onset algorithm to measure n , the obstruction distance was calculated and then compared with the obstructions real distance. For each obstruction size and location, 10 measurements were recorded to prove the reliability of the algorithm calculating the obstruction position. Table 4-1 presents the average calculated distance and error percentage of a 100% S.S. obstruction in the water-filled PVC tube, using the onset detection algorithm and Equation 4.2. It is important to point out that distance calculated is fairly close to real distance with error percentage below 2%. Figure 4-6 shows the error percentages of the five different stainless steel obstructions located along the tube. For the obstructions of 100% to 60% the error is below 5%, in the other hand for 40% and 20% obstructions the error increases as the distances increases.

Table 4-1 Distance estimation using the v_{ave} calculated, the onset detection algorithm and Equation 4.2. The real and estimated distances were compared resulting in an error percentage of 2% or less and a difference of 1.2cm at most.

Average Obstruction Distance Calculations			
Calculated Distance [cm]	Real Distance [cm]	Difference [cm]	Error Percentage [%]
20.21	20	0.21	1.10
24.96	25	0.04	0.26
29.96	30	0.04	0.27
35.05	35	0.05	0.19
40.27	40	0.27	0.70
45.24	45	0.24	0.53
50.41	50	0.41	0.81
55.43	55	0.43	0.78
60.48	60	0.48	0.80
65.63	65	0.63	0.97
70.79	70	0.79	1.13
75.46	75	0.46	0.61
80.65	80	0.65	0.82
85.99	85	0.99	1.17
91.2	90	1.20	1.33

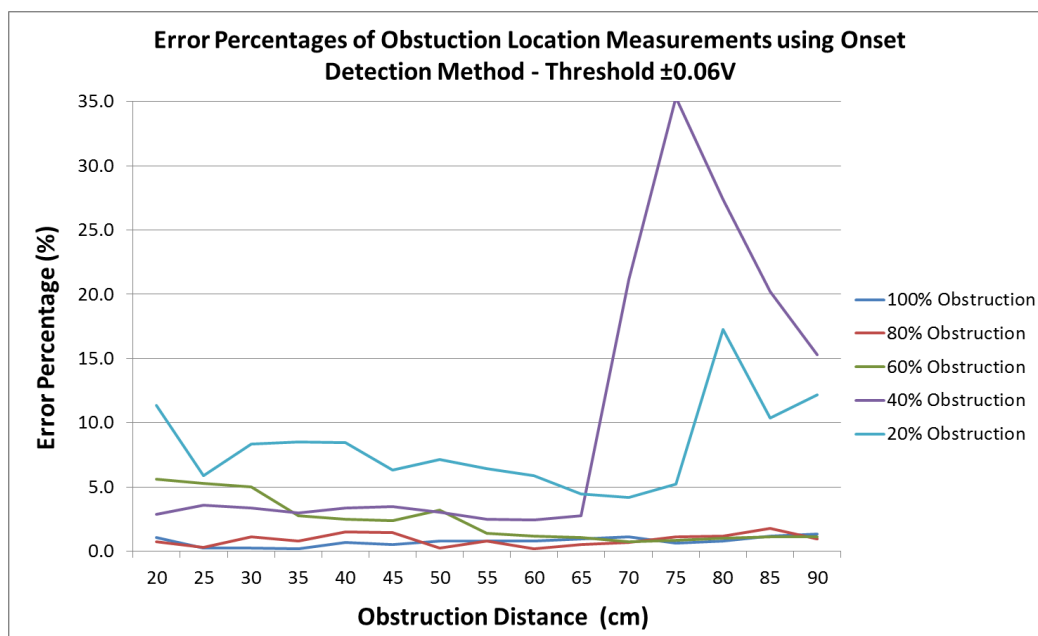


Figure 4-6 Error percentages of obstruction location measurements for 5 different obstruction sizes, using Onset Detection method with $\pm 0.06 V$ thresholds. The obstructions used were made of stainless steel and the sizes were 100% (blue line), 80% (red line), 60% (green line), 40% (purple line) and 20% (light blue line) from the 2.54cm diameter PVC tube.

As already known, small obstructions will produce small reflections, thus small reflections do not overpass the threshold limits of $\pm 0.06\text{V}$. Consequently the algorithm was not able to make an accurate measure of the obstruction distance as Figure 4-6 shows for 40% and 20% size obstructions. To overcome this problem the onset threshold was reduced to $\pm 0.04\text{ V}$. Reflections from 20% and 40% size are presented in Figure 4-7 and 4-8, respectively. The first reflection in both figures is produced by the obstruction located in the PVC tube, while the second reflection is due to the water/air interface at the distal end of the PVC tube. In these figures both thresholds, $\pm 0.06\text{V}$ and $\pm 0.04\text{V}$ are presented, showing that the first reflection does not reach the $\pm 0.06\text{V}$ threshold limits and therefore the reflection onset is not measured correctly. With the threshold set to $\pm 0.04\text{V}$, the 20% and 40% onset reflections were measured correctly and hence a reduction in the obstruction location error percentage, showed in Figure 4-9. For the 40% obstruction the error percentage was reduced from 35% to 10% error for locations greater than 65cm. For the 20% obstruction the error percentage reduction was from 15% for $\pm 0.06\text{V}$ threshold to below 6% using $\pm 0.04\text{V}$ threshold in locations greater than 75cm.

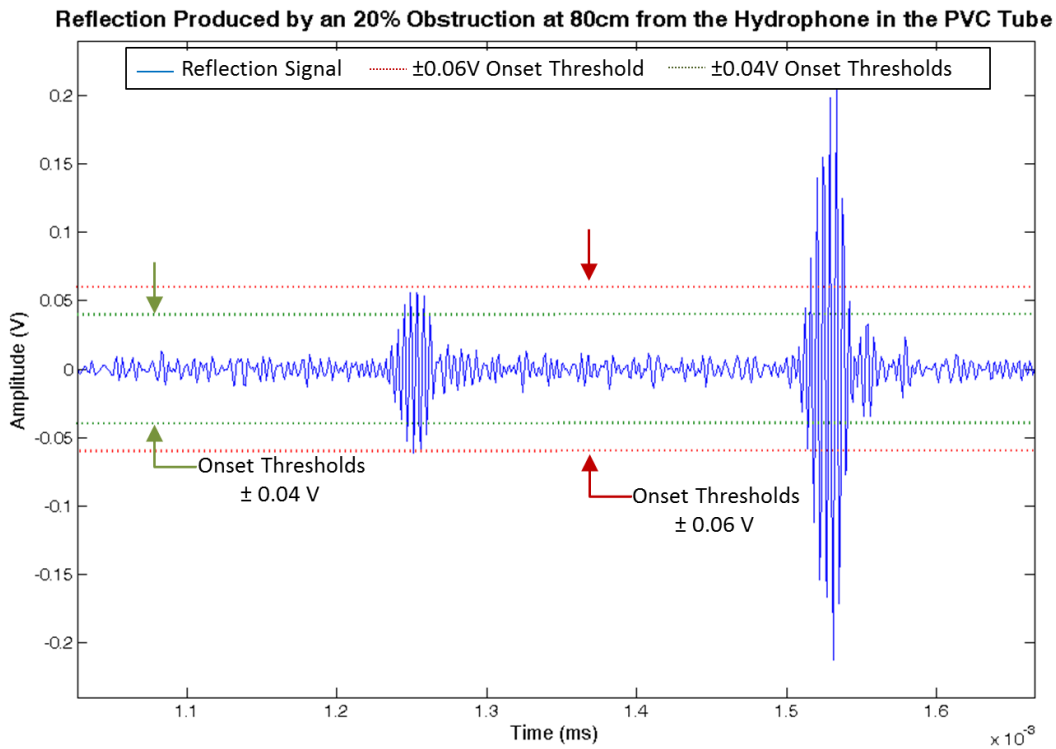


Figure 4-7 Reflection of the 20% obstruction located at 80cm from the hydrophone in the PVC tube. The reflection at 1.25ms is produced by the obstruction, and the 1.5ms reflection is from the water/air interface at the distal end of the PVC tube. The thresholds are $\pm 0.06\text{V}$ (red line) and $\pm 0.04\text{V}$ (green line).

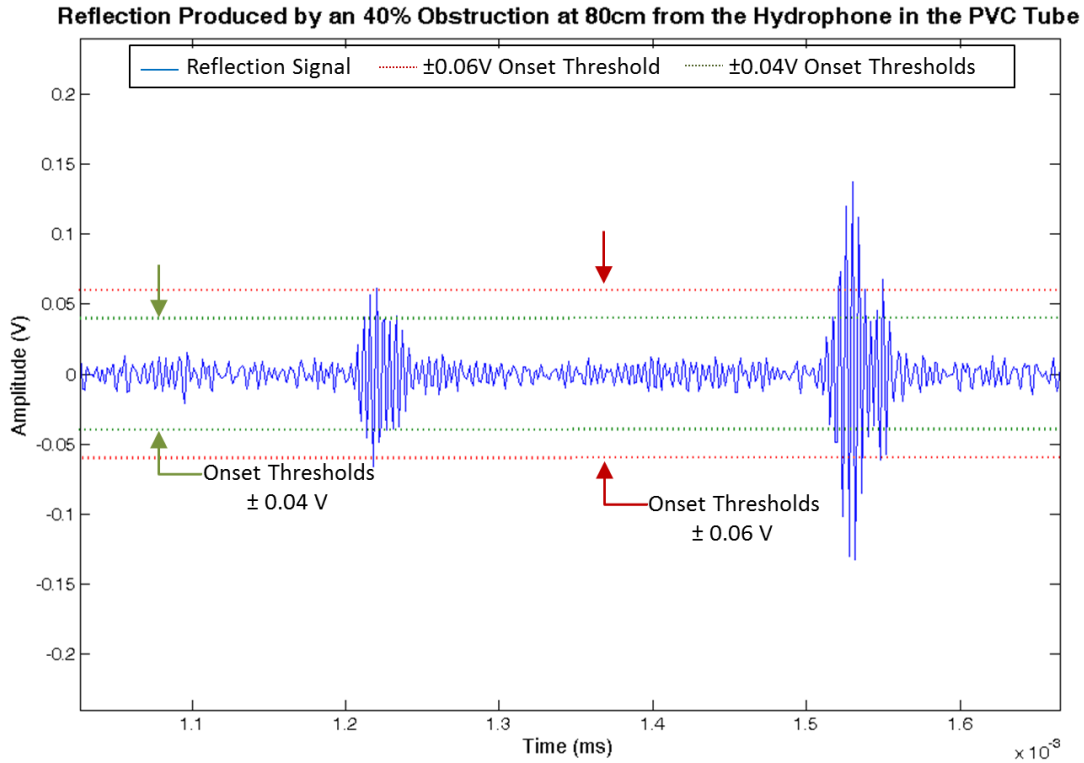


Figure 4-8 Reflection of the 20% obstruction located at 80cm from the hydrophone in the PVC tube. The reflection at 1.25ms is produced by the obstruction, and the 1.5ms reflection is from the water/air interface at the distal end of the PVC tube. The thresholds are $\pm 0.06\text{V}$ (red line) and $\pm 0.04\text{V}$ (green line).

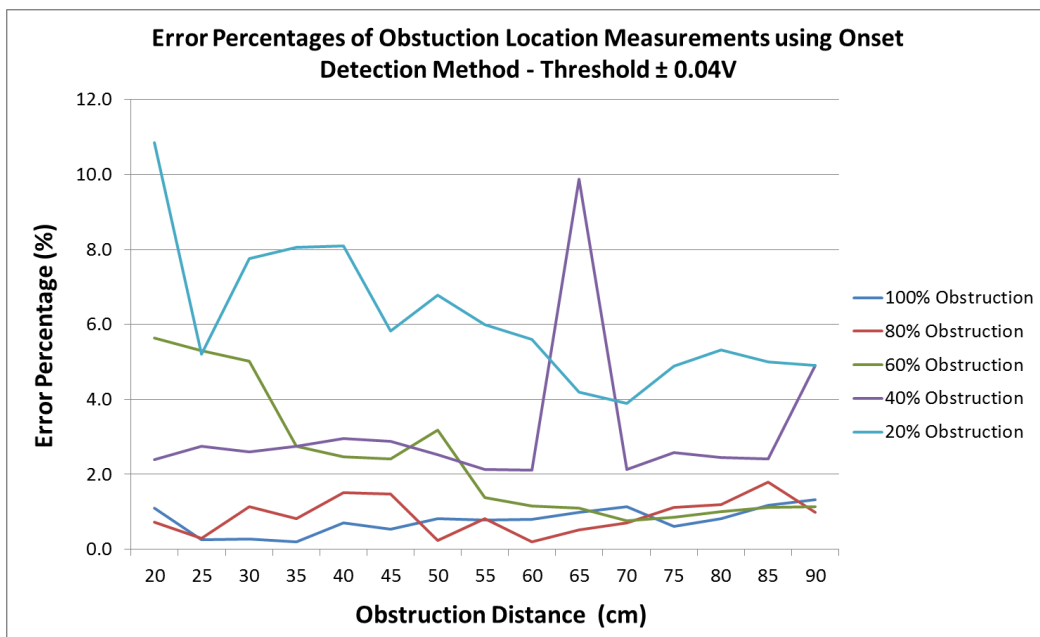


Figure 4-9 Error percentages of obstruction location measurements for 5 different obstruction sizes, using Onset Detection method with $\pm 0.04\text{V}$ threshold. The obstructions used were made of stainless steel and the sizes were 100% (blue line), 80% (red line), 60% (green line), 40% (purple line) and 20% (light blue line) from the 2.54cm diameter PVC tube.

4.1.2.2 Feature Extraction of PVC Tube Reflections

As stated in Section 3.2, feature extraction is a fundamental process in audio identification and object recognition. The extracted features from the reflection waves were the spectrogram time axis projection and envelope of the time signal. The next sections describe how these features are extracted and how are used to determine which type, size and obstruction locations are in the tube lumen.

4.1.2.2.1 Spectrogram Time-Axis Projection

In order to estimate obstruction type, size and location, time-frequency analysis was implemented using spectrograms. Spectrograms are images that show how the power spectral (PSD) energy changes as time elapsed. Figure 4-10 shows the reflection spectrograms produced by a 20% S.S. obstruction located at 40cm and 70cm from the hydrophone. As mentioned before, as the obstruction distances increase, an increment in the PSD of the spectrograms is observed later. Figure 4.10a shows an increment of PSD in 0.5 ms approximately, while Figure 4.10b shows the increment at 0.9 ms, both corresponding to the 20% obstruction at 50cm and 70cm respectively. Since the obstruction size is 20 % (the smallest), a considerable part of the acoustic pulse passes through it. The second PSD increment corresponds to the water level reflection at top of the tube (approximately at 1.35 ms). Figure 4-11 presents how PSD varies as the obstruction size increases, leading to a characterization of obstruction sizes. As expected, Figure 4-11 shows that by increasing the obstruction size a greater reflection is produced, due to the higher reflection coefficient (Equation 2-6) for larger changes in cross sectional area.

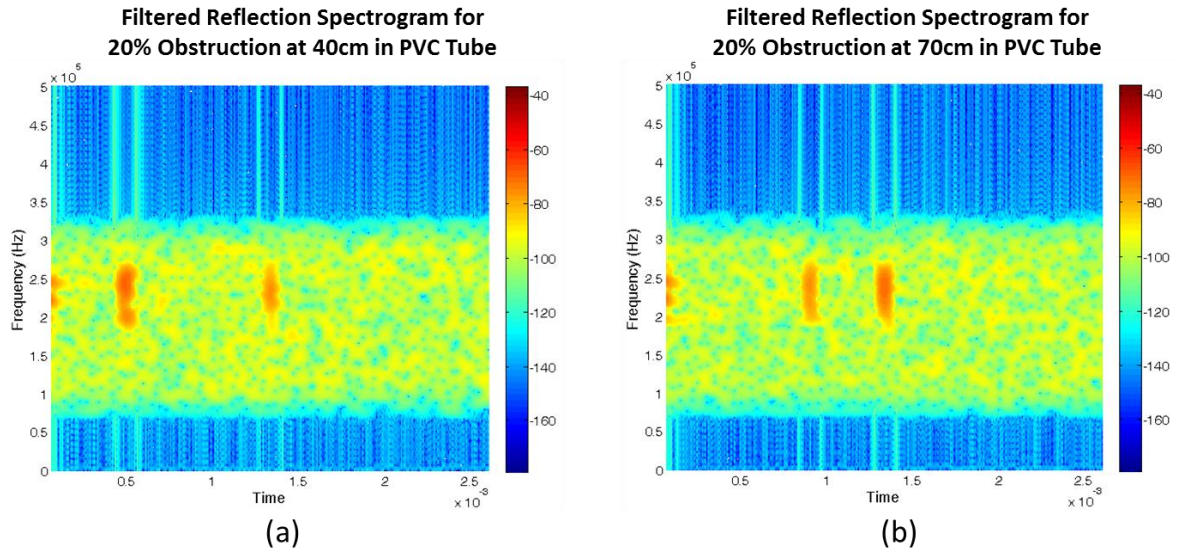


Figure 4-10 Spectrograms of an obstruction reflection of 20% size at 40cm (a) and 70cm (b) in a water-filled PVC tube using a 200 kHz and 20 μ s acoustic pulse.

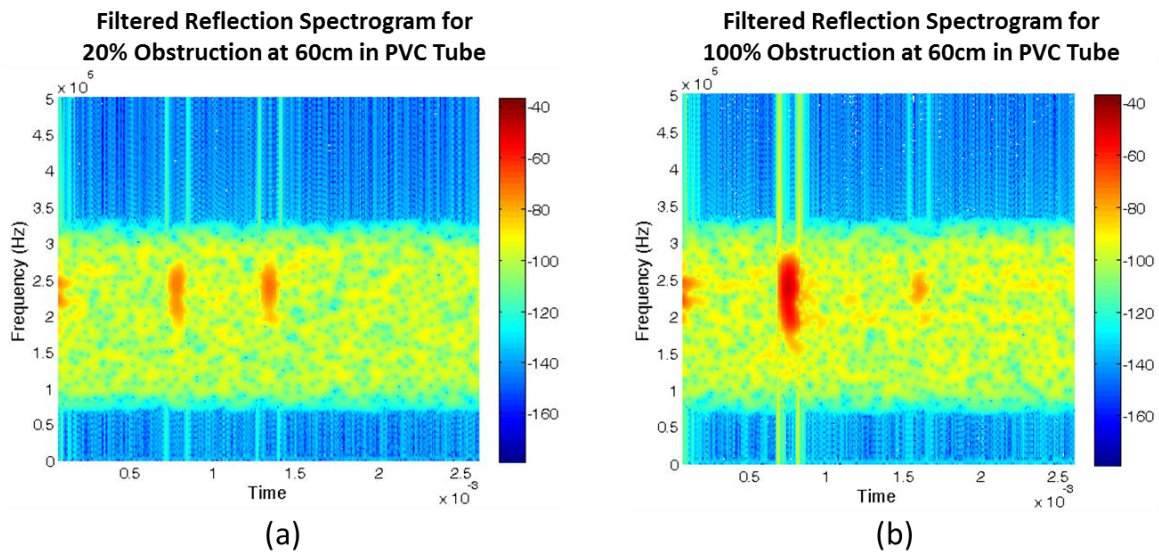


Figure 4-11 Spectrograms of an obstruction reflection of 20% (a) and 100% (b) size located at 60 cm from Hyd. in a water-filled copper tube using a 200 kHz and 20 μ s acoustic pulse.

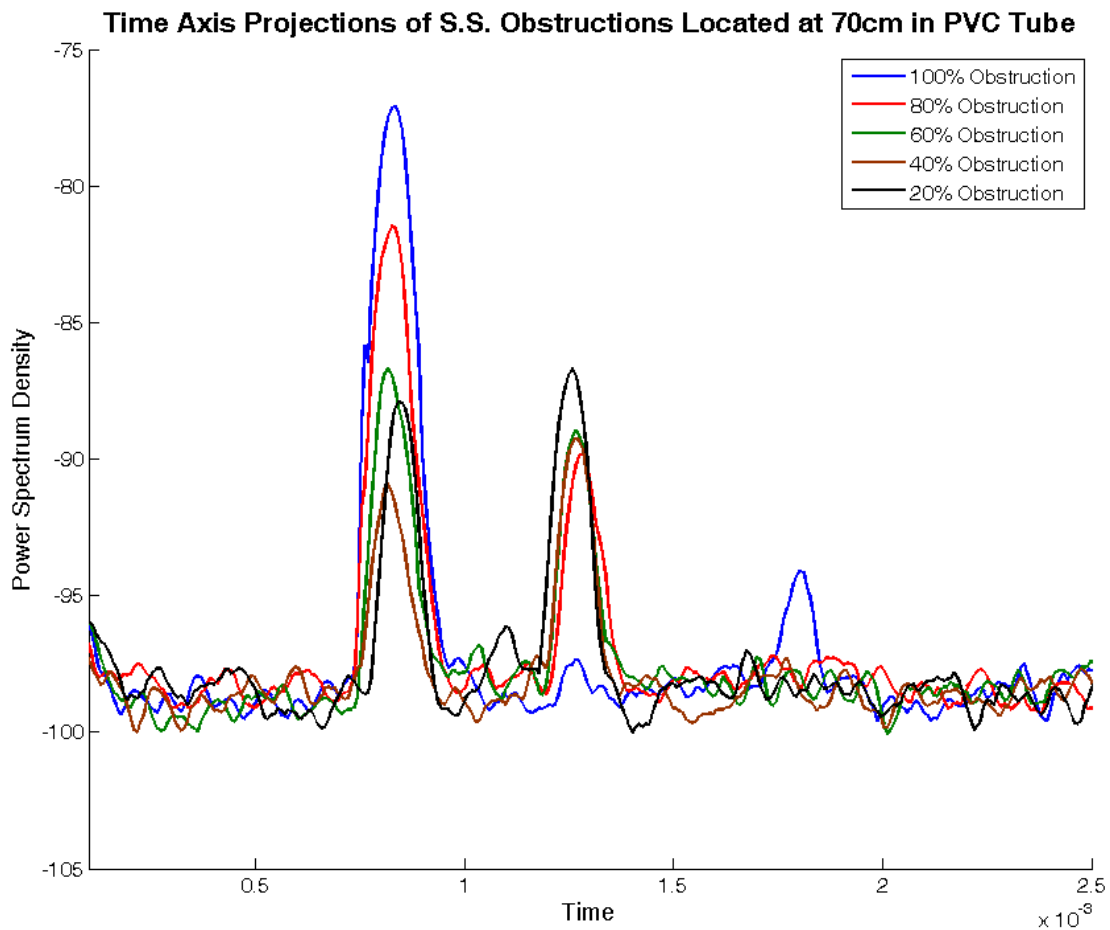


Figure 4-12 Graph of the time axis projections of the Spectrogram for the S.S. obstruction sizes used (100% blue, 80% red, 60% green, 40% brown and 20% black). The time projection calculation was performed in MATLAB, cropping the electric crosstalk. At 1.3 ms an increased in the PSD is observed as expected for the water level of 1 meter from the Hyd.

Figure 4-12 depicts the spectrogram time axis projection for five different S.S. obstruction sizes at 70cm from the hydrophone, where each power spectrum can be distinguished from each other. In the time projection the 100% obstruction (blue line) had the highest power density value in the first peak of the reflection (0.7 ms), while the 40% obstruction (brown line) had the lowest one. A second PSD peak area can be noticed in 1.3 ms which belongs to the reflection produced by the water level, since the small obstructions let part of the acoustic pulse passes through them. This graph also can be used to calculate the time at where the reflection occurs, leading to location estimation as well.

4.1.2.2.2 Reflection Signal Envelope

The reflections envelope is the second feature that was extracted from the recorded signals. Figure 4-13 shows the reflection envelopes for an S.S. obstruction of 40% size located at 40cm and 70cm. The first reflection measured in both (a) and (b) belongs to the 40% S.S. obstruction located in the PVC tube. As mentioned before as the obstruction position is far from the hydrophone the reflection occurs later. Also small obstructions allowed passing a portion of the incident signal. This results in a reflection approximately at 1.3ms, due to the water/air interface at the distal end of the PVC tube. Figure 4-14 demonstrate how the signal and envelope changes due to changes in obstruction sizes at the same distance. For larger cross sectional area obstructions the reflection produced is greater than smaller cross sectional area obstructions and vice versa. Finally, Figure 4-15 shows an example of the 5 S.S. obstructions reflection envelopes at a distance of 70cm from the hydrophone in the PVC tube. As observed and expected from theory and experiments, larger obstructions produced greater reflections, resulting in a characterization of envelopes as functions of obstruction type, size and position.

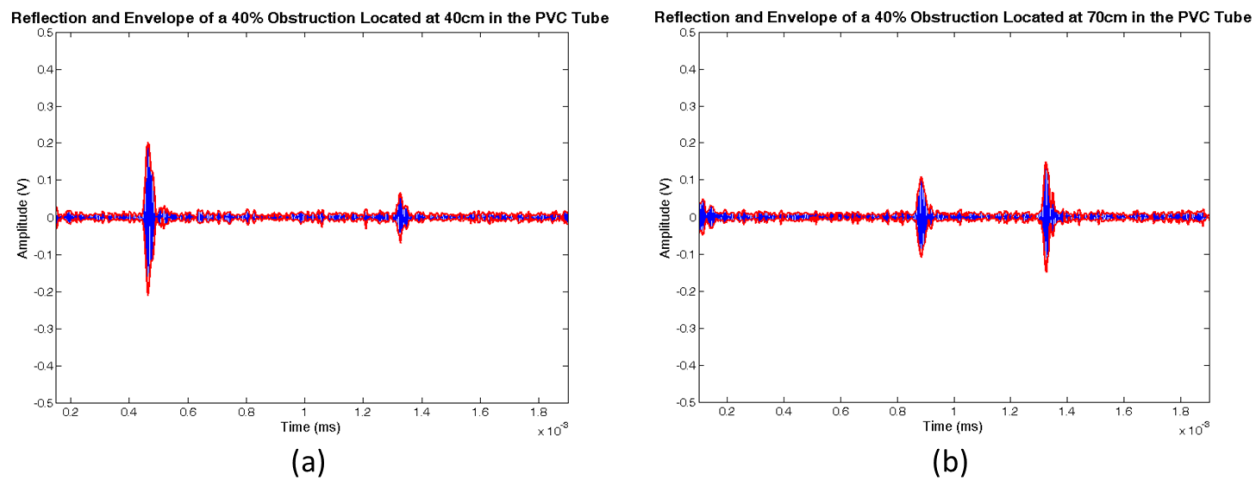


Figure 4-13 Reflections Envelope (red line) of an S.S. obstruction reflection of 40% size at 40cm (a) and 70cm (b) in a water-filled PVC tube using a 200 kHz and 20 μ s acoustic pulse. The reflection that occurred at approx. at 1.3ms in both (a) and (b), belongs to the water/air interface at the distal end of the PVC tube.

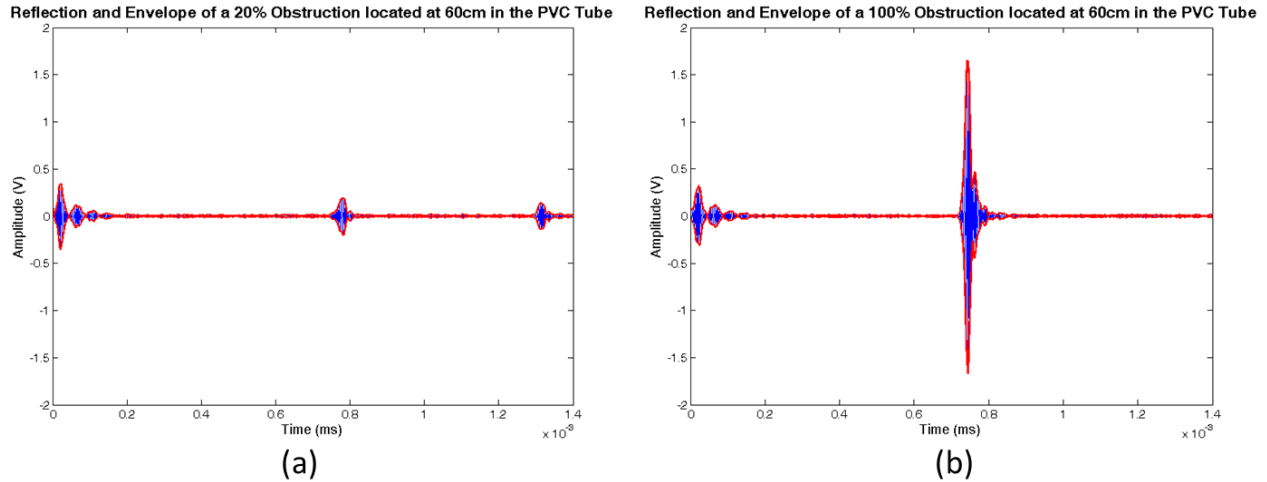


Figure 4-14 Reflections Envelope (red line) of an S.S. obstruction reflection of 20% (a) and 100% (b) size located at 60cm in a water-filled PVC tube using a 200 kHz and $20\mu\text{s}$ acoustic pulse. The reflection that occurred at approx. at 0.75ms in both (a) and (b) belongs to the echo produced by the 20% and 100% obstructions.

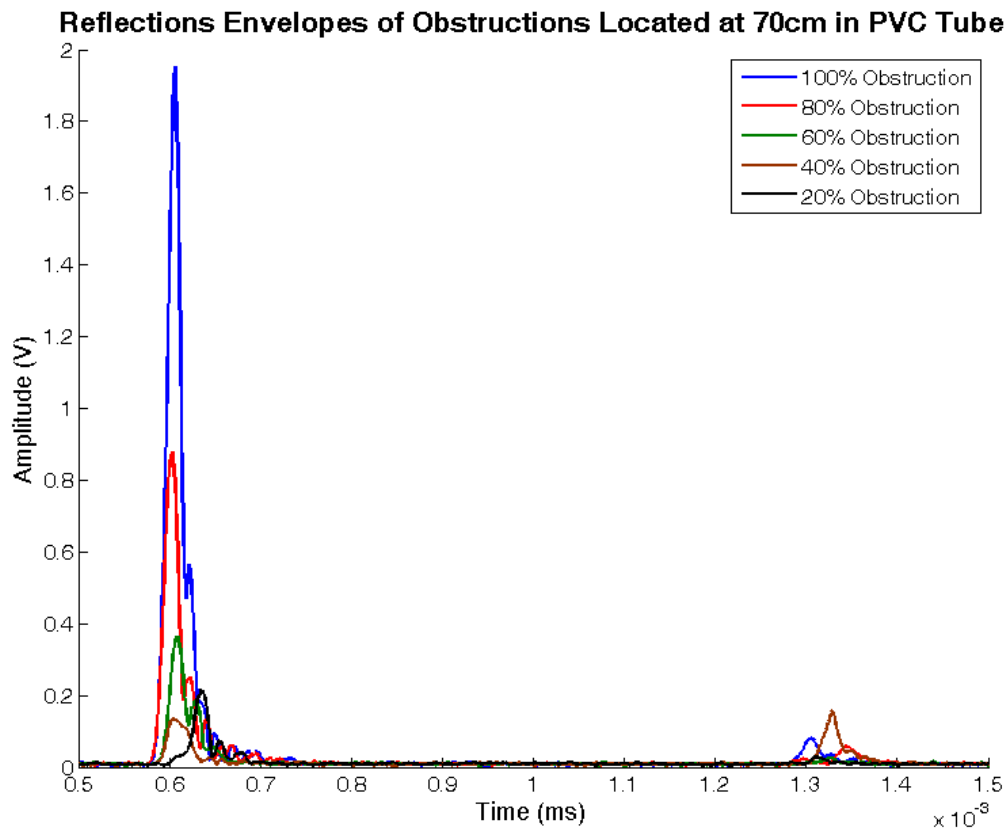


Figure 4-15 Graph of the reflection envelopes for the S.S. obstruction sizes used (100% blue, 80% red, 60% green, 40% brown and 20% black). The reflections envelope was performed in MATLAB, cropping the electric crosstalk. At 1.3ms an increased in amplitude is observed as expected for the water level of 1 meter from the Hyd.

4.1.2.2.3 Extracted Features as a Function of Obstruction Type

The main difference between reflections produced by stainless steel and Delrin obstructions is its amplitude. A Delrin obstruction has an acoustic impedance of 3.45 MRayls, much lower than stainless steel obstruction which is 36.23 MRayls. Consequently, lower intensity reflections are generated by Delrin obstructions as Figure 4-16 and 4-17 presents. Figure 4-16 shows the time-axis projections for the two obstructions types, stainless steel (a) and Delrin (b), at a distance of 70cm in the PVC tube. Similarly, Figure 4-17 illustrates the reflection envelopes for stainless steel (a) and Delrin (b) obstructions located at 70cm in the PVC tube. As observed in both figures, Delrin obstructions produced lower intensity reflections, therefore this characteristic was helpful to distinguish the obstruction type inside the PVC tube.

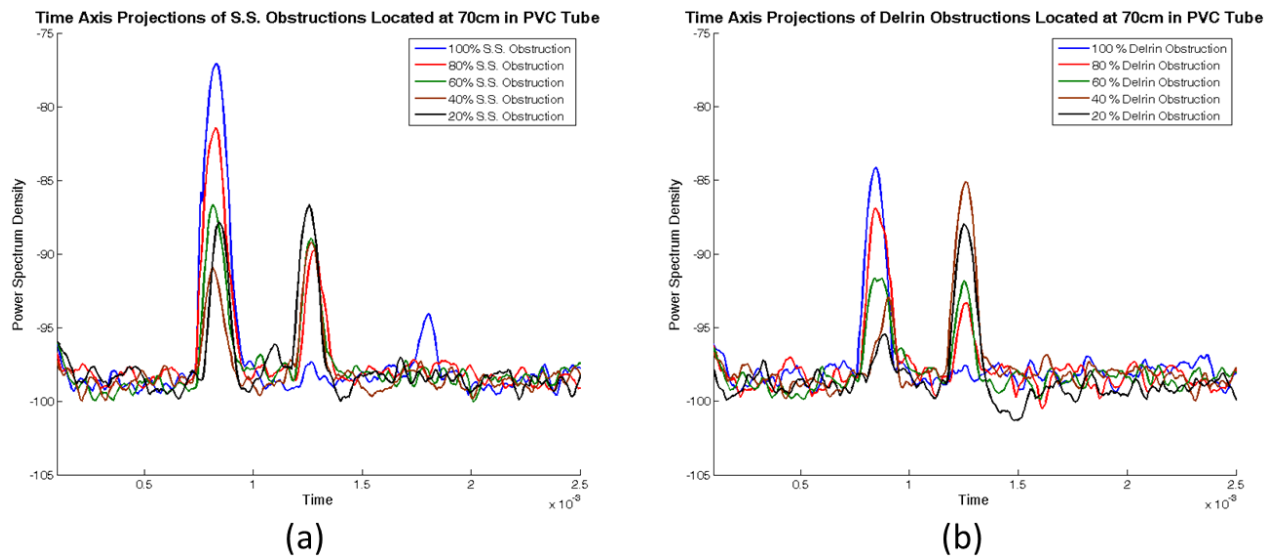


Figure 4-16 Spectrogram time axis projections of (a) S.S. and (b) Delrin obstructions located at 70cm in the PVC tube. Reflections produced by Delrin obstructions have a lower intensity than S.S. obstructions as expected, since the acoustic impedance of Delrin is lower than S.S.

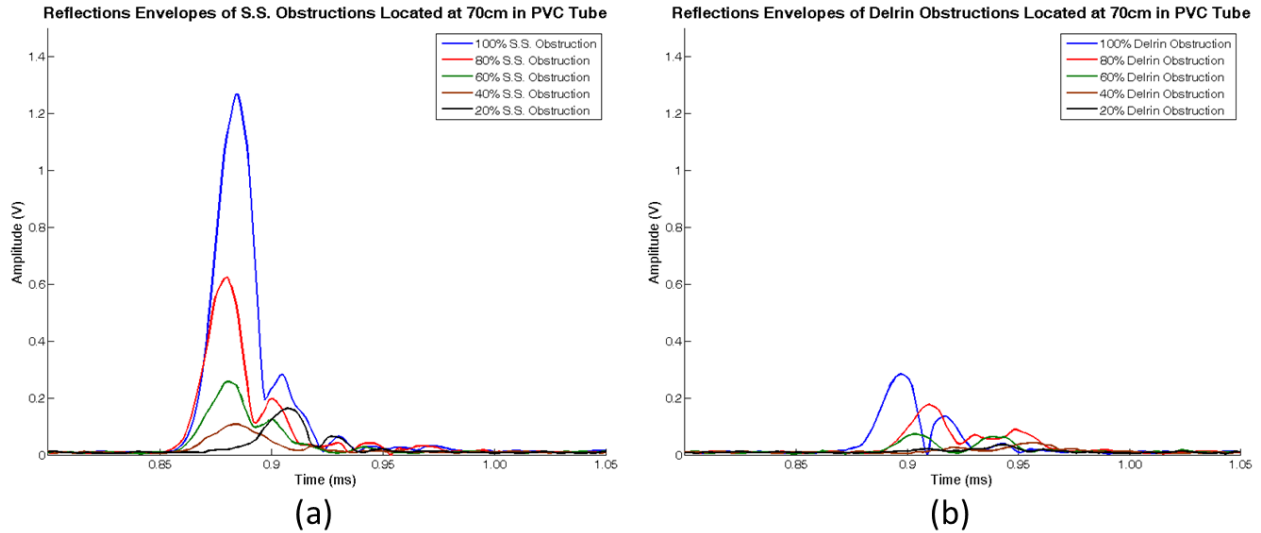


Figure 4-17 Reflections Envelopes of (a) S.S. and (b) Delrin obstructions located at 70cm in the PVC tube. Reflections produced by Delrin obstructions have a lower intensity compared to S.S. obstructions as expected, since the acoustic impedance of Delrin is lower than S.S.

4.1.3 Signal Matching Algorithm

The signal matching is the last process in the framework presented in Figure 3-9 to achieve obstruction detection. The algorithm basically compares the extracted features of an unknown acoustic reflection with the features stored in the database. This comparison is performed using the Euclidean Distance (Equation 3.5) formula between features, and then finding the lowest distance.

4.1.3.1 Database Creation

Reflections for the different obstructions were recorded varying its position along the water-filled PVC tube, according to Section 3.3. Then, using the spectrogram time axis projection and signal envelope, a database with these features or acoustic signature was created and stored. Thus, the database contains the features of reflection produced by Stainless Steel and Delrin obstructions with sizes from 20% to 100% for different location along the water-filled PVC tube. Figure 4-18 shows the process to create and store the features database.

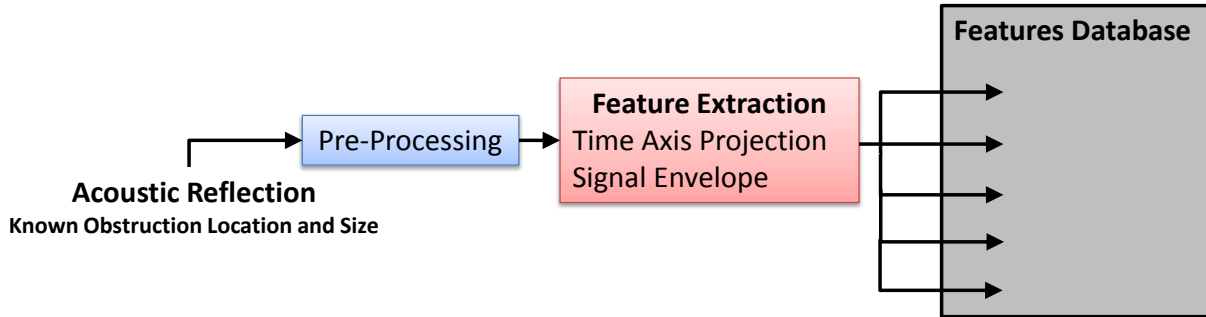


Figure 4-18 Process to create and store the features database.

4.1.3.2 Signal Matching Results

Ten measurements were recorded for each obstruction type, size and position, and were processed by the signal matching algorithm to test the reliability of the method for obstruction recognition. Figure 4-19 shows the feature database of the spectrogram time axis projections (solid lines) for the S.S. obstructions located at 50cm from the hydrophone in the water-filled PVC tube. The dashed line in the figure is the obstruction reflection that is being processed by the algorithm to find the best match within the database. The lower Euclidean distance between the obstruction reflection and the database was 29.02, showing that the obstruction reflection was closest to the 100% S.S. obstruction located at 50cm in the PVC tube which was the real type, size and position of the obstruction. The main difference observed in Figure 4-19 is the magnitude of the reflection PSD peak at the moment that the reflection occurred, approximately at 0.5ms. An overlap is also observed between the reflection processed by the algorithm and the 100% obstruction (blue line) stored in the database pointing out the expected signal matching.

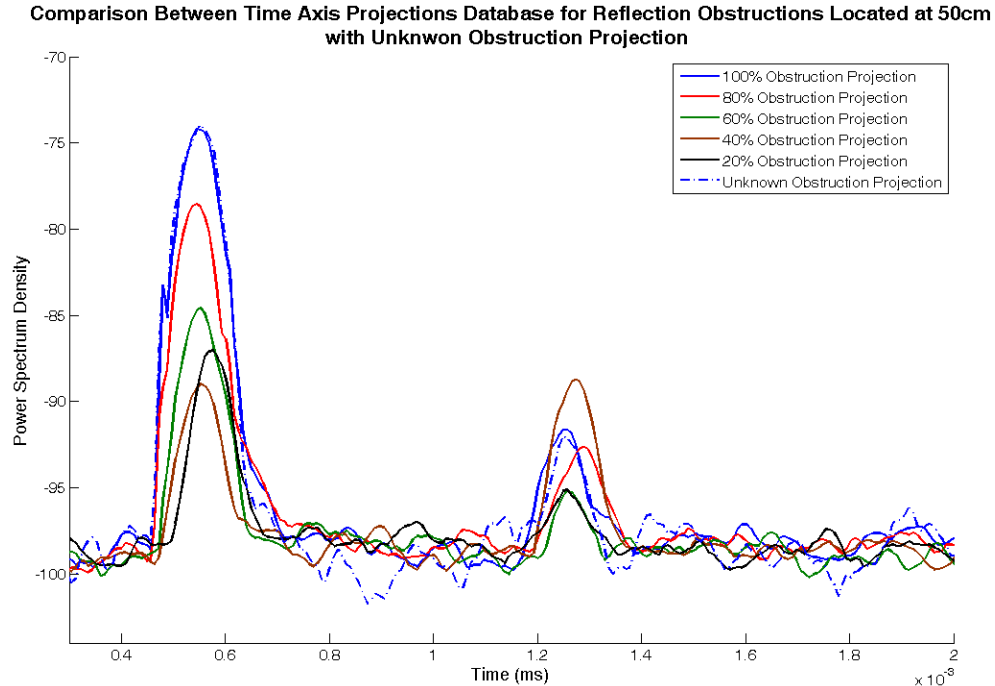


Figure 4-19 Comparison between the time axis projection feature of an unknown obstruction reflection and the reflections database. The reflection database presented is for S.S. obstructions located at 50cm from the hydrophone in the water-filled PVC tube. The unknown reflection (dashed blue line) is closest to the 100% S.S. obstruction (blue line), overlapping in the PSD peak, resulting on a Euclidian distance of 29.02.

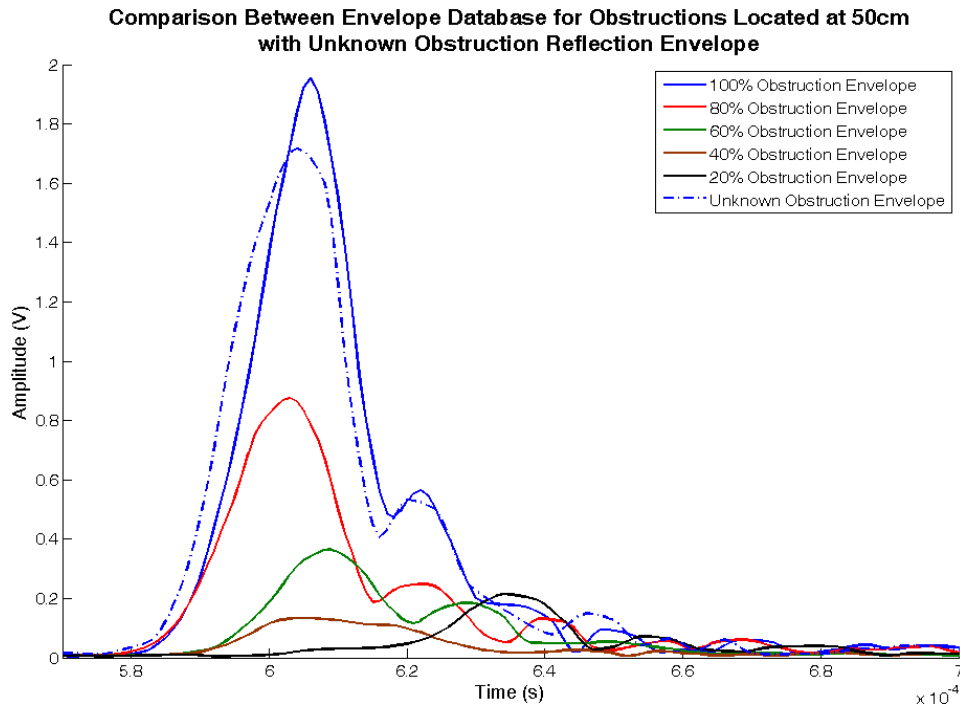


Figure 4-20 Comparison between the envelope feature of an unknown obstruction reflection and the envelope reflection database. The reflection database presented is for S.S. obstructions located at 50cm from the hydrophone in the water-filled PVC tube. The unknown reflection envelope (dashed blue line) is closest to the 100% S.S. obstruction (blue line) resulting on a Euclidian distance of 4.02.

Figure 4-20 presents the other reflections feature stored in the database, which is the reflection envelope. The dashed blue line is the envelope extracted from a reflection of a 100% S.S. obstruction at 50cm in the PVC tube. Comparing the extracted envelope with the envelope database, the lowest Euclidean distance was 4.02 between the extracted envelope and the 100% S.S. obstruction at 50cm stored in the database. Hence a correct obstruction type, location and size detection by the algorithm. Similar to Figure 4-17 the main difference between different obstruction size envelopes at a particular distance is the amplitude. As Equation 2.6 states larger changes in cross sectional area inside the tube results in higher reflection coefficients. This was experimentally showed in Figure 4-19 and 4-20, where reflections with greater amplitude were measured for larger obstruction sizes.

Each of the 10 measurements for every location was processed and analyzed by both algorithms to estimate the obstruction type, location and size by comparing the extracted features to the features database. Figures 4-21 and 4-22 present the correct prediction percentage of the 100% S.S. obstruction measurements along the PVC tube. From both figures is observed that the obstruction location (blue bar) and type (green bar) was determined correctly at all distances. The obstruction size (red bar) was detected with an accuracy of 95.3% using the envelope feature as Figure 4-21 shows. While using the time axis projection feature, the accuracy was 99.3% to detect the obstruction size (Figure 4-22).

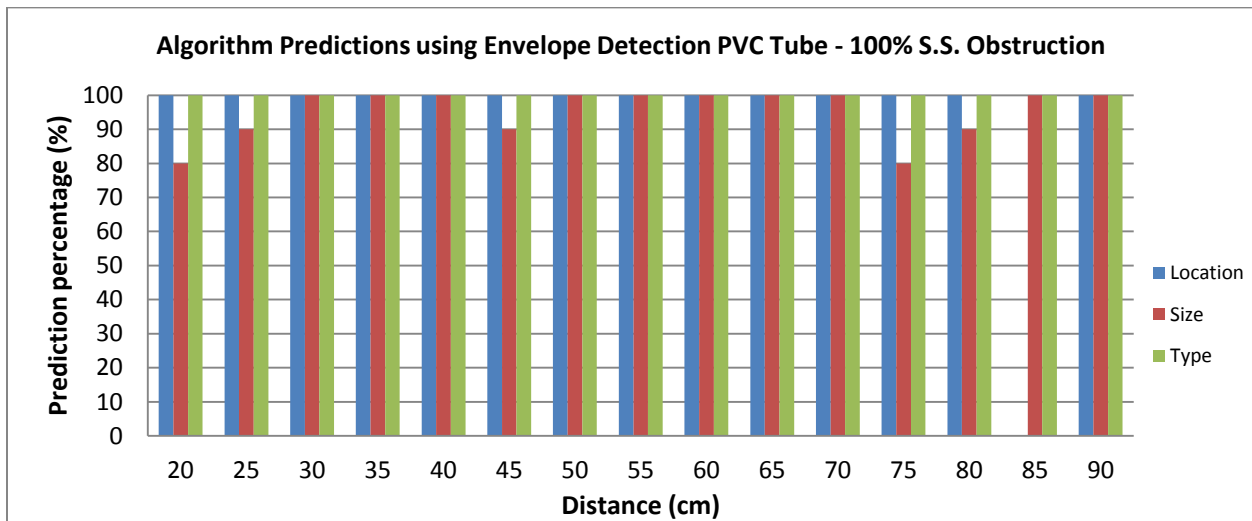


Figure 4-21 Prediction percentage of the Envelope Detection algorithm to recognize 100% S.S. obstruction at different locations along the water-filled PVC tube. Location predictions are plotted in the blue bar, size in the red bar and type in green bar.

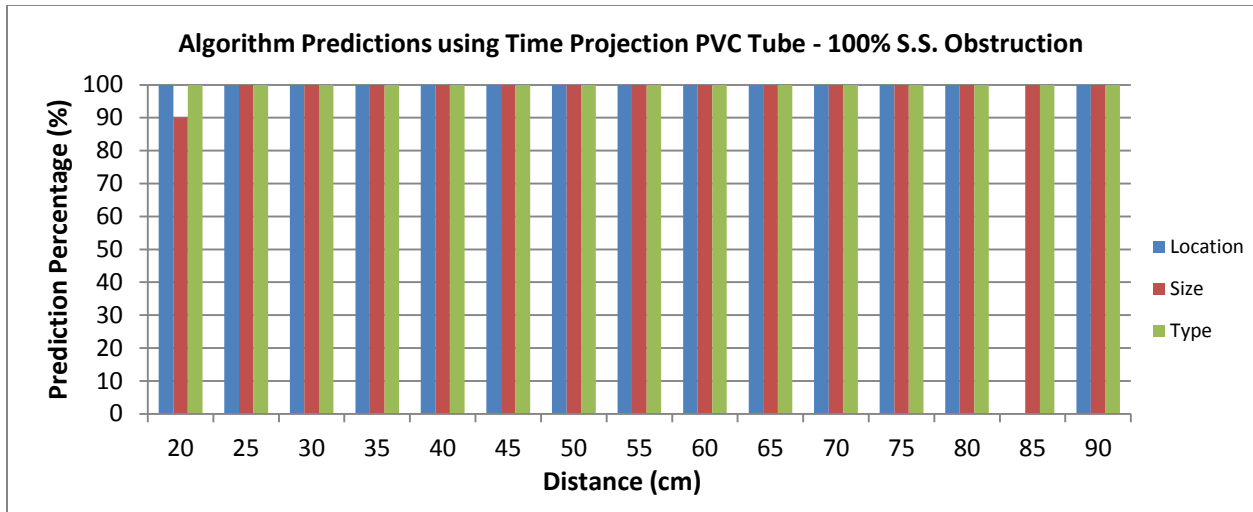


Figure 4-22 Prediction percentage of the Time Projection algorithm to recognize 100% S.S. obstruction at different locations along the water-filled PVC tube. Location predictions are plotted in the blue bar, size in the red bar and type in green bar.

In order to identify where the incorrect obstruction size detections were located, a histogram was generated for each feature extraction method. The histogram shows how the algorithm results are organized in 5 bins (100%, 80%, 60%, 40% and 20%). Each bin represents the obstruction size possibilities stored in the database. Figure 4-23a indicates that using the envelope feature to detect the 100% S.S. obstruction, 143 measurements out of 150 were identified correctly. Figure 4-23b presents the histogram using the time projection feature which results in 149 measurements out of 150 identified correctly by the algorithm. The incorrect results were identified by the algorithms as 80% size obstructions.

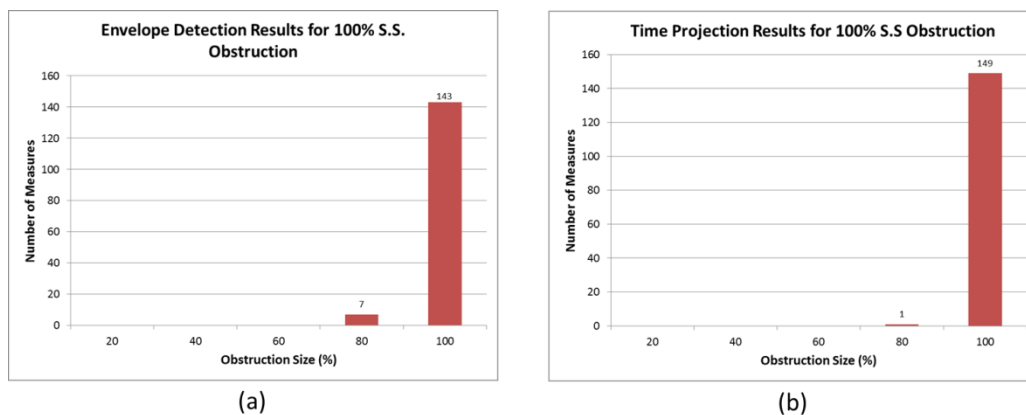


Figure 4-23 Histograms of the reflections processed by the Envelope Detection (a) and Time Projection (b) algorithms to detect 100% obstruction in the water-filled PVC tube. Ten reflections were recorded for each of the 16 positions along the PVC tube, resulting on 160 reflections processed by each algorithm.

The algorithms error detecting the obstruction location and size are shown in Figure 4-24 and Figure 4-25, respectively. A positive error value means that the algorithm result was overestimated and vice versa. For the 100% S.S. obstruction reflections processed by both algorithms, the location error was zero for all positions along the PVC tube, except for the distance of 85cm that was 5 ± 0 cm. Meanwhile, using the time axis projection (green line) for obstruction size detection, results with less error than using the envelope (blue line) as shown in Figure 4-25. The overall error using the envelope feature was -0.93 ± 2.23 % (mean \pm STD) and for the time-axis projection was -0.13 ± 0.39 % (mean \pm STD). At 20cm was the only location where time projection detected incorrectly the obstruction size, giving a -2 % size error with a standard deviation of 6.32%. This standard deviation shows that the algorithm results were closed to the error mean and the data is not dispersed. For locations of 20, 25, 45, 75 and 80 cm, using the envelope feature (blue line) to detect the obstruction size, results in errors of -4 ± 8.43 % (mean \pm STD) or less. It is important to point out that the algorithm results are discrete since the database was created for discrete values of obstruction type, size and positions. This needs to be kept in perspective when analyzing and discussing the results.

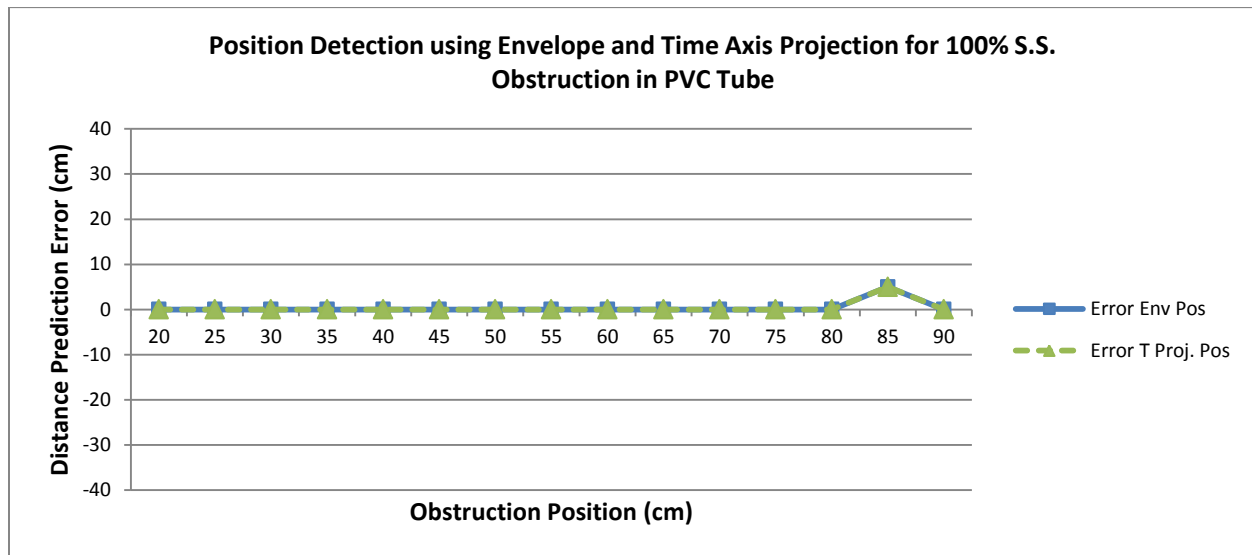


Figure 4-24 Obstruction position detection error using envelope detection (blue line) and Time Projection (green line) algorithms for 100% obstruction. Positive error values means overestimation of the real values and negative error values means underestimation. The error was zero for all locations, except for 85cm which was 5cm for both features.

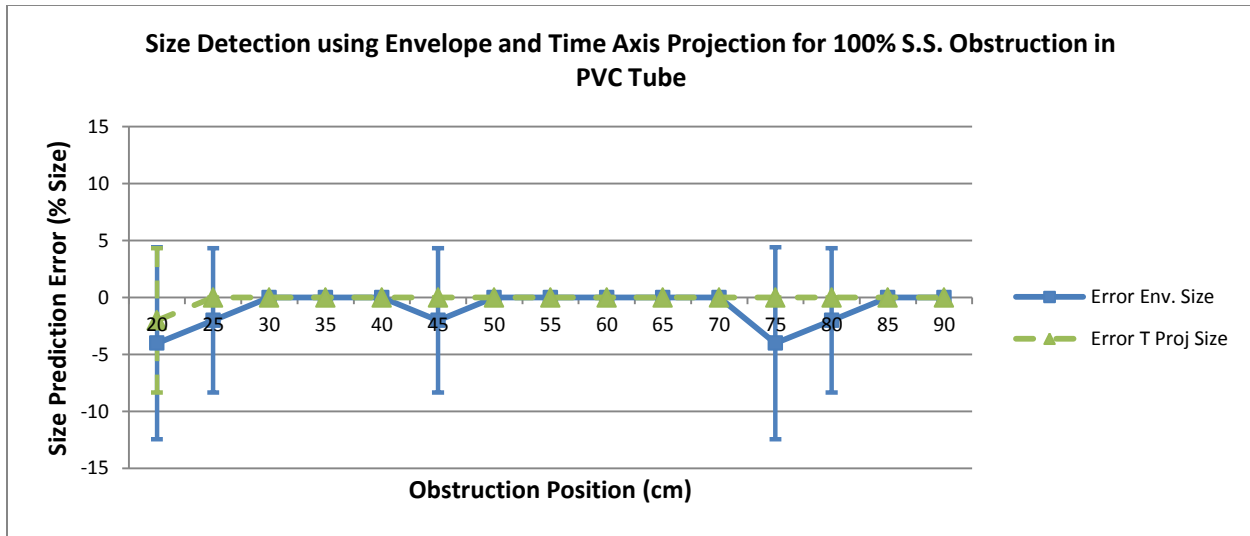


Figure 4-25 Obstruction size detection error using envelope detection (blue line) and Time Projection (green line) algorithms for S.S. 100% obstruction. Standard deviations of each error are also presented. Time projection feature results on less error than the envelope feature to detect obstruction size. The overall error using the envelope feature was -0.93 ± 2.38 % (mean \pm STD) and for the time-axis projection was -0.13 ± 0.42 % (mean \pm STD).

Figure 4-26 to 4-33 presents the distance and size error predictions for S.S. obstructions from 80% to 20% size. For 80% S.S. obstruction size, the distance error was zero at all distances except for 85 cm, similar to the 100% obstruction using both methods. The size prediction errors for 80% S.S. obstruction, shown in Figure 4-27, increases as the obstruction position increases using both methods. In this case, time-axis projection results in slightly lower overall error of -3.2 ± 5.52 % (mean \pm STD) compared with the -3.6 ± 2.30 % (mean \pm STD) signal envelope error. Figure 4-28 shows the distance prediction using both methods for 60% S.S. obstruction, which was estimated correctly at all locations except for 85cm, as 80% and 100% S.S. obstructions. For the size detection errors presented in Figure 4-29, it is observed that signal envelope have negative errors at 50 and 60 cm, while the time-axis method results in negative errors from 25cm to 70cm. Consequently, the overall error using the envelope feature to detect 60% S.S. obstruction was -2.8 ± 0.98 % (mean \pm STD), much lower than the time-axis projection that was 7.46 ± 5.77 % (mean \pm STD). Figure 4-30 and 4-32 shows the distance predictions error for 40% S.S. obstruction and 20% S.S. obstruction respectively. For both obstructions the distances error were similar using the signal envelope and time-axis projection features. The overall error for 40% S.S. obstruction using the signal envelope was 3.7 ± 1.38 cm (mean \pm STD) and using time projection

was $4.06 \pm 1.38\text{cm}$ (mean \pm STD). While for 20% S.S. obstruction the average error using the envelope feature was $4.06 \pm 1.17\text{ cm}$ (mean \pm STD) and using time projection was $4.26 \pm 1.33\text{ cm}$ (mean \pm STD). Figure 4-31 shows that using both features for 40% S.S. obstruction size detection, the error increases as obstruction distances increases. Using the time-axis projection to detect the size for the 20% S.S. obstruction results in a considerably lower error with an overall of $1.33 \pm 6.65\%$ (mean \pm STD), than using the signal envelope with an overall error of $30.8 \pm 2.96\%$ (mean \pm STD).

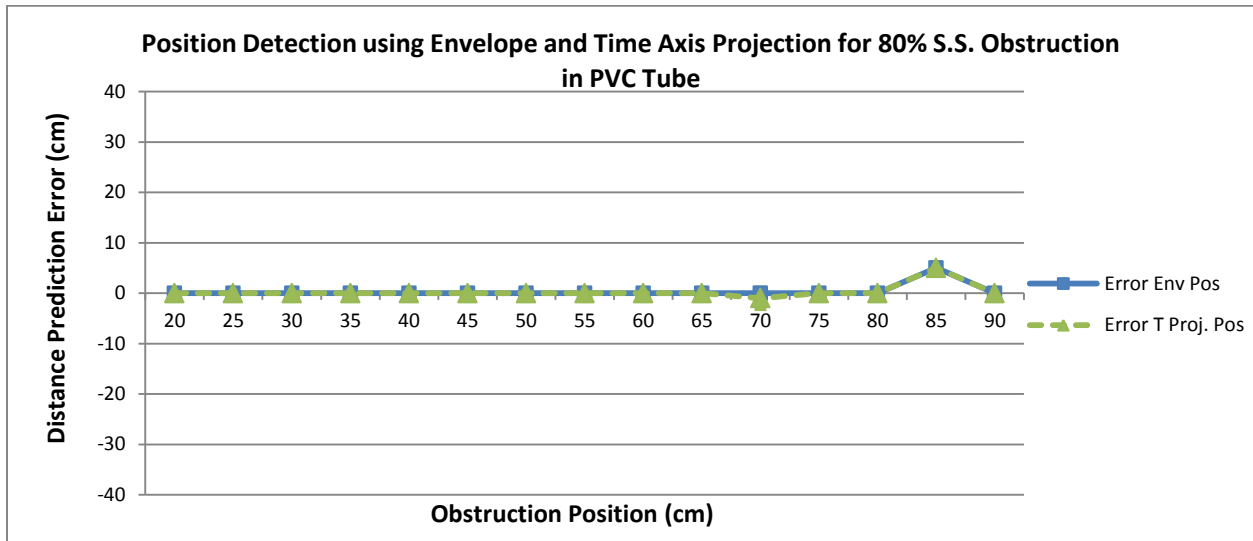


Figure 4-26 80% S.S. Obstruction position detection error using envelope detection (blue line) and Time Projection (green line) algorithms for 80% S.S. obstruction. The error was zero for all locations, except for 85cm which was 5cm for both features.

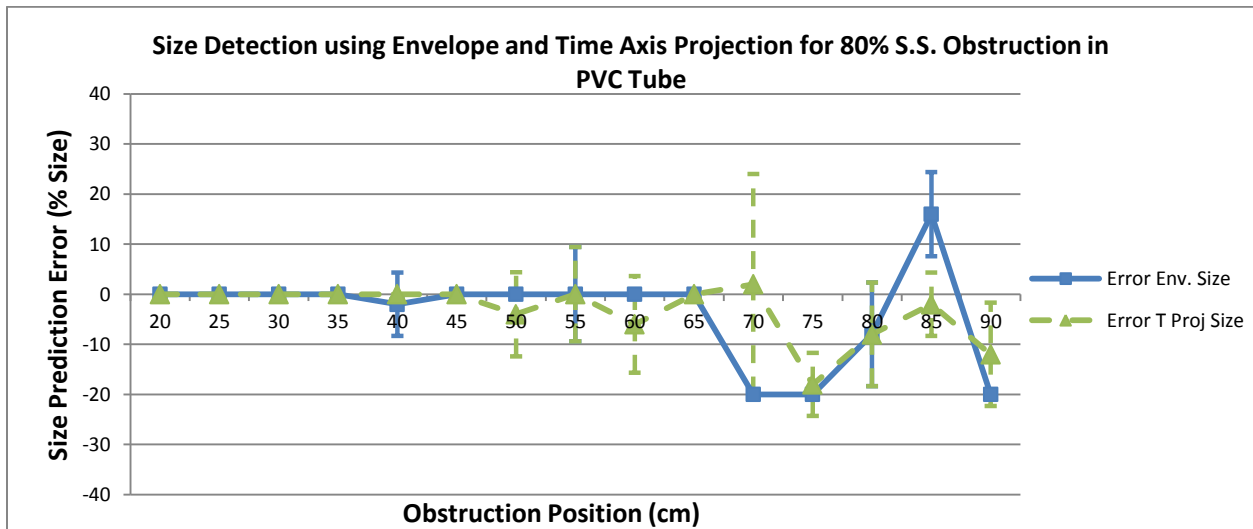


Figure 4-27 80% S.S. Obstruction size detection error using envelope detection (blue line) and Time Projection (green line) algorithms. The overall error using the envelope feature was $-3.6 \pm 2.30\%$ (mean \pm STD) and for the

time-axis projection was $-3.2 \pm 5.52\%$ (mean \pm STD). Time-axis projection feature shows slightly lower errors than the envelope feature as the obstruction distances increases but with higher standard deviations.

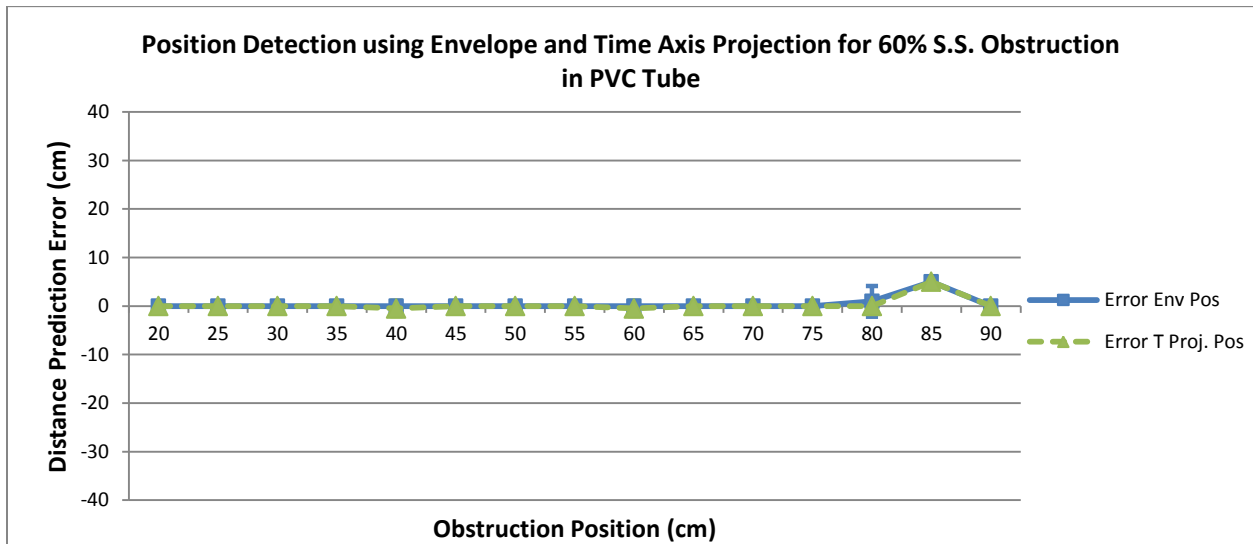


Figure 4-28 60% S.S. Obstruction distance detection error using envelope detection (blue line) and Time Projection (green line) algorithms. The error was zero for all locations, except for 80cm with an error of 1 ± 3.16 cm (mean \pm STD) for the envelope feature and at 85cm with an error 5cm for both features.

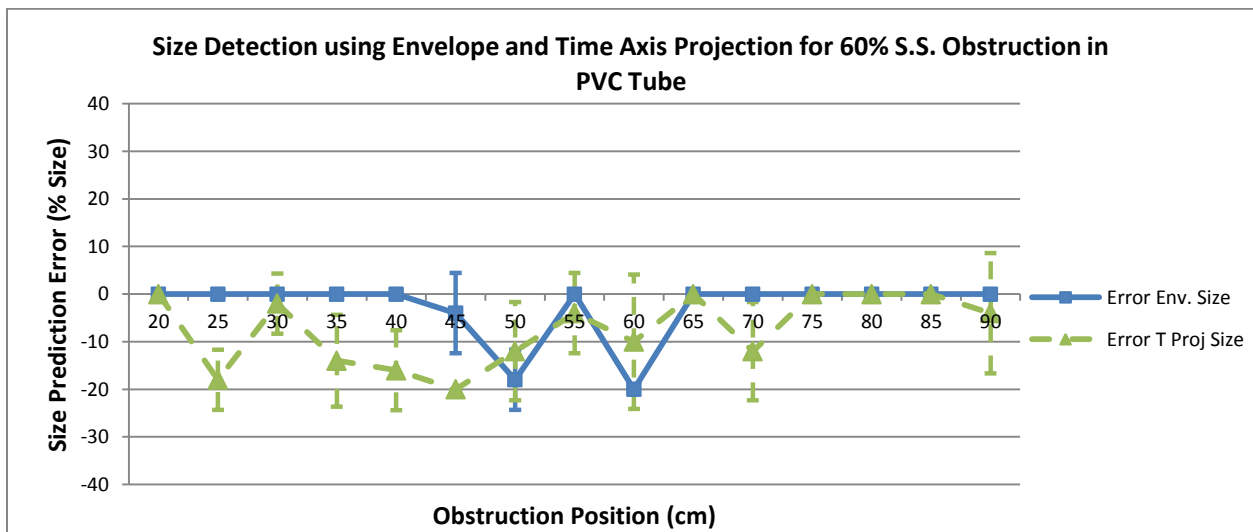


Figure 4-29 60% S.S. Obstruction size detection error using envelope detection (blue line) and Time Projection (green line) algorithms. The overall error using the envelope feature was $-2.8 \pm 0.98\%$ (mean \pm STD) and for the time-axis projection was $7.46 \pm 5.77\%$ (mean \pm STD).

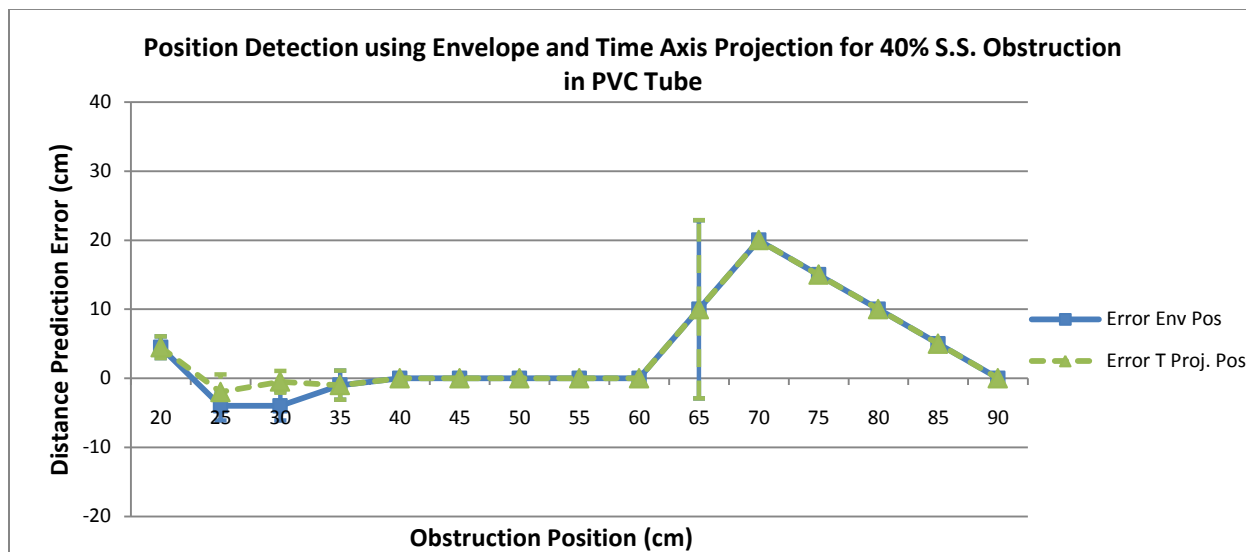


Figure 4-30 40% S.S. Obstruction distance detection error using envelope detection (blue line) and Time Projection (green line) algorithms. As obstructions become smaller and farther from the hydrophone the error increases for both features. Average error using the envelope feature was 3.7 ± 1.38 cm (mean \pm STD) and using time projection was 4.06 ± 1.38 cm (mean \pm STD).

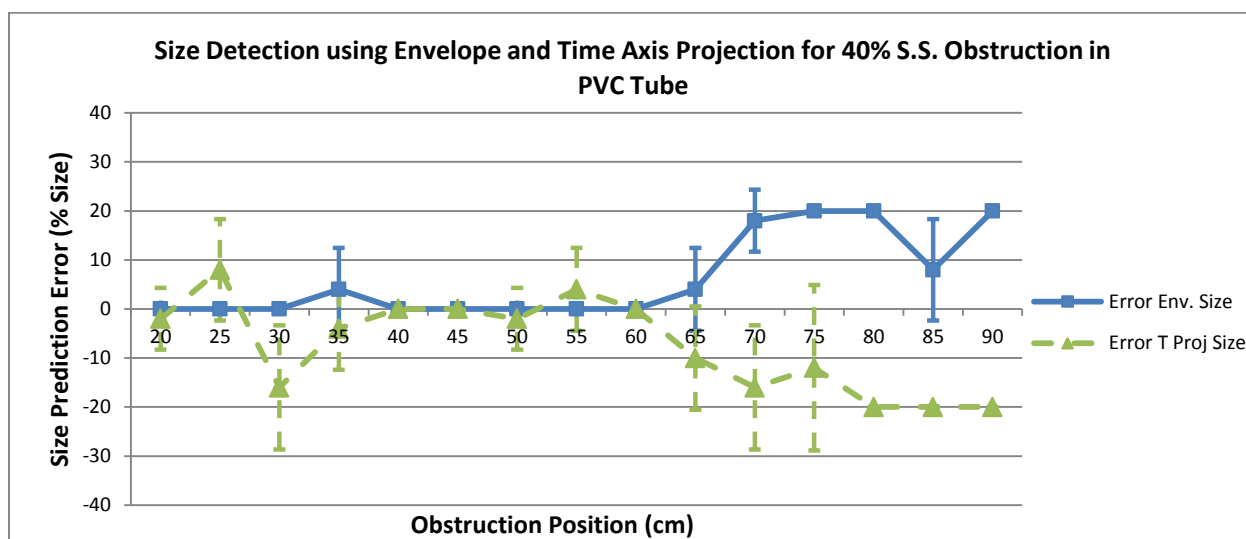


Figure 4-31 40% S.S. Obstruction size detection error using envelope detection (blue line) and Time Projection (green line) algorithms. The overall error using the envelope feature was 6.26 ± 2.23 % (mean \pm STD) and for the time-axis projection was -7.73 ± 6.16 % (mean \pm STD). As obstructions become smaller and farther from the hydrophone the error increases for both features.

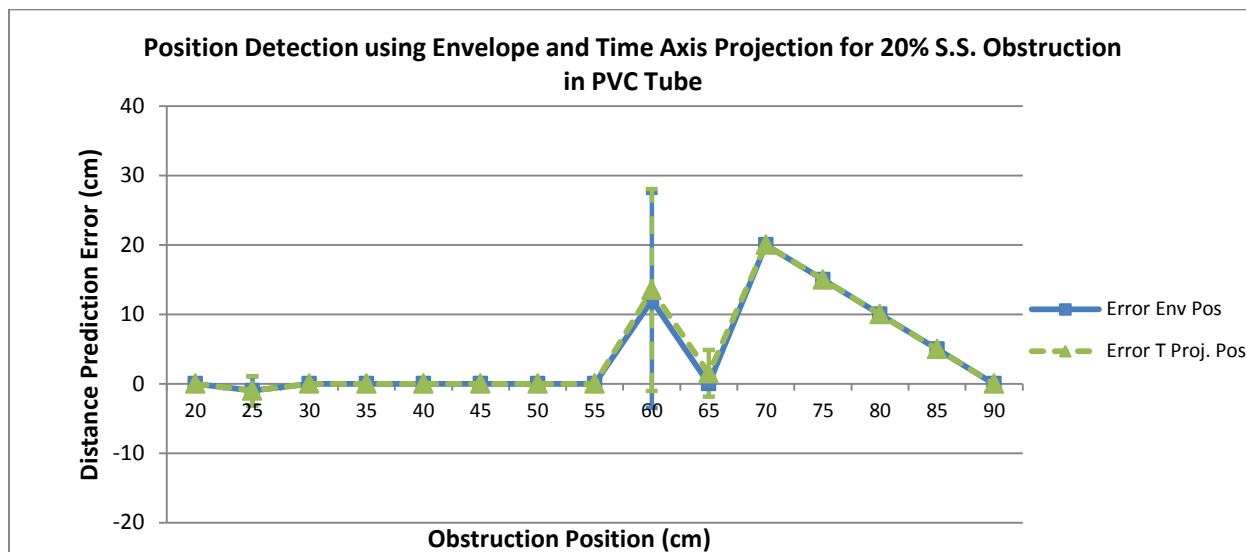


Figure 4-32 20% S.S. Obstruction distance detection error using envelope detection (blue line) and Time Projection (green line) algorithms. As obstructions become smaller and farther from the hydrophone the error increases for both features. Average error using the envelope feature was 4.06 ± 1.17 cm (mean \pm STD) and using time projection was 4.26 ± 1.33 cm (mean \pm STD).

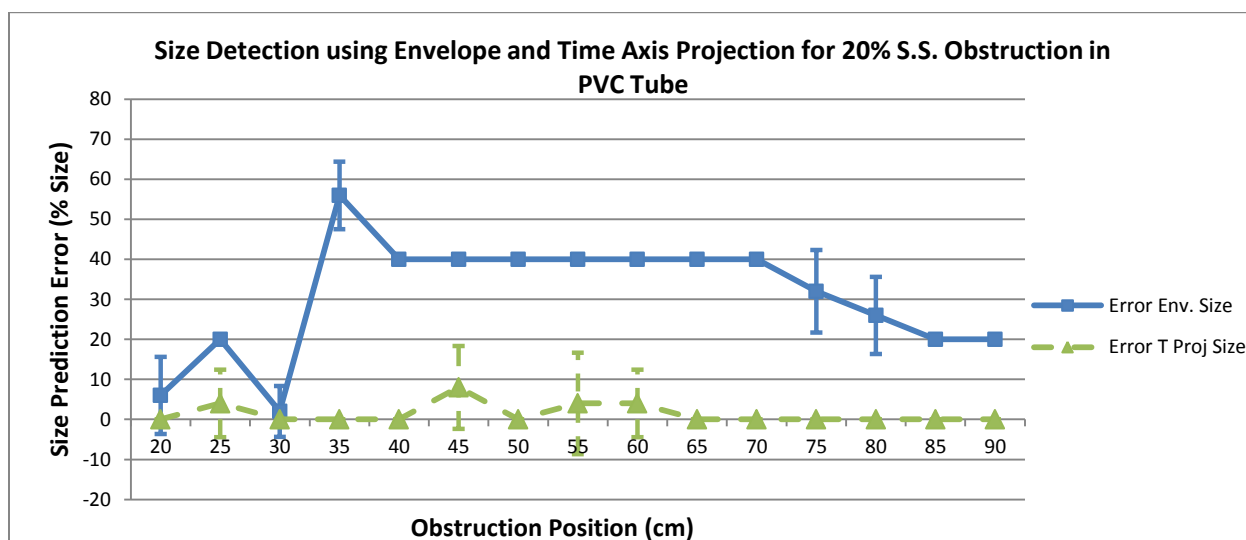


Figure 4-33 20% S.S. Obstruction size detection error using envelope detection (blue line) and Time Projection (green line) algorithms. The overall error using the envelope feature was 30.8 ± 2.96 % (mean \pm STD) and for the time-axis projection was 1.33 ± 6.65 % (mean \pm STD).

4.1.3.2.1 Signal Matching Algorithm Accuracy and Average Errors Detecting Stainless Steel Obstructions

Figure 4-34 summarizes the correct estimations using the envelope detection and time-axis projection to detect the obstruction type, position and size, located in the water-filled PVC tube. It is observed that by decreasing the obstruction size from 60% to 20% the accuracy detecting the obstruction type decreases (orange line). This incorrect estimation corresponds to the similarity between reflections produced by small S.S. obstructions and large Delrin obstructions. Figure 4-16 and 4-17 shows that extracted envelopes and time-axis projections of 60% to 20% S.S. obstructions are similar to 100% to 60% Delrin obstructions. This similarity results on an incorrect obstruction type prediction leading to an incorrect features database comparison. Therefore, the obstruction size and position are estimated incorrectly.

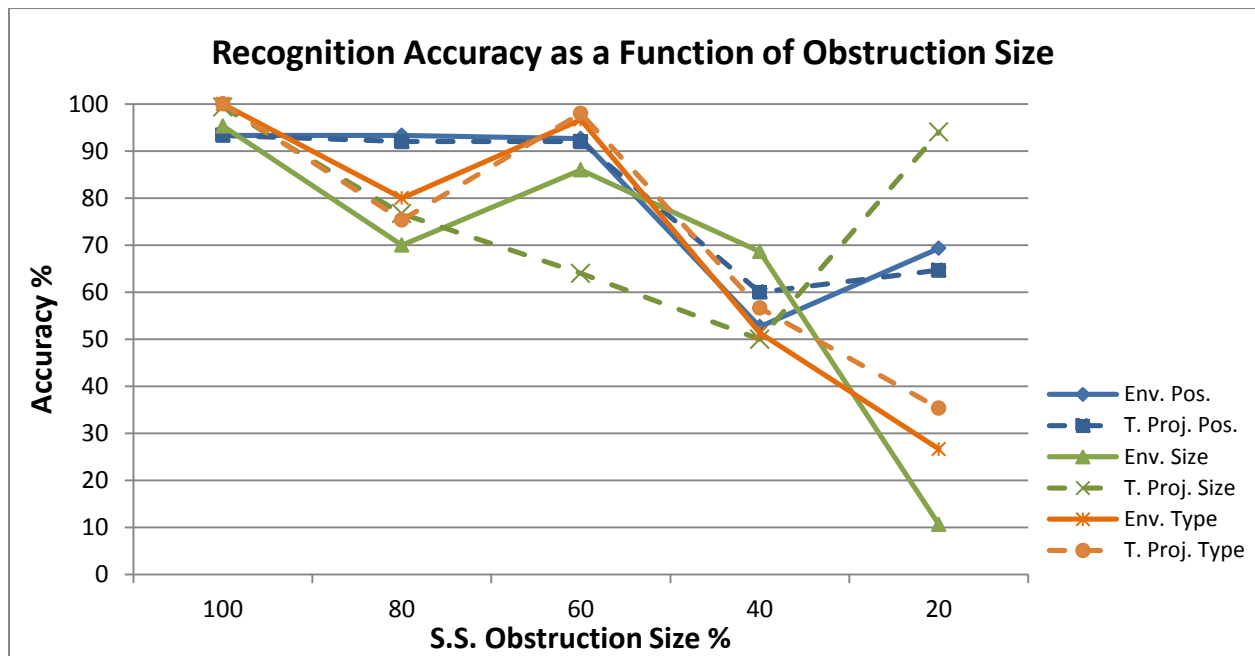


Figure 4-34 Algorithm accuracy using signal envelope and time-axis projection to detect stainless steel obstruction size, position and type in PVC tube. For 20% and 40% obstruction size the algorithm accuracy decreases due to similarity between reflections of small stainless steel obstructions and large Delrin obstructions.

To summarize where the incorrect S.S. obstructions positions were located, the average errors were plotted as function of obstruction position and size. Figure 4-35 and 4-36 summarize these average errors detecting the S.S. obstructions position in the water-filled PVC tube, using the envelope detection and time-axis projection. As Figure 4-35 shows, once the S.S. obstructions location reach 60cm the error increases up to 8 ± 0.42 cm at 70cm. In order to identify which of the S.S. obstructions has more effect in the increase of average error, Figure 4-36 presents the average error as a function of S.S. obstruction size. The figure shows that for 40% and 20% S.S. obstructions the average error increases up to 4.26 ± 1.33 cm (mean \pm STD) for 20% S.S. obstruction. In both figures, the average errors using the envelope and time-axis methods to estimate the S.S. obstructions position are similar. As mentioned, the envelope and time-axis projection of 40% and 20% obstructions are very similar to larger Delrin obstructions, which results on an increase in the average error of distance estimation.

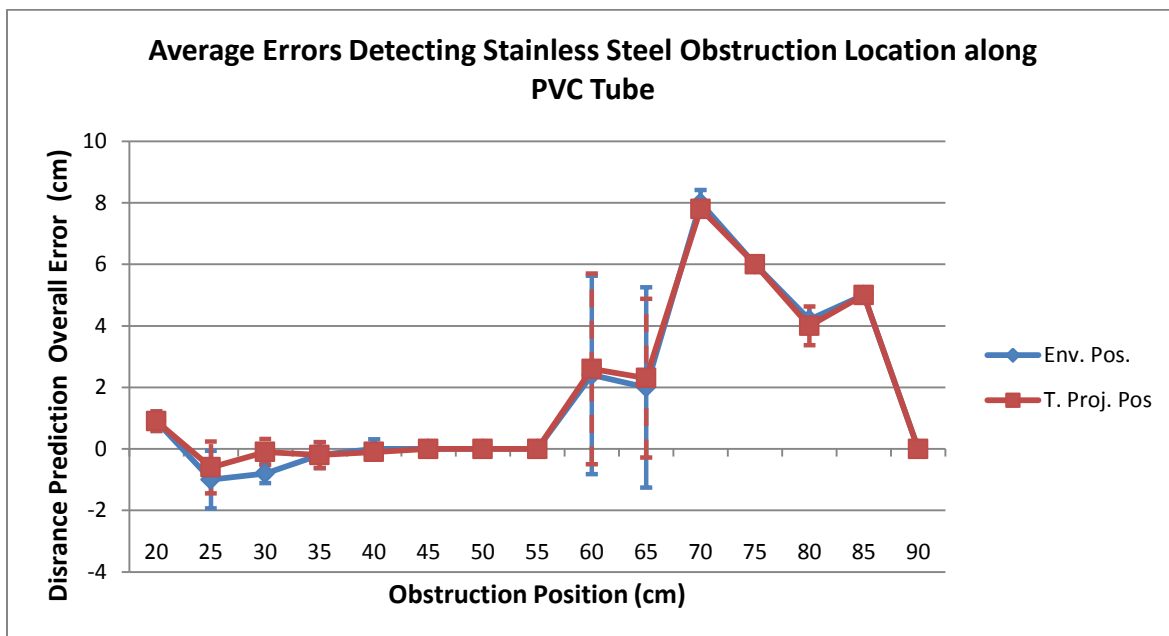


Figure 4-35 Average errors detecting S.S. obstructions position in water-filled PVC tube, using the envelope detection and time-axis projection. From 60cm onwards, the overall distance prediction error increases up to 8 ± 0.42 cm (mean \pm STD) at 70cm. Both features results in similar error values detecting the S.S. obstructions positions along the PVC tube.

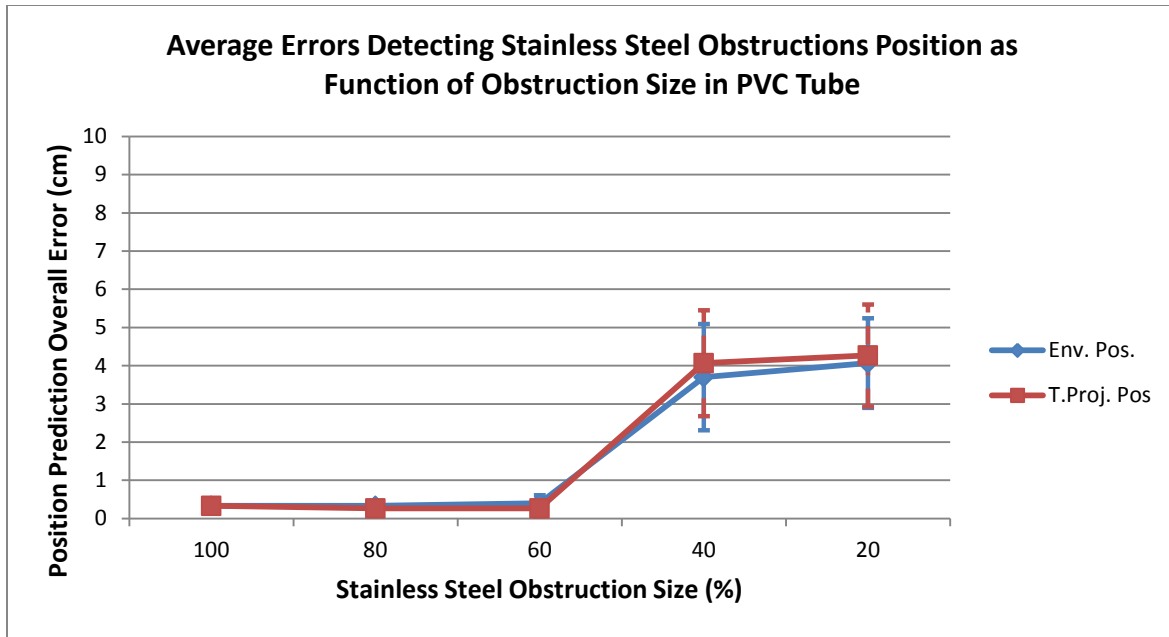


Figure 4-36 Average errors detecting S.S. obstructions position as function of obstruction size in water-filled PVC tube. For 40% and 20% S.S. obstructions, the average error detecting the obstruction position increases up to 4.26 ± 1.33 cm (mean \pm STD) for 20% obstruction. Both features results in similar error values detecting the S.S. obstructions positions along the PVC tube.

The same procedure was performed to summarize the average errors detecting the S.S. obstructions size, as function of obstruction position and size. Figure 4-37 shows the size prediction average error as a function of obstruction position, where it is observed that the envelope detection overestimates the obstruction real size with an overall error of 5.94 ± 2.17 % (mean \pm STD). While the time-axis projection underestimates the obstruction real size, with an overall error of -3.36 ± 4.10 % (mean \pm STD). Figure 4-38 shows that the obstruction size error was mainly produced by the 20% S.S. obstruction using the envelope detection, with an error of 30.8 ± 2.96 % (mean \pm STD). The time-axis projection error for 20% S.S. obstruction size detection was 3.7 ± 1.38 % (mean \pm STD), much lower than using the envelope. Therefore, for the water-filled PVC tube the time-axis projection estimates better 20% S.S. obstruction. However, the error for small S.S. obstructions is produced by the incorrect estimation of the obstruction type, presented in Figure 4-34.

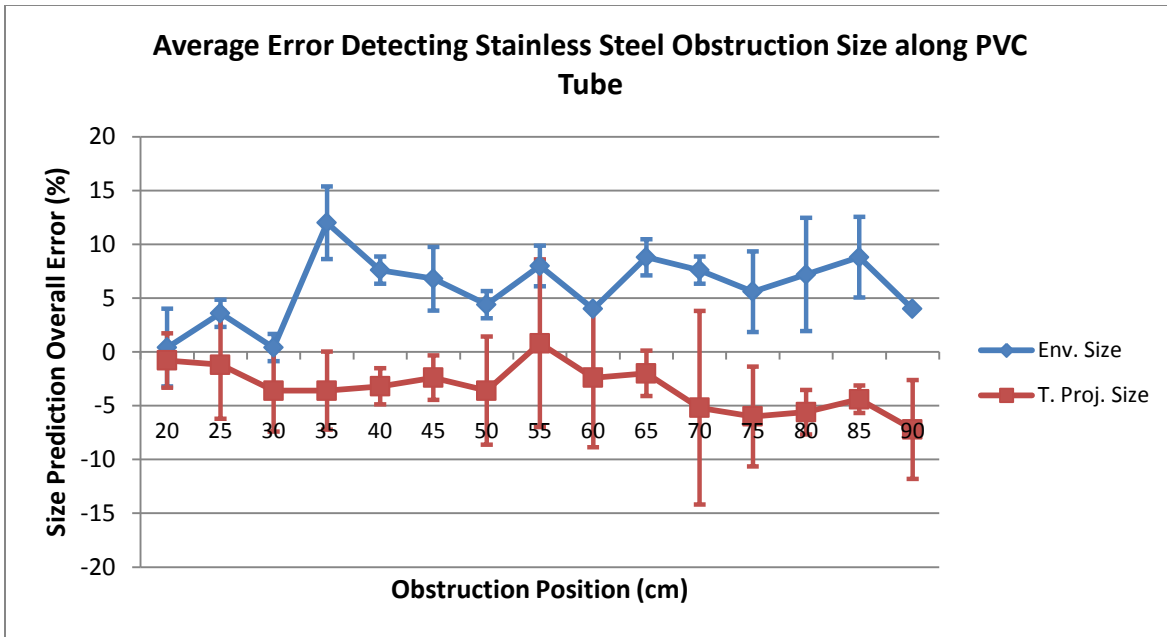


Figure 4-37 Average errors detecting S.S. obstructions size in water-filled PVC tube, using the envelope detection and time-axis projection. The envelope detection average errors show that this method overestimates the obstruction size real value with an overall error of 5.94 ± 2.17 % (mean \pm STD). The time-axis projections method underestimates the obstruction size real value with an overall error of -3.36 ± 4.10 % (mean \pm STD).

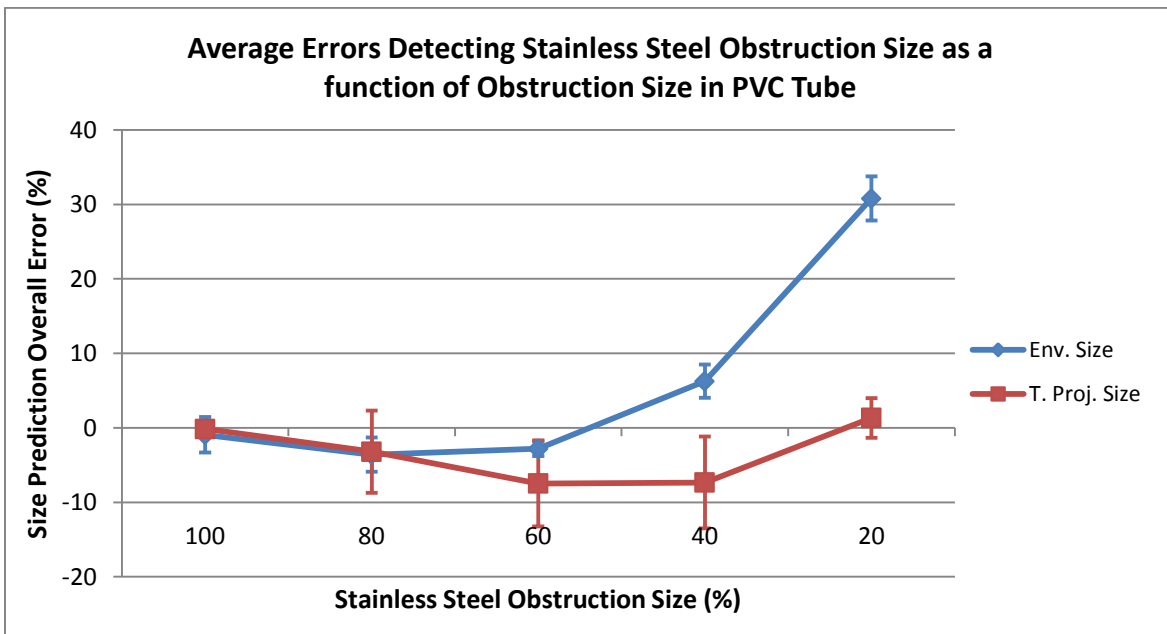


Figure 4-38 Average errors detecting S.S. obstructions size as function of obstruction size in water-filled PVC tube. For 40% and 20% S.S. obstructions, the envelope detection average error increases up to 30.8 ± 2.96 % (mean \pm STD). The time-axis projection average errors are lower, up to -7.46 ± 5.77 % (mean \pm STD) for 60% S.S. obstruction.

4.1.3.2.2 Signal Matching Algorithm Accuracy and Average Errors Detecting Delrin Obstructions

This section summarizes the results for Delrin obstructions location, size and type estimations in the water-filled PVC tube. As was performed for S.S. obstructions, ten measurements were recorded for each Delrin obstruction size and position along the PVC tube. Then the algorithm that compares the acoustic reflection envelope and time-axis projection was used to estimate the obstruction type, size and position of Delrin obstructions reflections. Figure 4-39 presents the accuracy of both features estimating the obstruction position (blue lines), size (green lines) and type (orange lines). As observed, the obstruction type was estimated correctly using both methods, with an accuracy of at least 98% for 60% Delrin obstruction. The estimation accuracy of Delrin obstructions position decreases as the obstruction size decreases, using both features. For the 20% Delrin obstruction, the accuracy using the signal envelope was 87.3%, slightly more than using the time-axis projection with 84.6% of accuracy.

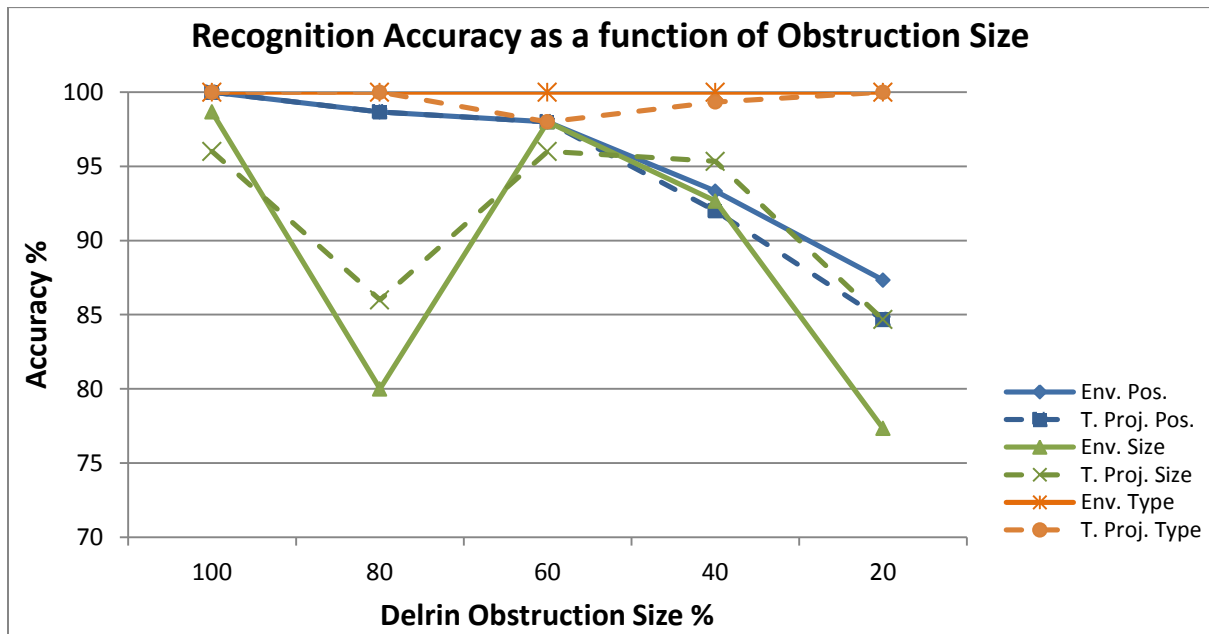


Figure 4-39 Algorithm accuracy using signal envelope and time-axis projection to detect Delrin obstruction size, position and type in PVC tube. The obstruction type (orange line) was estimated correctly using both methods. The obstruction position estimation accuracy (blue lines) decreases as the obstruction size decreases. For the obstruction size, it was estimated with an accuracy of at least 84.6% for 20% Delrin obstruction using the time-axis projection.

For the obstruction size estimation, the 80% and 20% obstructions results with the lowest accuracy percentages of 80% and 77.3% respectively, using the envelope feature. The time-axis projection has better accuracy estimating Delrin obstruction size, with 86% of accuracy for 80% Delrin obstruction and 84.6% for 20% Delrin obstruction.

Figure 4-40 shows the average errors estimating the Delrin obstructions location in the PVC tube. Using both features, the error is very similar along the different positions in the PVC tube. For distances of 70cm and closer, both algorithms underestimate the obstruction position up to -0.8 ± 1.68 cm (mean \pm STD) at 40cm. And for distances over 70cm, both algorithms overestimates the obstructions position up to 1.8 ± 2.08 cm (mean \pm STD) at 80cm. Figure 4-41 presents the distance estimation error as a function of obstruction size, where it is observed that that average error varies from -0.26 ± 0.56 cm (mean \pm STD) for 80% and 60% obstructions to 0.53 ± 1.12 cm (mean \pm STD) for 20% obstruction.

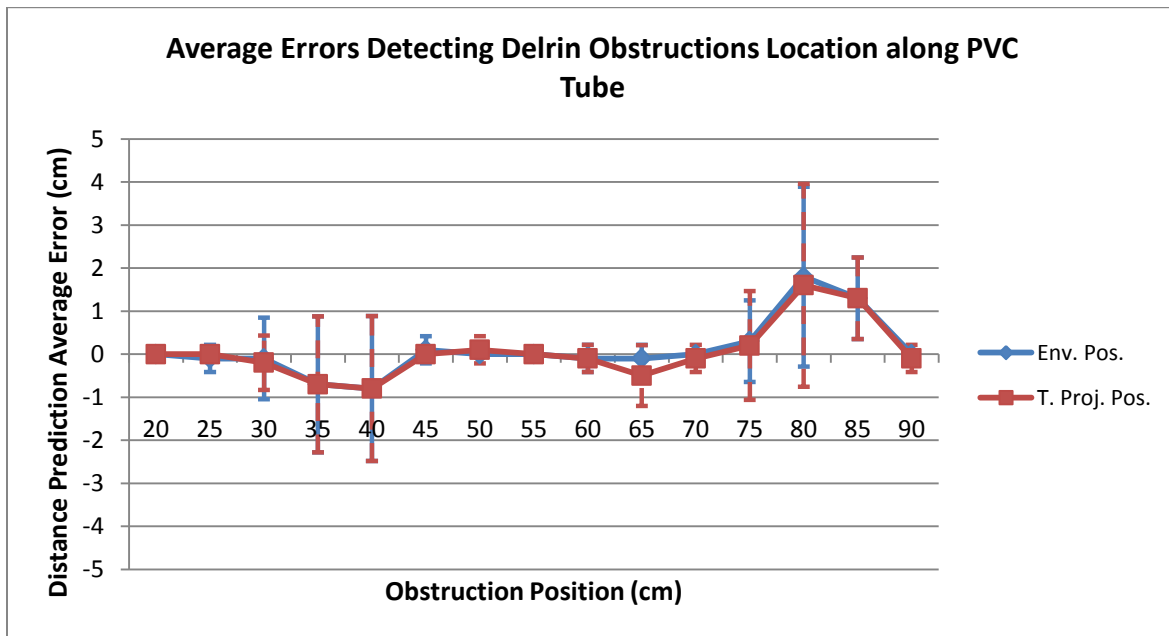


Figure 4-40 Average errors detecting Delrin obstructions position in water-filled PVC tube, using the envelope detection and time-axis projection. For distances of 70cm and closer, both algorithms underestimate the obstruction position up to -0.8 ± 1.68 cm (mean \pm STD) at 40cm. And for distances over 70cm, both algorithms overestimates the obstructions position up to 1.8 ± 2.08 cm (mean \pm STD) at 80cm using the envelope feature.

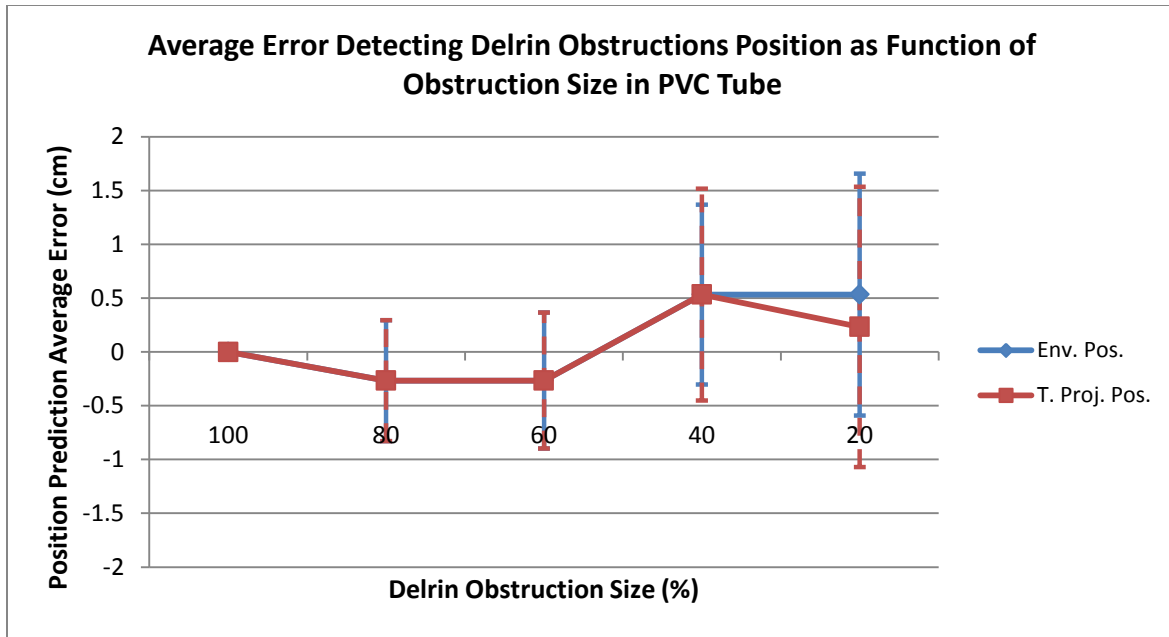


Figure 4-41 Average errors detecting Delrin obstructions position as function of obstruction size in water-filled PVC tube. Both features results in similar error values detecting the Delrin obstructions positions along the PVC tube. The error increases up to 0.53 ± 1.12 cm (mean \pm STD) as the obstruction size decreases at 20% size using the envelope feature.

Figure 4-42 illustrates the size estimation error as a function of obstruction location, where it is observed that average errors using the envelope feature varies from -5.60 ± 3.37 % (mean \pm STD) at 35cm to 4.8 ± 1.68 % (mean \pm STD) at 70cm. While using the time-axis projection the error variations is lower, from -4 ± 3.37 % (mean \pm STD) at 20cm to 2.4 ± 2.06 % (mean \pm STD) at 65cm. For positions of 45cm and closer both methods underestimates the obstruction size up to -5%, and for 50cm to 90cm the obstruction size is overestimated up to 5%. As expected from Figure 4-42, Figure 4-43 also shows that using time-axis projection results in lower error estimating Delrin obstructions size. For estimating 20% Delrin obstruction size the error increases up to 5.46 ± 6.52 % (mean \pm STD) using the envelope feature. The increment in error for 20% Delrin obstructions is mainly due to the low reflection intensity produced by the obstruction. As Figure 4-16 and 4-17 shows, the shape and intensity of the time-axis projection for the 20% Delrin obstruction is more notable than the signal envelope, resulting in a better comparison using the time-axis projection feature than the envelope feature.

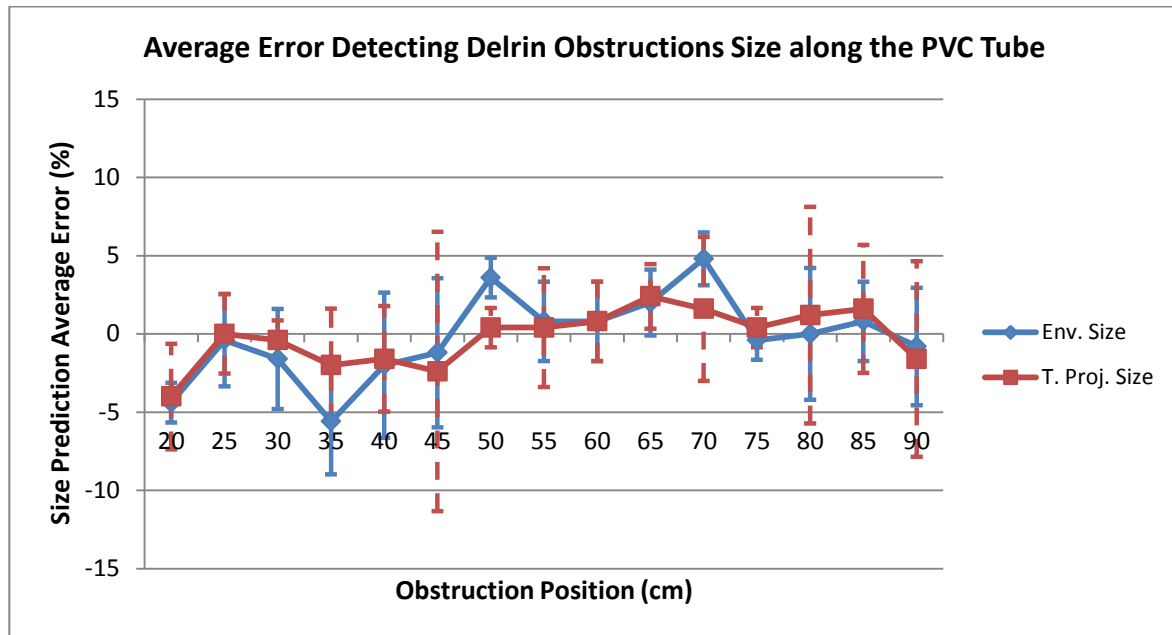


Figure 4-42 Average errors detecting Delrin obstructions size in water-filled PVC tube, using the envelope detection and time-axis projection. For positions of 45cm and closer both methods underestimates the obstruction size up to -5%, and for 50cm to 90cm the obstruction size is overestimated up to 5%.

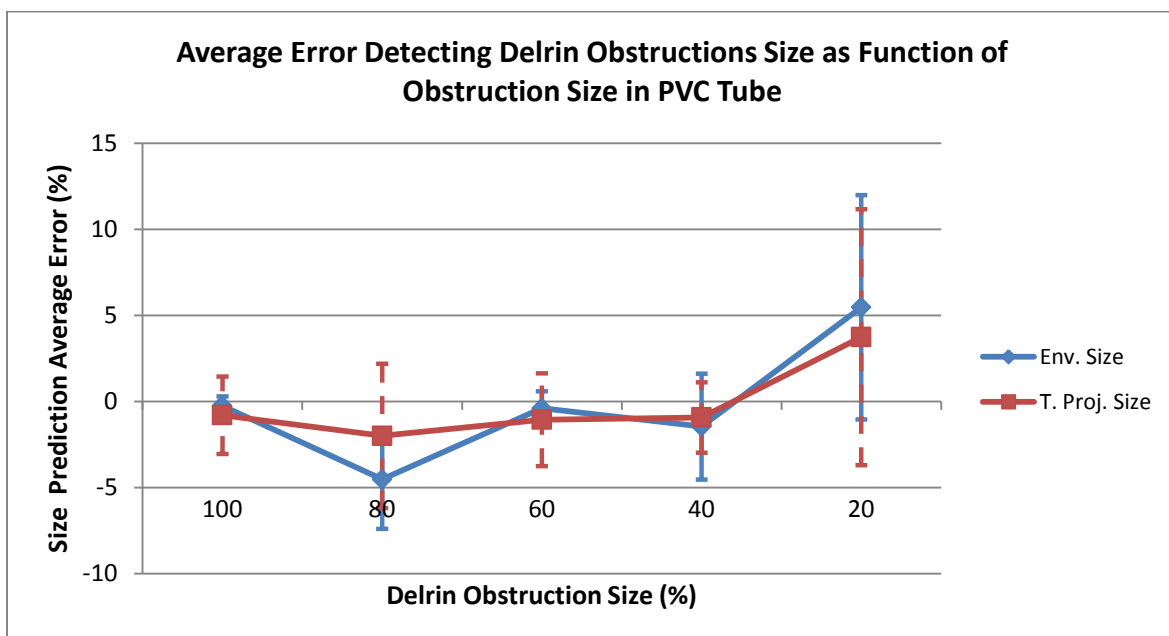


Figure 4-43 Average errors detecting Delrin obstructions size as function of obstruction size in water-filled PVC tube. The time-axis projection results with less error in detecting the Delrin obstruction size in the PVC tube. Using both methods the error increases for 20% obstruction size, up to 5.46 ± 6.52 % (mean \pm STD) using the envelope feature.

4.2 Copper Tube Measurements

For the Copper tube experiments, a tube with the same dimensions of the PVC tube of 1 meter long tube with 2.54 cm (1 inch) diameter was used. The reflection measurements were recorded utilizing the experimental setup presented in Figure 3-1. From propagation experiments we can state that acoustic modulated pulses with frequency of 100 kHz will not propagate along the water-filled Copper tube. Using modulated acoustic pulses of 200 and 300 kHz the propagation in water-filled Copper tubes was achieved. Figure 4-44 presents the reflection produced by a 100% S.S. obstruction located at 25cm, 55cm and 85cm in the tube using an acoustic pulse of 200 kHz with 20 μ s of duration. As mentioned previously in the discussion for the PVC tube reflections, the farther the obstruction is located from the hydrophone, the later the reflection wave occurs. The main difference from the PVC measurements performed is that reflections in Copper pipes have more dispersion, as observed in Figure 4-44.

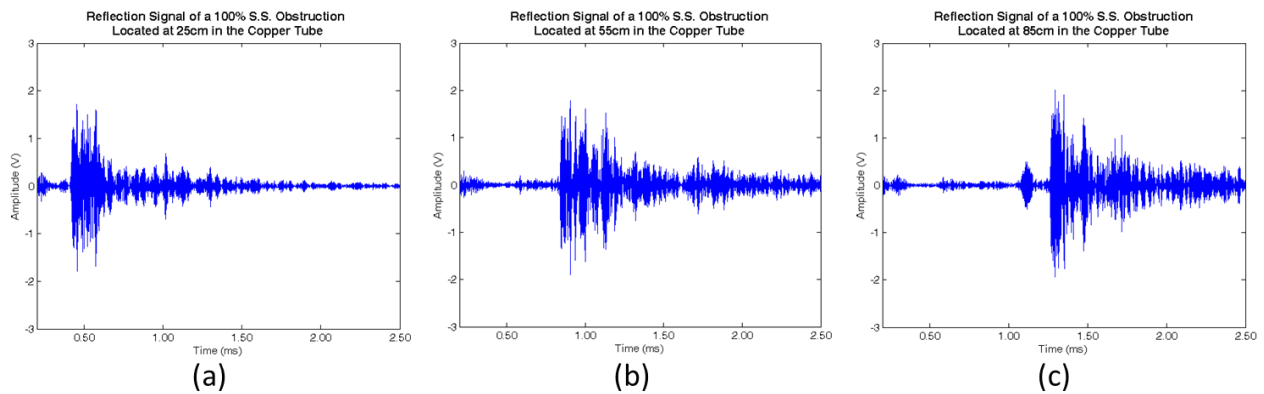


Figure 4-44 Reflection produced by an 100% S.S. obstruction in a water-filled copper tube, located at 25 cm (a), 55 cm (b) and 85 cm (c) from the hydrophone, using an acoustic pulse of 200 kHz with 20 μ s of duration.

The propagation velocity was calculated and plotted in Figure 4-45 using the reflection measurements of a 100% S.S. obstruction located from 5cm to 85cm. For water-filled copper tubes the average velocity was 1462 m/s and for water-filled PVC tube was 1428m/s, both fairly close to the sound propagation velocity in fresh water which is 1497 m/s.

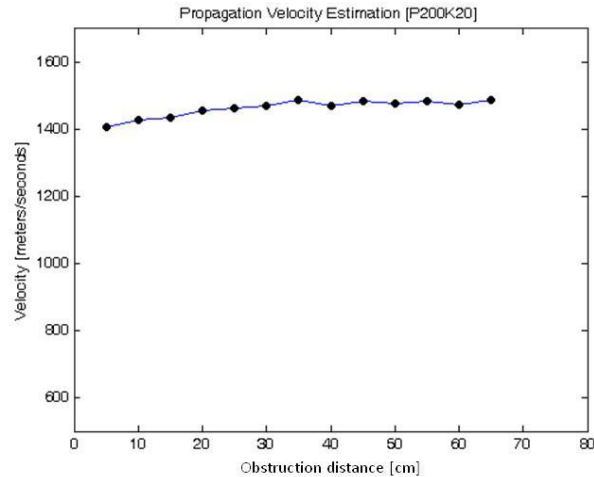


Figure 4-45 Calculated velocities using the onset detection algorithm and Equation 4.1. Each velocity belongs to a reflection produced by an obstruction located in the water-filled copper tube.

4.2.1 Signal Matching Results

As presented in Section 4.1 for the PVC tubes, the same procedures used to extract the reflections signal envelope and time-axis projection were implemented, to estimate the stainless steel and Delrin obstructions type, size and location in the copper tube. A database was created for each obstruction type. Each database contains the reflections envelope and time-axis projections for the 5 different obstruction sizes (100%, 80%, 60 %, 40% and 20%) located along the copper tube. Finally, the signal matching algorithm, presented in Figure 3-9, compares the features extracted from an obstruction reflection with the feature databases to estimate the obstruction type, size and position in the copper tube.

4.2.1.1 Signal Matching Algorithm Accuracy and Average Errors Detecting Stainless Steel Obstructions

As was performed with the water-filled PVC tube, ten measurements were recorded for each S.S. obstruction size located at different positions along the water-filled copper tube. Figure 4-46 presents the signal matching algorithm accuracy estimating the S.S. obstruction type, size and position using the signal envelope and time-axis projection. It is observed that the signal envelope results with higher accuracy, estimating the obstruction type (solid orange line) rather than using the time-axis projection. The time-axis projection accuracy drops to 85.3% for 20% S.S. obstruction, while the signal envelope has an accuracy of 98.6% for 20% S.S. obstruction. Compared to Figure 4-34, the S.S. obstruction type estimation accuracy for 20% S.S. obstruction in the water-filled copper tube was 85.3%, while in the PVC tube was 35.3%. For the obstruction size and position estimation, the signal envelope (solid lines) results better accuracy than using the time-axis projection. The acoustic reflections in the water-filled copper tube, as shown in Figure 4-44, have more dispersion and less attenuation than in the PVC tube. This results in signal envelopes and time-axis projections with higher amplitudes for small obstructions, making a better database comparison and obstructions estimation.

Figure 4-47 and 4-48 illustrates the average errors estimating the S.S. obstruction distance as a function of obstruction position and size, respectively. From Figure 4-47 it can be stated that as obstruction distance increases the error also increases, with a maximum error of -2.6 ± 5.97 cm (mean \pm STD) at 90cm using both methods. This tendency was also observed for S.S. obstructions in the PVC tube. Figure 4-48 shows that for 100% and 80% S.S. obstructions, the position was underestimated with an error of -1 ± 1.35 cm (mean \pm STD) for 80% S.S. obstruction. For 40% and 20% the position was overestimated with an error of 1.06 ± 1.71 cm (mean \pm STD) for 20% S.S. obstruction. The difference between the signal envelope and time-axis projection to estimate the S.S. obstruction position was indistinct.

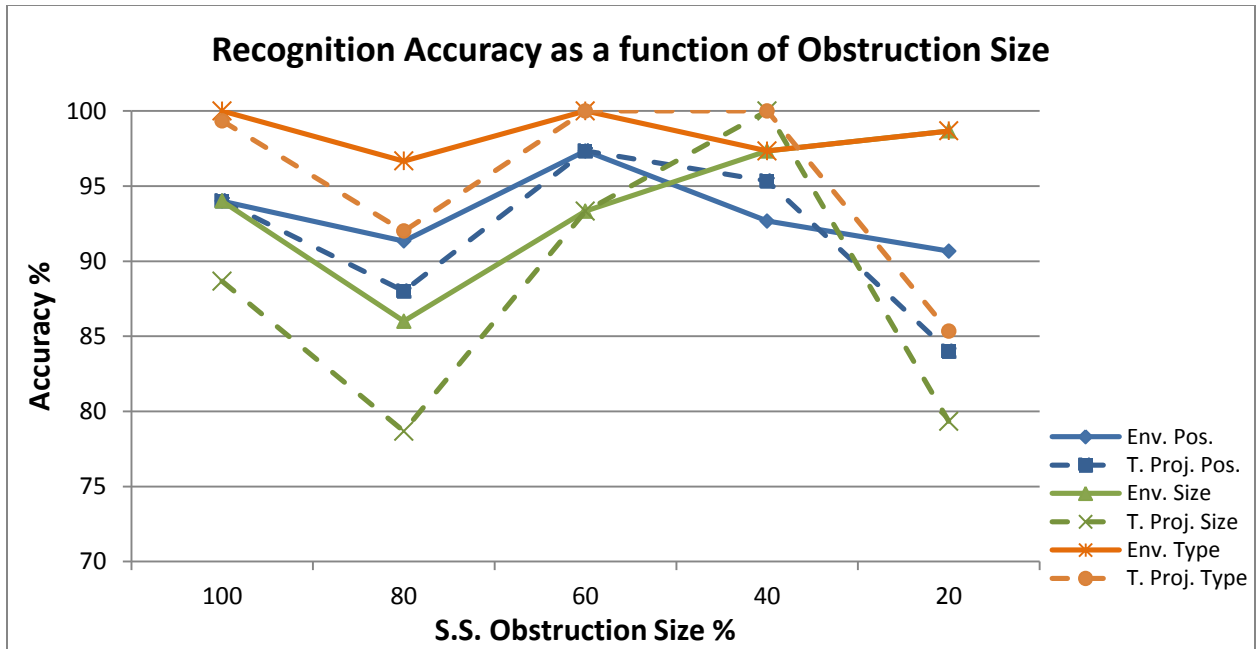


Figure 4-46 Algorithm accuracy using signal envelope and time-axis projection to detect S.S. obstruction size, position and type in copper tube. The obstruction type (orange line) was estimated with more accuracy using the signal envelope feature, while the time-axis projection decreases to 85.3% of accuracy for 20% obstruction. The envelope feature results with higher accuracy than time-axis projection, detecting the obstruction type, size and locations as function of S.S. obstruction size.

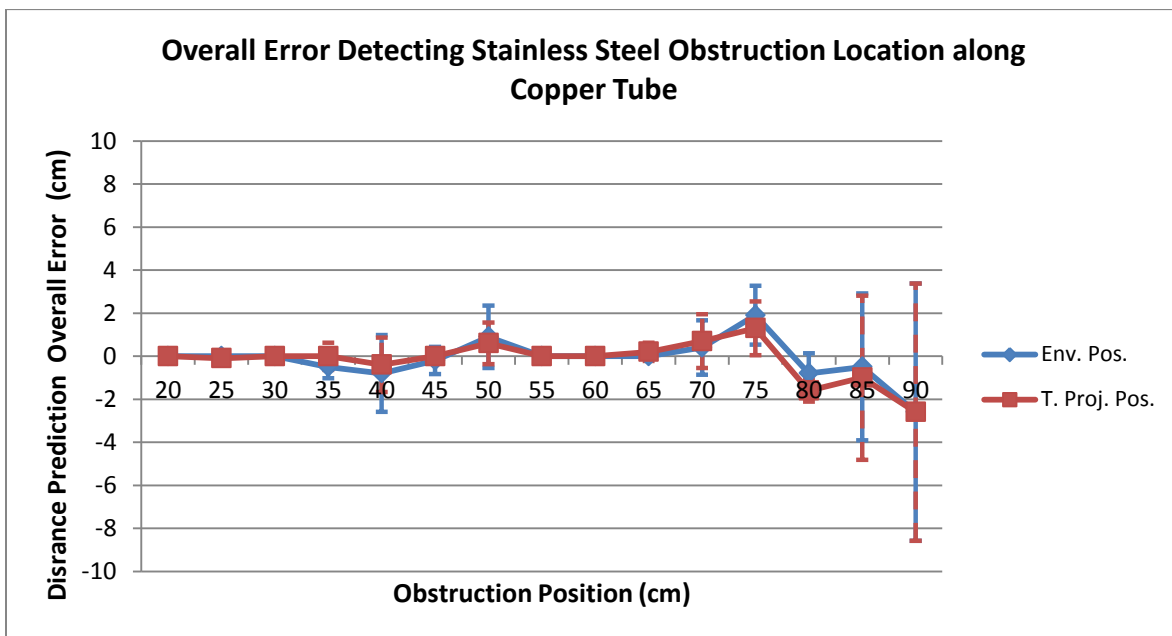


Figure 4-47 Average errors detecting S.S. obstruction position in water-filled copper tube, using the envelope detection and time-axis projection. As the obstruction position increases the average location error also increases, with a maximum error of -2.6 ± 5.97 cm (mean \pm STD) at 90cm. Both methods show very similar error results.

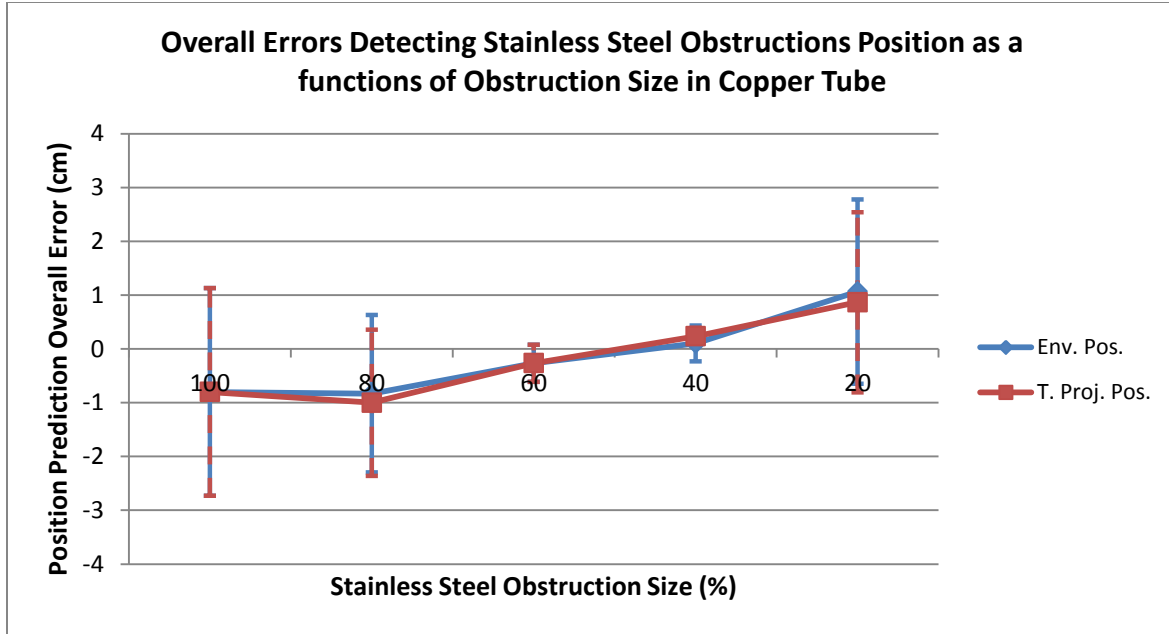


Figure 4-48 Average errors detecting S.S. obstructions position as function of obstruction size in water-filled copper tube. Both methods show very similar error results, where the average error varies from -0.80 ± 1.92 cm (mean \pm STD) for 100% S.S. obstruction to 1.06 ± 1.71 cm (mean \pm STD) for 20% S.S. obstruction.

The average error estimating the S.S. obstruction size as a function of obstruction distance is presented in Figure 4-49. It is notable that the signal envelope results with less error estimating the S.S. obstruction size, than using the time-axis projection. For obstruction positions of 25cm and 80cm, the size prediction error using the time-axis projection was $10.4 \pm 5.05\%$ (mean \pm STD) and $-12 \pm 0.0\%$ (mean \pm STD) respectively. While using the signal envelope, the error increases as the obstruction position increases up to $-8.8 \pm 9.9\%$ (mean \pm STD) at 90cm. Figure 4-50 presents the S.S. obstruction size error as a function of obstruction size, where it is observed that the signal envelope, as expected, results with lower errors than the time-axis projection. From Figure 4-49 and 4-50, it can be stated that the signal envelope outperformed the time-axis projection estimating the S.S. obstruction size in the copper tube.

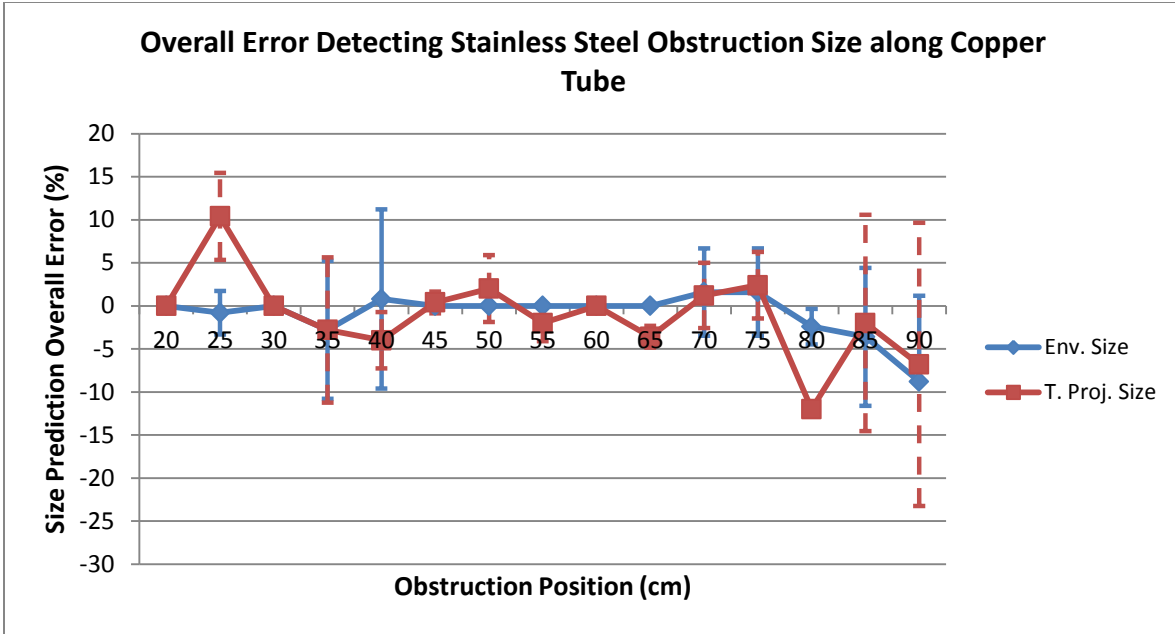


Figure 4-49 Average errors detecting S.S. obstruction size in water-filled copper tube, using the envelope detection and time-axis projection. Time-axis projection results on higher errors detecting the obstruction size in the copper tube than using the signal envelope.

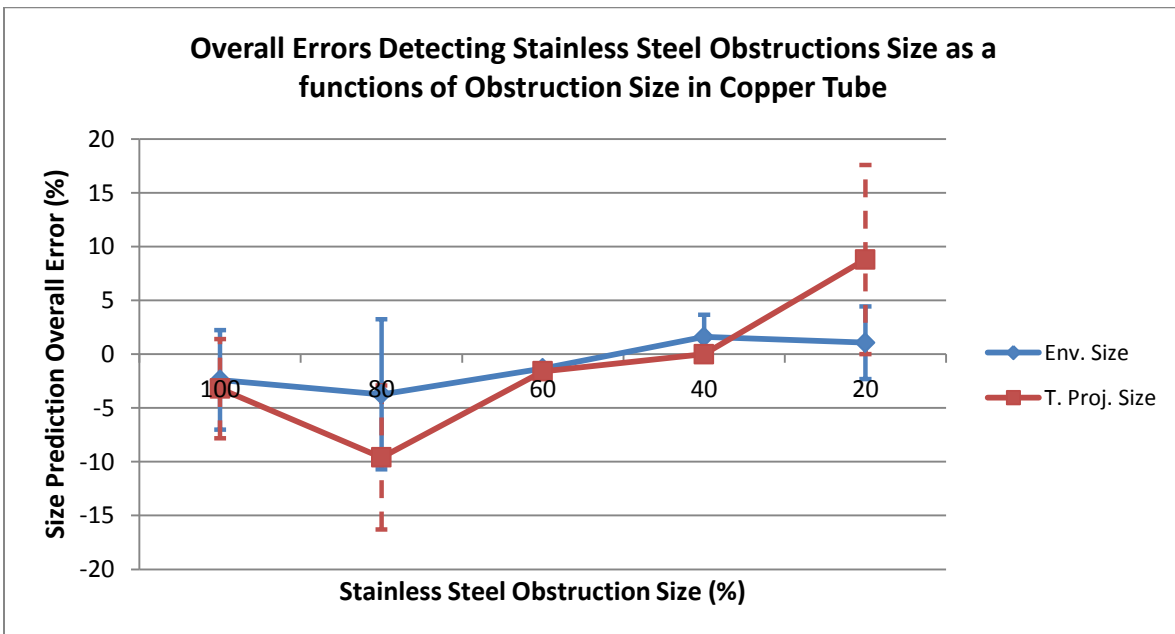


Figure 4-50 Average errors detecting S.S. obstructions size as function of obstruction size in water-filled copper tube. The signal envelope results on lower errors detecting the obstruction size than using time-axis projection.

4.2.1.2 Signal Matching Algorithm Accuracy and Average Errors Detecting Delrin Obstructions

As mentioned in the previous sections, ten measurements were recorded for each obstruction type and size, located along the water-filled copper tube. Each measurement was processed using the signal matching algorithm to estimate the obstruction type, size and position. Figure 4-51 presents the algorithm accuracy estimating the Delrin obstructions type, size and position, using the signal envelope and time-axis projection features. It is observed that using the signal envelope to estimate the Delrin obstruction type (solid orange line) in the copper tube, results with 100% accuracy for all obstruction sizes. In the other hand, estimating Delrin obstruction type using time-axis projection (dashed orange line), results with a decrease in accuracy for small Delrin obstructions. The signal envelope also shows higher accuracies estimating Delrin obstructions size and position along the water-filled copper tube. But as a common factor, the accuracy decreases as the Delrin obstruction size decreases using both methods.

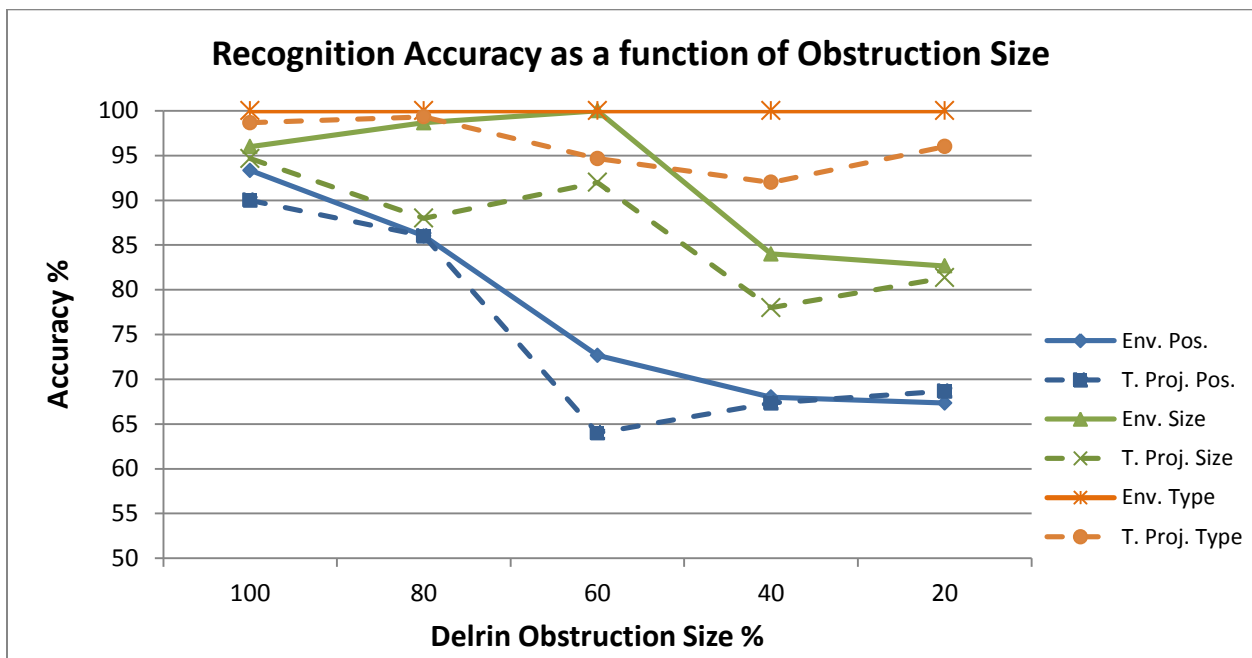


Figure 4-51 Algorithm accuracy using signal envelope and time-axis projection to detect Delrin obstruction size, position and type in copper tube. The obstruction type (orange line) was estimated with an accuracy of 100% using the signal envelope feature, while the time-axis projection accuracy decreases for small Delrin obstructions. For the obstruction size and position estimation, the accuracy decrease as the obstruction size decreases. Signal envelope (solid lines) results with higher accuracy than time-axis projection, detecting Delrin obstructions type, size and position.

Figure 4-52 and 4-53 presents the average errors estimating the Delrin obstructions position along the water-filled copper tube. As Figure 4-52 shows, the average error begins to increase for obstruction located at larger distances. Both methods show similar error results, where the maximum error was of -9.8 ± 12.41 cm (mean \pm STD) at 90 cm in the copper tube. Also Figure 4-53 also shows that both methods have very similar error results, where the average error increases to 3.76 ± 2.69 cm (mean \pm STD) for 60% and 1.73 ± 7.11 cm (mean \pm STD) for 20% Delrin obstructions. Signal envelope and time-axis projections have similar average errors estimating Delrin obstructions position, as Figure 4-52 and 4-53 illustrates. However, Figure 4-51 shows that signal envelope estimates slightly better Delrin obstructions position in the water-filled copper tube.

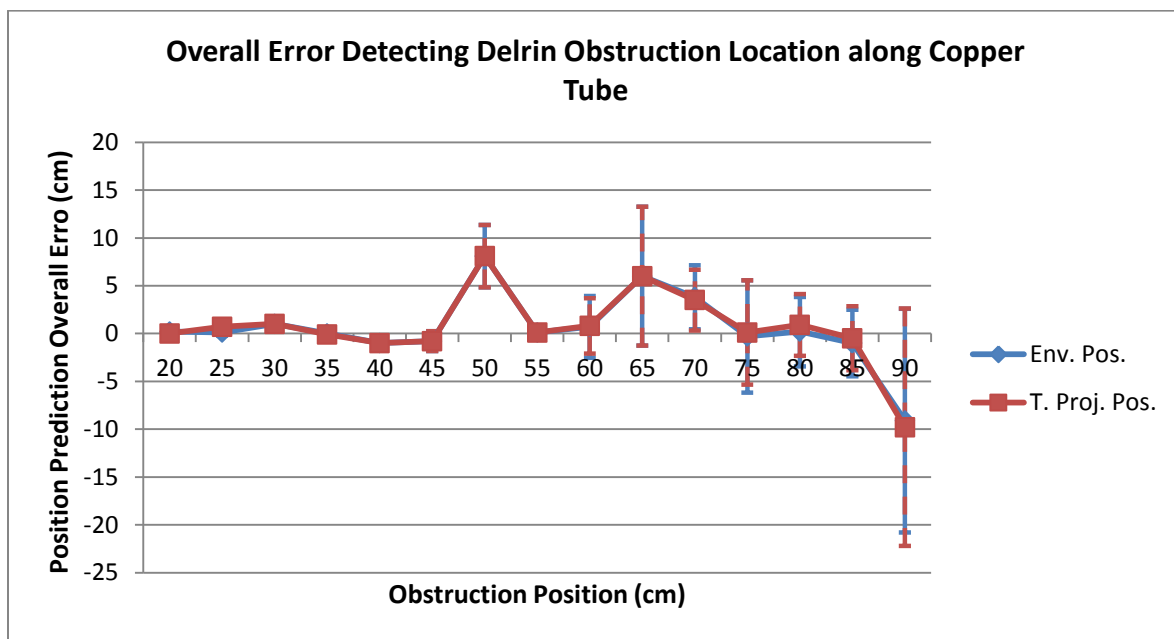


Figure 4-52 Average errors detecting Delrin obstruction position in water-filled copper tube, using the envelope detection and time-axis projection. As the obstruction position increases the average location error also increases, with a maximum error of -9.8 ± 12.41 cm (mean \pm STD) at 90cm. Both methods show very similar error results.

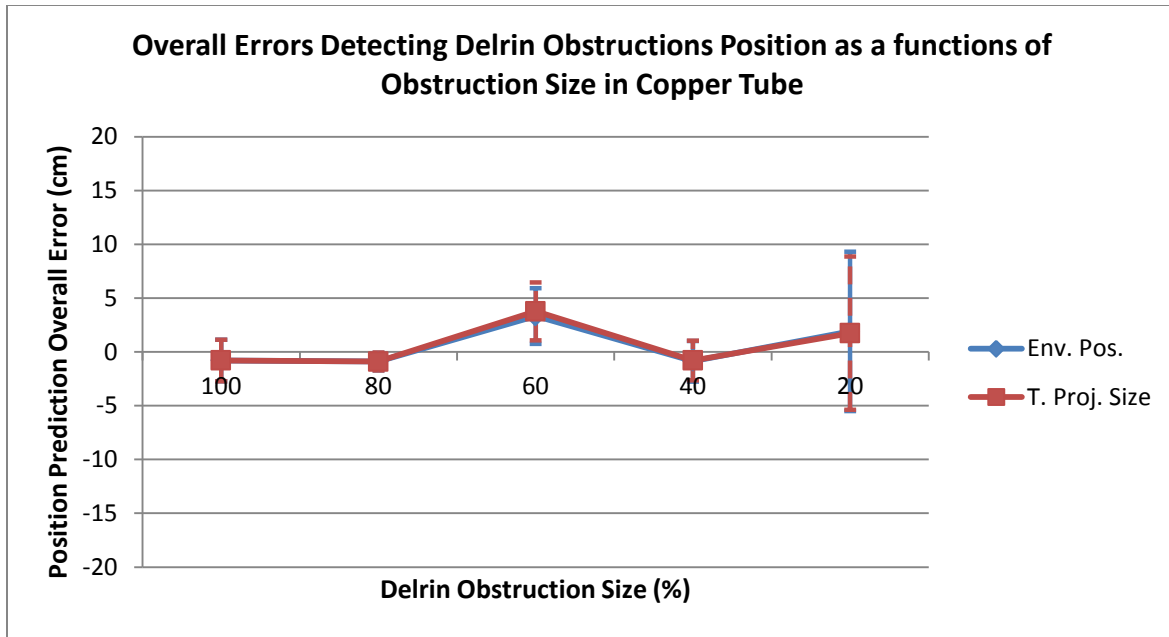


Figure 4-53 Average errors detecting Delrin obstructions position as function of obstruction size in water-filled copper tube. Both methods show very similar error results, where the average error increases to 3.76 ± 2.69 cm (mean \pm STD) for 60% and 1.73 ± 7.11 cm (mean \pm STD) for 20% Delrin obstructions.

The average errors estimating Delrin obstructions size as a function of obstruction distance, is presented in Figure 4-54. The time-axis projection shows slightly large errors than using the signal envelope at particular positions in the copper tube. The largest error by both methods results at 50cm, with $8.8 \pm 4.54\%$ (mean \pm STD) for the signal envelope and $14.4 \pm 5.05\%$ (mean \pm STD) for the time-axis projection. Using both methods, the error tends to increase as the obstruction position increases.

Figure 4-55 shows the average errors estimating the Delrin obstruction size as a function of obstruction size. Where the largest error was obtained for 20% Delrin obstruction, which was $8 \pm 7.88\%$ (mean \pm STD) for the signal envelope and $12.4 \pm 13.15\%$ (mean \pm STD) for the time-axis projection. Both methods results on similar error values for the larger Delrin obstructions. Thus the signal envelope results with lower averages errors, estimating the Delrin obstruction sizes in the water-filled copper tube.

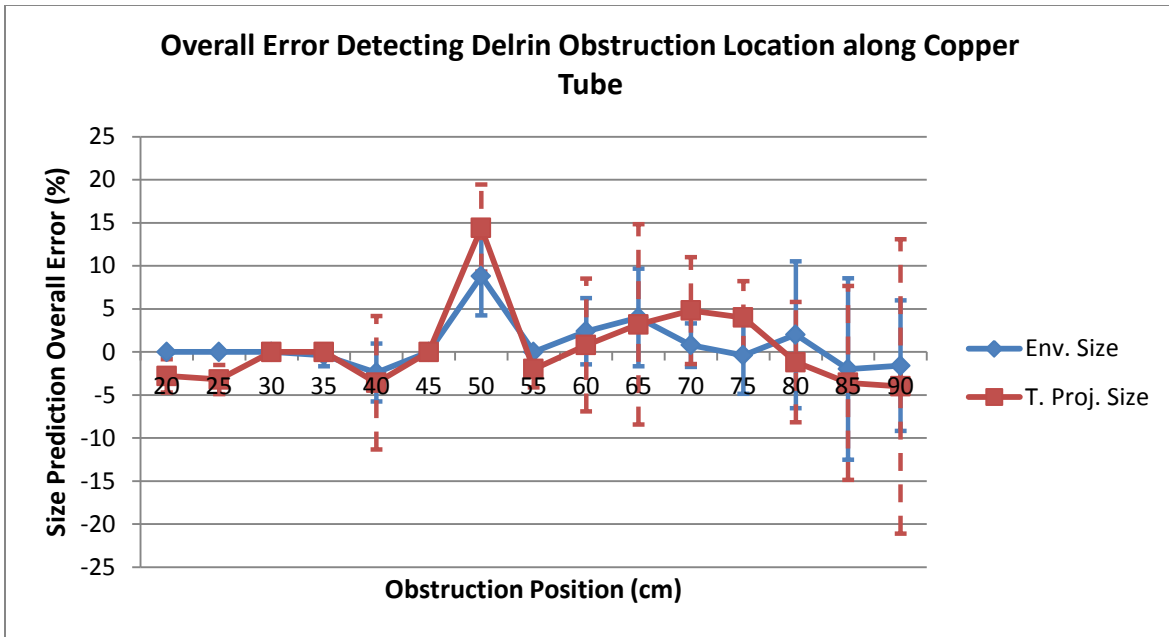


Figure 4-54 Average errors detecting Delrin obstruction size in water-filled copper tube, using the envelope detection and time-axis projection. As the obstruction distance increase the estimation error star to increase using both methods.

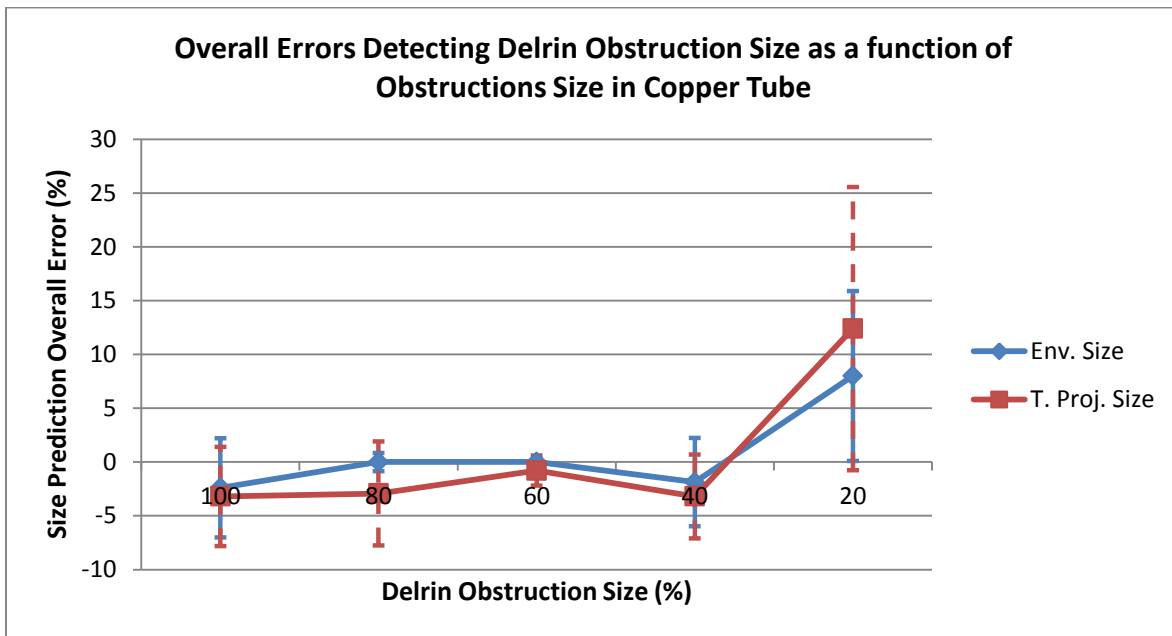


Figure 4-55 Average errors detecting Delrin obstructions size as function of obstruction size in water-filled copper tube. The signal envelope results on slightly lower errors detecting the obstruction size than using time-axis projection.

4.3 Vinyl Tube Measurements

Catheters construction is based in polymers such as silicone rubber, latex and polyurethane elastomers. The special configuration shown in Figure 3-19 and 4-56, which consists on a flexible vinyl tube of 1 cm of diameter inside a larger vinyl tube, mimics a catheter inside a patient. This special vinyl tube configuration, shown in Figure 4-56, was placed in the setup presented in Figure 3-1 to record and analyze reflections produced by obstructions. To accomplish acoustic propagation in the water-filled vinyl tube of 1cm of diameter, the modulated pulse frequency was increased to 300 kHz with duration of 20 μ sec. Figure 4-57 illustrates the vinyl tubes configuration surrounded by water, with a 100% Delrin obstruction located at 12cm from the hydrophone. The air layer kept the acoustic waves propagation inside the 1cm diameter vinyl tube, which makes possible acoustic reflections being produced and recorded.

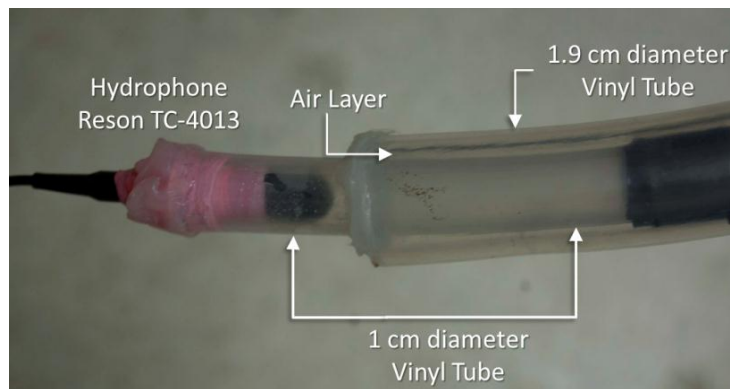


Figure 4-56 Experimental setup of the flexible Vinyl tubes configuration used for measurements.

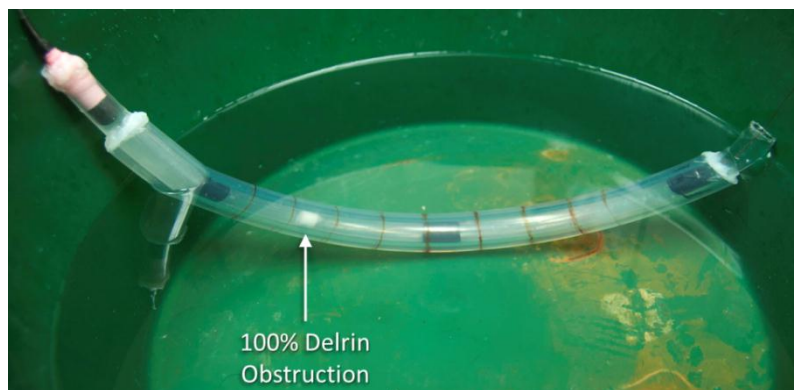


Figure 4-57 Water-filled vinyl tube configuration surrounded by water with a layer of air in between. A 100 % Delrin obstruction located at 12cm from the hydrophone in the vinyl tube.

After achieving acoustic propagation in the water-filled vinyl tube with a 300 kHz pulse, the acoustic propagation velocity was calculated experimentally as was for the PVC and copper tube. Figure 4-58 shows the reflections measured by a 100% S.S. obstruction located at 9 cm, 12 cm and 15 cm from the hydrophone. As the obstruction is located farther from the hydrophone, their reflection occurs later, same as the PVC and copper tube reflections. Using these reflections the propagation velocity was estimated using the onset detection and Equation 4.1. Figure 4-59 shows the velocities calculated using the reflections recorded at different location in the vinyl tube. The average propagation velocity in the vinyl tube was 1312.7 m/s, lower than the propagation velocity in PVC and copper which were 1428 m/s and 1462 m/s respectively. As the tubes material becomes more flexible, the phase velocity traveling to the water decrease due to the material relaxation time and propagation speed as shown in Equation 2.18.

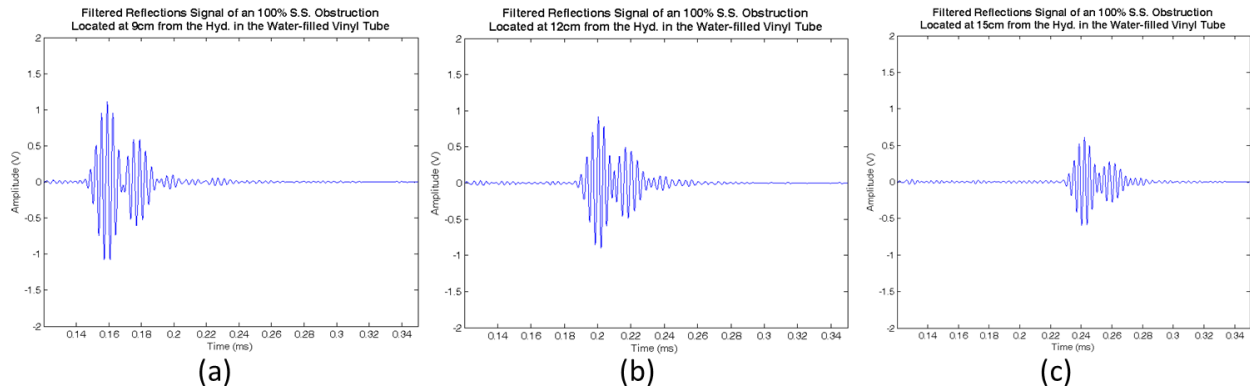


Figure 4-58 Reflection due to a 100% S.S. obstruction located at 9cm (a), 12cm (b) and 15cm (c) from the Hyd. in a 1cm diameter vinyl tube and using an acoustic pulse with frequency of 300 kHz and 20 μ s.

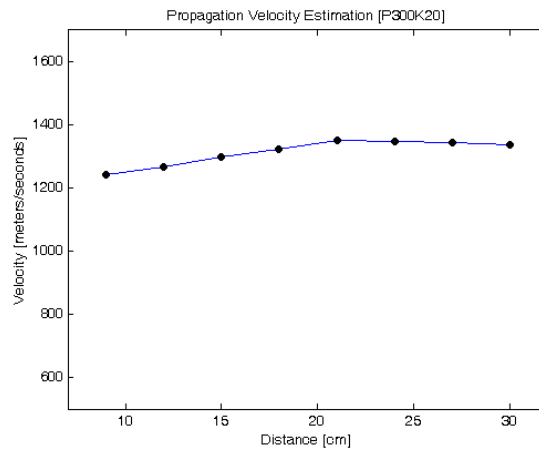


Figure 4-59 Calculated velocities using the onset detection algorithm and Equation 4.1. Each velocity belongs to a reflection produced by an obstruction located in the water-filled vinyl tube. The average propagation velocity found experimentally in the vinyl tube was 1312.7 m/s.

4.3.1 Signal Matching Results

As presented in Section 4.1 for the PVC tube and Section 4.2 for the copper tube, the same procedures used to extract the reflections signal envelope and time-axis projection were implemented, to estimate the stainless steel and Delrin obstructions type, size and location in the vinyl tube. A database was created for each obstruction type. Each database contains the reflections envelope and time-axis projections for the 5 different obstruction sizes (100%, 80%, 60 %, 40% and 20%) located along the vinyl tube. Since the vinyl tube has a diameter of 1cm, the same obstructions used for the PVC and copper tube cannot be used. Figure 3-20 illustrates the smaller obstruction used in the vinyl tube experiments. Another variation from the PVC and copper tube measurements was the obstruction location measurements that were recorded from 9cm to 30cm with increments of 3cm, since the vinyl tube was 40cm long. Finally, the signal matching algorithm, presented in Figure 3-9, compares the features extracted from an obstruction reflection with the feature databases to estimate the obstruction type, size and position in the vinyl tube.

4.3.1.1 Signal Matching Algorithm Accuracy and Average Errors Detecting Stainless Steel Obstructions

As was performed in the PVC and copper tube, ten measurements were recorded for each obstruction type, size and location in the water-filled vinyl tube. The signal matching algorithm extracts the envelope and time-axis projection of the reflection produced by an obstruction, to estimate its type, size and position along the vinyl tube. Figure 4-60 presents the accuracy estimating S.S. obstructions type, size and position along the vinyl tube using the signal envelope and time-axis projection features. The obstruction type (orange lines) was estimated with an accuracy of at least 97.5% using the signal envelope, slightly better than using the time-axis projection with an accuracy of 95%. For the obstruction size and position estimation, the signal envelope also results with better accuracies compared with the

time-axis projection. As the PVC and copper tube, the accuracy tends to decrease as the obstruction size decreases, more notable in the position estimation for the vinyl tube.

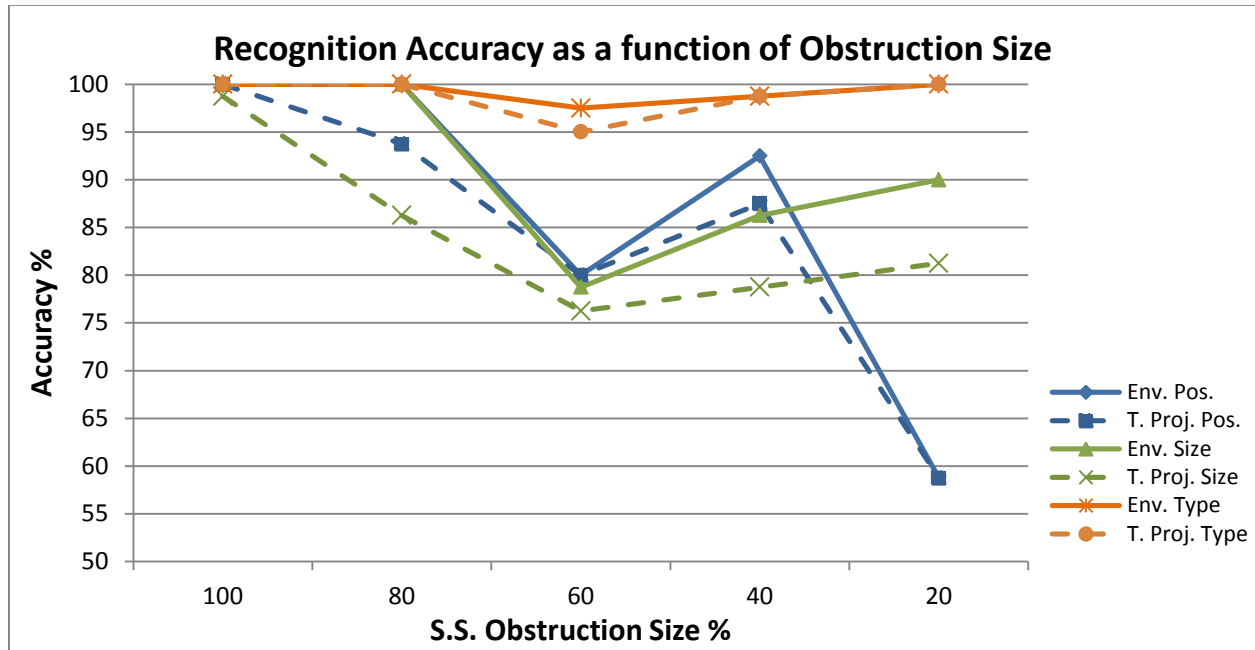


Figure 4-60 Algorithm accuracy using signal envelope and time-axis projection to estimate S.S. obstruction size, position and type in vinyl tube. The obstruction type (orange line) was estimated with accuracy over 95% using the signal envelope and time-axis projection feature. For the obstruction size and position estimation, the envelope results with higher accuracies than using the time-axis projection.

Figure 4-61 shows the average error estimating the S.S. obstruction position along the vinyl tube. As mentioned for the PVC and copper tubes, while the obstruction distance increases the error also increases. For the vinyl tube the largest error estimating the obstruction distances was -2.4 ± 2.57 cm (mean \pm STD) at 30cm, which is the farther distance measured. Figure 4-61 also shows that both methods are very similar estimating the S.S. obstructions position along the vinyl tube. In Figure 4-62 is presented the average errors as a function of obstruction size, where it is observed that the 60% and 20% S.S. obstructions results with the higher errors. The 60% obstruction was underestimated to -0.82 ± 1.43 cm (mean \pm STD) and the 20% was overestimated to 0.9 ± 1.88 cm (mean \pm STD).

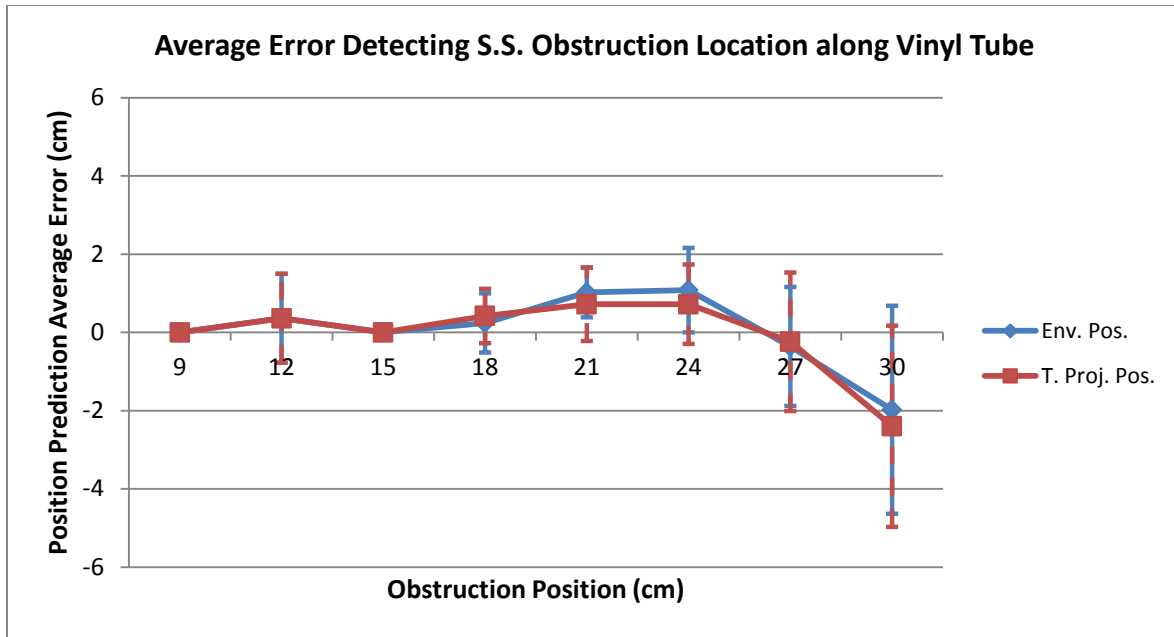


Figure 4-61 Average errors detecting S.S. obstruction position in water-filled vinyl tube, using the envelope detection and time-axis projection. As the obstruction position increases the average location error also increases, with a maximum error of -2.4 ± 2.57 cm (mean \pm STD) at 30cm. Both methods show very similar error results.

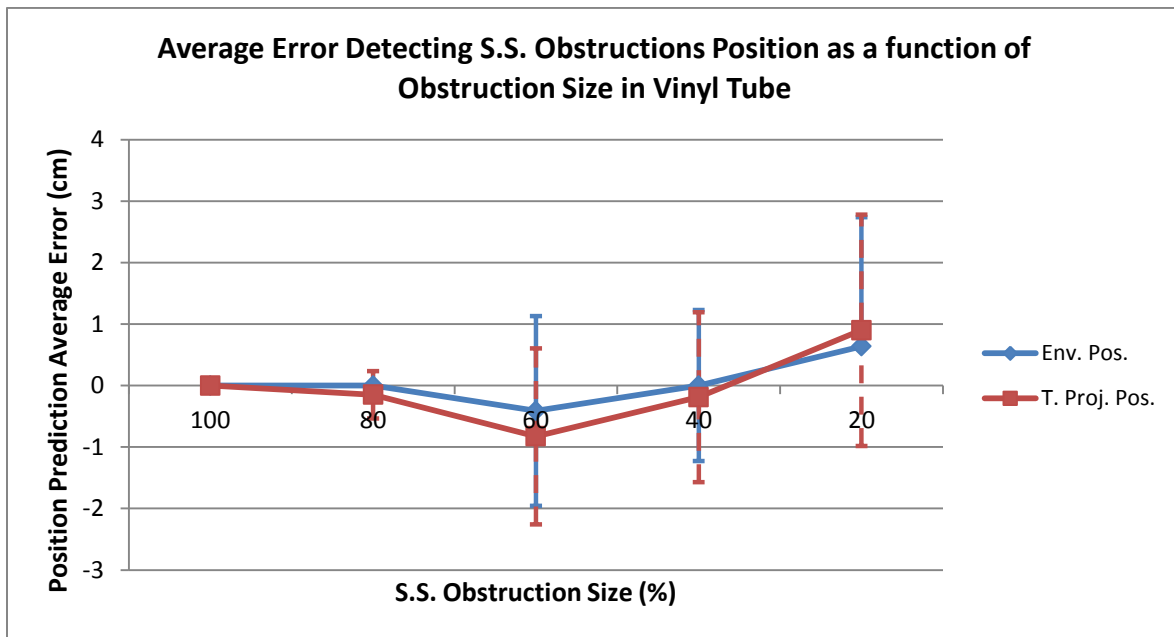


Figure 4-62 Average errors detecting S.S. obstructions position as function of obstruction size in water-filled vinyl tube. Both methods show very similar error results, where the average error varies from -0.82 ± 1.43 cm (mean \pm STD) for 60% S.S. obstruction to 0.9 ± 1.88 cm (mean \pm STD) for 20% S.S. obstruction.

Figure 4-63 and 4-64 presents average error estimating the obstruction size in the vinyl tube using the signal envelope and time-axis projection. As occur with the PVC and copper tube, as the obstruction position increases the error estimating the obstruction size also increases. The error increment is more notable using the time-axis projection with an error of $-5.2 \pm 18.84\%$ (mean \pm STD) at 30cm, compared to $-1.2 \pm 6.23\%$ (mean \pm STD) using the signal envelope. As Figure 4-64 shows, the error also increases for smaller obstructions, up to $7 \pm 11.24\%$ (mean \pm STD) for the 20% S.S. obstruction using the time-axis projection. The signal envelope also results on lower errors estimating the obstruction size, as expected from Figure 4-60, which shows higher accuracy using the envelope to estimate S.S. obstruction size.

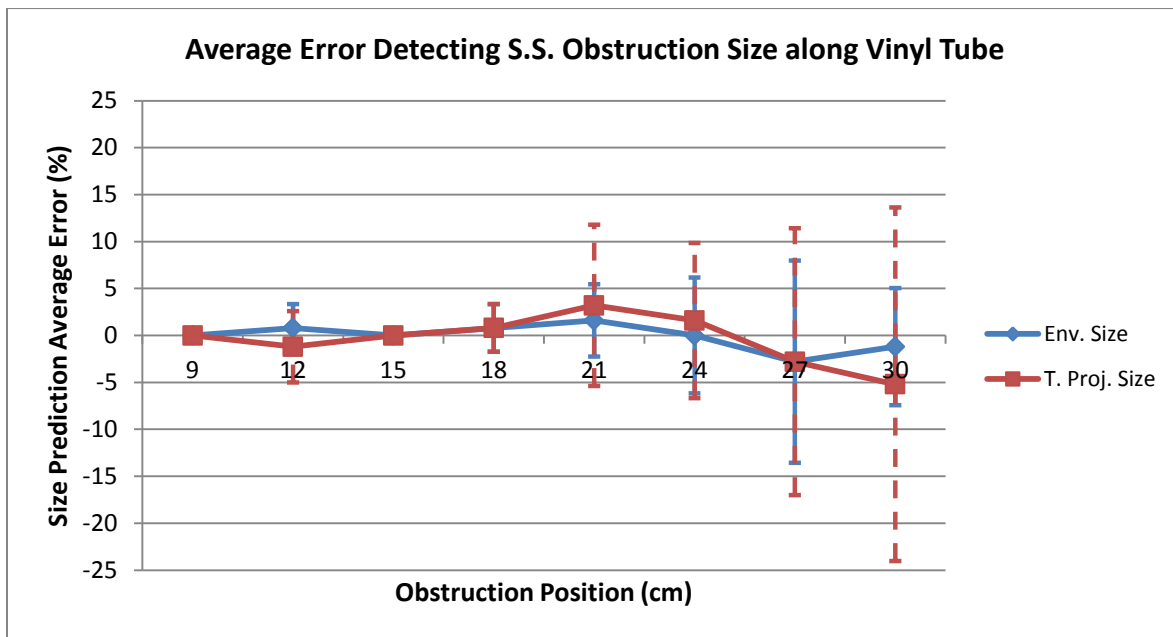


Figure 4-63 Average errors detecting S.S. obstruction size in water-filled vinyl tube, using the envelope detection and time-axis projection. As the obstruction position increases the average error and standard deviation estimating the obstruction size also increases, more notable using the time-axis projection. At 30cm the error using the time-axis projection was $-5.2 \pm 18.84\%$ (mean \pm STD) and with the signal envelope $-1.2 \pm 6.23\%$ (mean \pm STD).

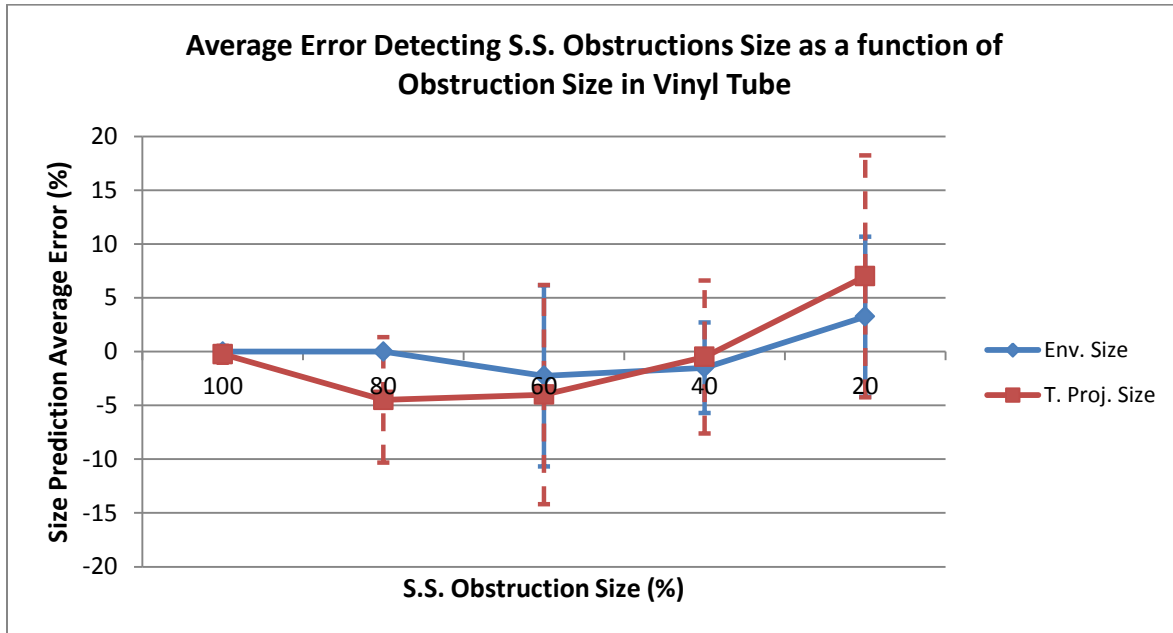


Figure 4-64 Average errors detecting S.S. obstructions size as function of obstruction size in water-filled vinyl tube. The signal envelope results on lower errors detecting the obstruction size than using time-axis projection. As the obstruction size decreases the error increases up to 7 ± 11.24 % (mean \pm STD) for the 20% S.S. obstruction using the time-axis projection

4.3.1.2 Signal Matching Algorithm Accuracy and Average Errors Detecting Delrin Obstructions

The same procedure was repeated using the signal matching algorithm to estimate Delrin obstructions type, size and position in water-filled vinyl tube. Figure 4-65 shows the accuracy of the signal envelope and time-axis projection to estimate Delrin obstructions type, size and position along the water-filled vinyl tube. The obstruction type was estimated with an accuracy of 100% using the signal envelope (solid orange line), while using the time-axis projection was estimated with an accuracy of at least 98.7%. For the obstruction size and position estimation, the signal envelope also results with higher accuracies compared to the time-axis projection. As presented in the PVC and copper tube, the accuracy estimating Delrin obstructions size and position tend to decrease for smaller obstruction.

Figure 4-66 presents the error estimating the Delrin obstructions position as the obstruction is located at different positions along the water-filled vinyl tube. As PVC and copper tubes, the error estimating the obstruction distance increases as the obstruction position also increases, with a maximum error of $-2.46 \pm 3.60\text{cm}$ (mean \pm STD) at 30cm using time-axis projection. Figure 4-66 also shows that the signal envelope has less error as the obstruction position increases compared to the time-axis projection.

The error estimating the obstruction position as function of obstruction size is presented in Figure 4-67. The estimated position of the 40% Delrin obstruction was overestimated more notable as the obstruction position increases, as Figure 4-66 shows, resulting in an average error of $1.46 \pm 2.34\text{cm}$ (mean \pm STD) using the time-axis projection. Once again the signal envelope results with less error estimating the Delrin obstruction position as a function of obstruction size, presented in Figure 4-67.

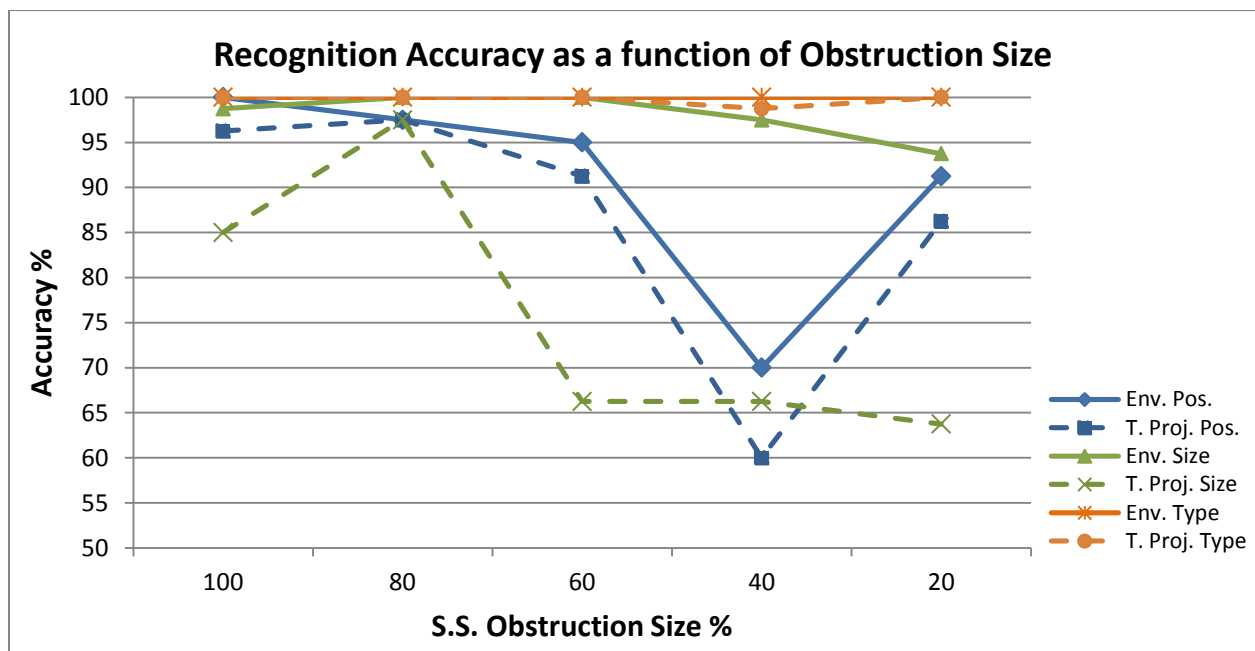


Figure 4-65 Algorithm accuracy using signal envelope and time-axis projection to estimate Delrin obstruction size, position and type in vinyl tube. The obstruction type (orange line) was estimated with accuracy of 100% using the signal envelope and over 95% using time-axis projection feature. For the obstruction size and position estimation, the envelope results with higher accuracies compared to the time-axis projection.

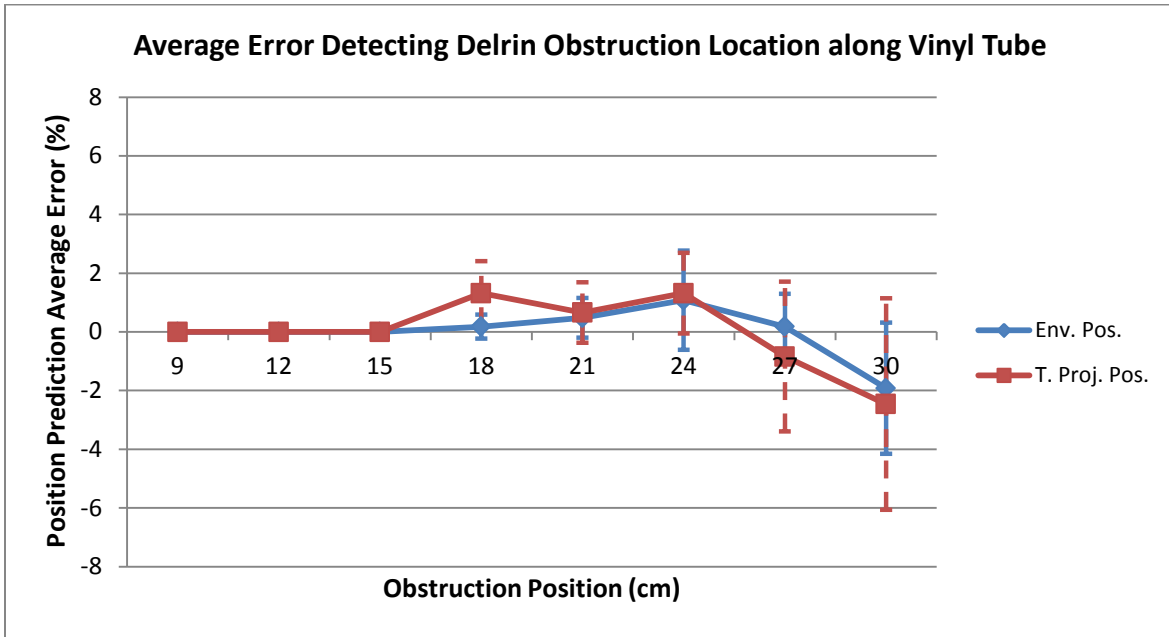


Figure 4-66 Average errors detecting Delrin obstruction position in water-filled vinyl tube, using the envelope detection and time-axis projection. As the obstruction position increases the average location error also increases, with a maximum error of -2.46 ± 3.60 cm (mean \pm STD) at 30cm using time-axis projection. Signal envelope shows lower error estimating the Delrin obstruction position.

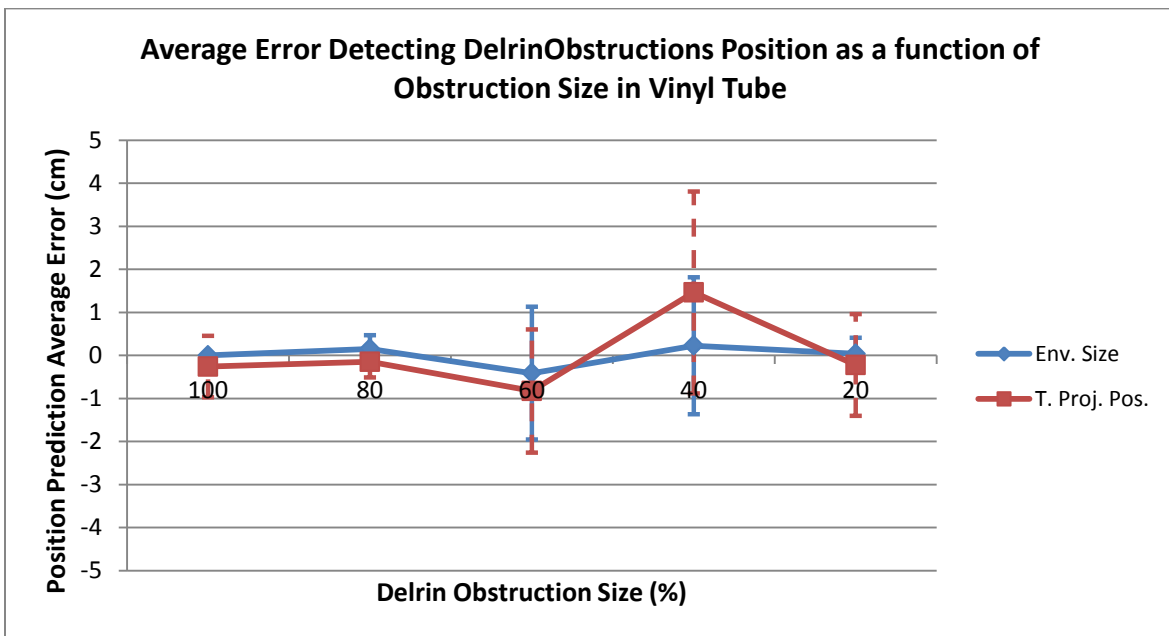


Figure 4-67 Average errors detecting Delrin obstructions position as function of obstruction size in water-filled vinyl tube. Both methods show similar error values except for 40% Delrin obstruction, where the time-axis projection error was 1.46 ± 2.34 cm (mean \pm STD) and -0.5 ± 1.58 cm (mean \pm STD) for the signal envelope.

Finally, Figure 4-68 and 4-69 presents the average errors estimating the Delrin obstruction size as a function of obstruction position and size, respectively. From Figure 4-68, can be stated that as the obstruction position increases the average error and standard deviation also increases, as occurred in the PVC and copper tube. The increase in the average error is mainly produced by the decrease of reflection amplitude for obstructions located far away from the hydrophone. This is more notable in Delrin obstruction reflections, since its intensity is lower than the S.S. obstructions. Figure 4-68 also shows that using the signal envelope (blue line) the error was slightly lower than using the time-axis projection (red line). The signal envelope also results with standard deviation much lower as the obstruction position increases compared to the time-axis projection.

Figure 4-69 shows that using the time-axis average errors increase for 100% and 20% Delrin obstructions. The 100% Delrin obstruction was underestimated to $-9 \pm 12.0\%$ (mean \pm STD) and the 20% obstruction was overestimated to $12.5 \pm 12.7\%$ (mean \pm STD). Yet again the envelope results on lower errors detecting the obstruction size compared to the time-axis projection.

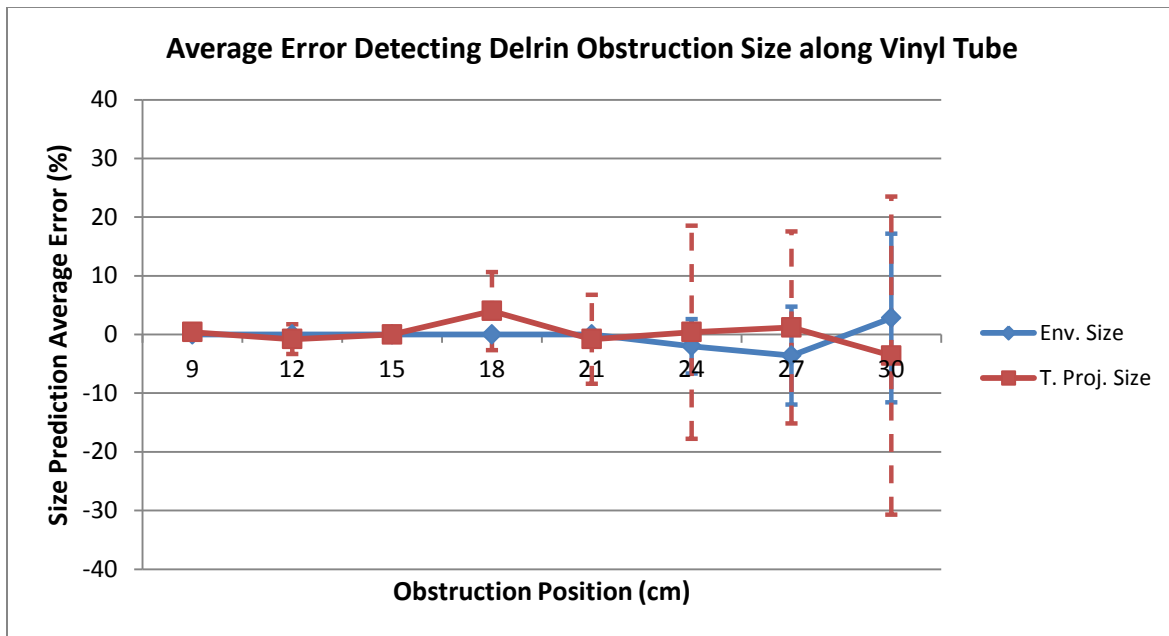


Figure 4-68 Average errors detecting Delrin obstruction size in water-filled vinyl tube, using the envelope detection and time-axis projection. As the obstruction position increases the average error and standard deviation estimating the obstruction size also increases, more notable using the time-axis projection. At 30cm the error using the time-axis projection was $-3.6 \pm 27.1\%$ (mean \pm STD) and with the signal envelope $2.8 \pm 14.3\%$ (mean \pm STD).

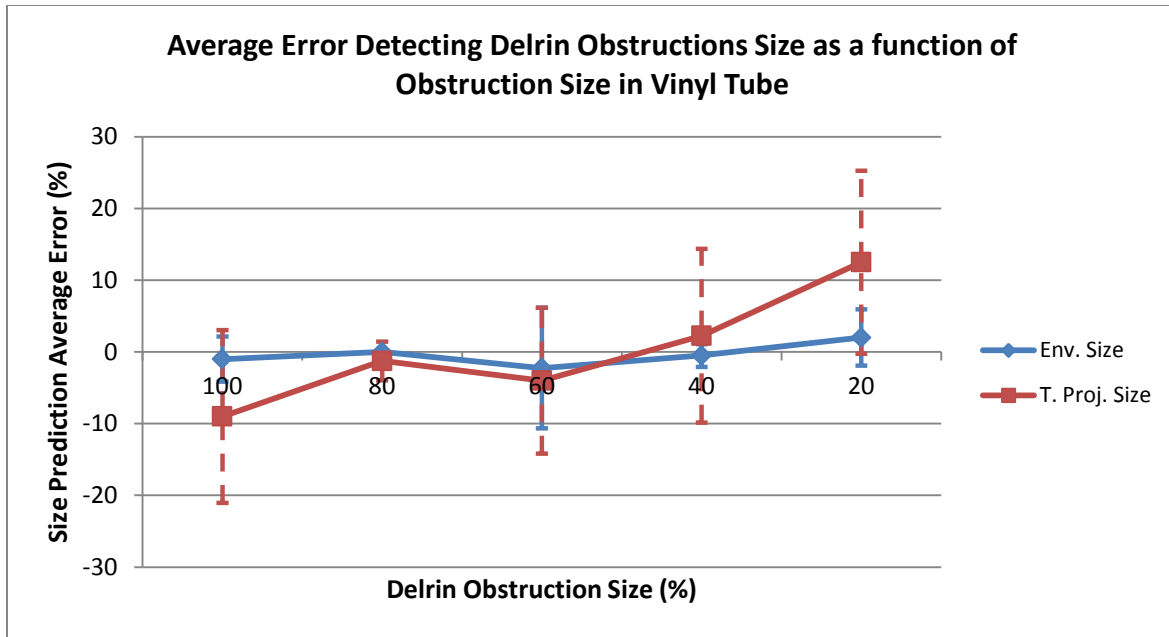


Figure 4-69 Average errors detecting Delrin obstructions size as function of obstruction size in water-filled vinyl tube. The signal envelope results on lower errors detecting the obstruction size than using time-axis projection. Time-axis projection error is higher for large and small Delrin obstructions.

4.4 Signal Envelope and Time-Axis Projection Comparison to Estimate Obstruction Type, Size and Position in water-filled PVC, Copper and Vinyl Tubes

Summarizing the results of the water-filled PVC, copper and vinyl tubes, Table 4-2 compares the accuracy and error values of the signal envelope and time-axis projection to estimate obstructions type, size and position. In the water-filled PVC tube, the obstruction position was estimated with an accuracy of 78.8% using the signal envelope, somewhat similar using the time-axis projection with an accuracy of 80.3%. The difference is that the signal envelope overall error was $0.93 \pm 0.59\text{cm}$ (mean \pm STD), considerable lower than $2.85 \pm 2.48\text{cm}$ (mean \pm STD) using the time-axis projection. For the obstruction size estimation in the PVC tube, the time-axis projection results with accuracy of 74.4%, against 64.3% using the signal envelope. The overall errors using the time-axis projection for obstruction size and position estimation in the PVC tube are always greater than using the signal envelope. Time axis projection also results with slightly more accuracy estimating the obstruction type in the PVC tube.

As Section 4.1.3.2.1 and 4.1.3.2.2 presents, the error estimating the obstruction position and size in the water-filled PVC tube increases as the obstructions position along the tube increases. Also as the obstruction size decreases the error tends to increase, due to the similarity between small S.S. and large Delrin obstructions. This similarity also produced that the accuracy of both methods estimating the obstruction type decreases.

Table 4-2 Accuracy and overall errors using the signal envelope and time-axis projection to estimate obstructions type, size and position in water-filled PVC, copper and vinyl tubes. For the water-filled copper and vinyl tubes, the signal envelope was able to estimate the obstruction type, size and position with higher accuracy and lower error values. For the water-filled PVC tube, the envelope estimates better the position, while the time-axis projection the obstruction size and type.

		Envelope Position	Time-Axis Position	Envelope Size	Time-Axis Size	Envelope Type Accuracy	Time-Axis Type Accuracy
Water-filled PVC Tube	Accuracy (%)	78.8 %	80.3 %	64.3 %	74.4 %	70.1 %	71.5 %
	Overall Error (mean \pm STD)	0.93 \pm 0.59 cm	2.85 \pm 2.48 cm	0.94 \pm 0.65 %	-1.78 \pm 3.91 %		
Water-filled Copper Tube	Accuracy (%)	85.3 %	83.4 %	93.0 %	87.4 %	99.2 %	95.7 %
	Overall Error (mean \pm STD)	0.19 \pm 2.04 cm	0.20 \pm 1.98 cm	-0.10 \pm 3.44 %	-0.33 \pm 4.85 %		
Water-filled Vinyl Tube	Accuracy (%)	85.2 %	82.8 %	90.3 %	83.1 %	99.1 %	98.6 %
	Overall Error (mean \pm STD)	0.02 \pm 0.86 cm	-0.02 \pm 1.11 cm	-0.22 \pm 3.71 %	-0.17 \pm 8.49 %		

For the water-filled copper tube, the signal envelope was able to better estimate the obstruction position, size and type, as Table 4-2 presents. The obstruction position overall error is quite similar using the signal envelope and time-axis projection, but the envelope accuracy was 85.3 % versus 83.4 % using the time-axis projection. In the obstruction size estimation the signal envelope outperforms the time-axis

projection with an accuracy of 93.0% and error of $-0.10 \pm 3.44\%$ (mean \pm STD) using the signal envelope, compared to 87.4% and $0.33 \pm 4.85\%$ (mean \pm STD) of error using the time-axis projection.

Finally, for the water-filled vinyl tube the signal envelope also outperforms the time-axis projection estimating the obstructions position, size and type. The overall error estimating the obstruction position using both methods is somewhat similar, while the accuracy using the signal envelope was 85.2% against 82.8% using the time-axis projection. For the obstruction size estimation, as Table 4-2 shows, the time-axis projection has less accuracy and higher standard deviations, meaning that this method estimated the obstruction size with less accuracy. Both methods show similar accuracies estimating the obstruction type in the water-filled vinyl tube. Using the signal envelope the accuracy was 99.1% versus 98.6% using the time-axis projection.

In the copper and vinyl tubes, as was for the PVC tube, the error estimating the obstruction position and size increases as the obstruction position increases and obstruction size decreases. This increase in error was more notable, as results showed, using the time-axis projection. The signal envelope in most of the cases showed higher accuracies and lower overall errors estimating obstructions position, size and type in the water-filled tubes under study.

CHAPTER 5

CONCLUSION AND RECOMENDATIONS

The analysis of acoustic reflections was performed using acoustic reflectometry in order to detect obstructions in liquid-filled tubes. An algorithm able to detect obstructions position, size and nature in different water-filled tubes was developed, using an experimental reflectometer capable to generate and record acoustic reflections traveling in the water inside different tubes. The experimental setup was used with tubes made of PVC and copper of 2.54cm diameter and a flexible vinyl tube of 1cm diameter. To achieve acoustic propagation in the water-filled tubes, a modulated acoustic pulse was used. The carrier frequency for the PVC and copper tubes of 2.54cm diameter was set to 200 kHz, while for the vinyl tube of 1.00cm diameter was increased to 300 kHz. As expected from theory for circular waveguides, the frequency needs to be increased as the waveguide radius decrease to achieve acoustic propagation along the waveguide.

From the wave propagation experiments was evident that the tube material influence the propagation of acoustic waves along water-filled tubes. The tube wall elasticity causes acoustic wave attenuation, due to the structural damping of the material, more notable in PVC and vinyl tubes compared to the copper tube.

The obstructions used for the experiments were made of stainless steel and Delrin, with sizes from 100% to 20% of the inner diameter for each tube. Measurements were recorded varying each obstruction size, type and position along the tubes. Two features were extracted from each obstruction reflection, the signal envelope and the spectrogram time-axis projection, to create a features database which was used to compare and estimate unknown obstructions reflections. The difference between stainless steel and Delrin obstructions was the amplitude and shape of their reflections. The acoustic impedance of Delrin obstructions is lower than stainless steel obstructions, resulting in reflections with

lower amplitudes. For obstructions of the same type this effect was also observed as the obstruction size decreases, since less cross sectional area of the water-filled tube was obstructed, lower amplitude reflections were produced.

A signal matching algorithm was developed to compare between the features extracted from an acoustic reflection and the features database, to estimate the position, size and type of the obstruction that produced the reflection. Using the signal envelope feature, the signal matching algorithm was able to estimate the obstruction position, size and type water-filled tubes made of copper with accuracies of 85.3%, 93.0% and 99.2% respectively, and 85.2%, 90.3% and 99.1% for the vinyl tube. In the water-filled PVC tube the obstruction position was estimated with an accuracy of 78.8% using the signal envelope and the obstruction size and type with accuracies of 74.4% and 71.5% respectively, using the time-axis projection. The average error estimating the obstruction position and size along each tube increases, as the obstruction position is located farther from the hydrophone. The more distance a reflection had to travel, its attenuation increases. Therefore, lower reflections are recorded becoming more difficult the features comparison performed by the signal matching algorithm, increasing the average errors estimating the obstruction position and size. Decreasing the obstructions size also presents this behavior, where less cross sectional area of the water-filled tube is obstructed, results in lower reflection coefficient and also lower amplitude reflections. As mentioned before the acoustic impedance of Delrin obstructions is lower than stainless steel obstructions, consequently Delrin obstruction reflections had lower amplitude than stainless steel, contributing to the increase of average errors estimating the obstruction position and size. To reduce the errors estimating the position and size of obstructions located at larger distances and with small sizes, the amplitude of the incident pulse should be increase, resulting in reflections with higher amplitudes. Thus, the features extracted from smaller obstructions located at farther distances contains more information to be compared by the signal matching algorithm.

With the results obtained during this research it can be stated that the approach utilized is accurate and precise, to estimate obstructions position, size and type in water-filled tubes made of PVC, copper and vinyl. This approach is used in audio identification and objects recognition, and consists in extracted

features of an acoustic signal, store them in a database and then, compare unknown acoustic reflections to the database to find the best match. It is also important to state that the envelope of the time-domain signals contain sufficient information to be used as acoustic signatures for each obstruction reflection, making the envelope a most reliable feature to detect and recognize obstructions in the water-filled tubes.

For future work it is necessary to use smaller acoustic transducers in order to perform experiments in narrow flexible tubes. The usable frequency range of the acoustic transducer needs to be high in order to accomplish acoustic propagation along narrow flexible tubes. As was performed in the liquid filled and surrounded vinyl tube experiments, it is recommended to use a layer of air or some material between the flexible tube walls that kept the acoustic wave traveling inside the liquid-filled tube. The T/R switch used in the experimental setup, an ADG419, may be changed to eliminate electrical crosstalk between channels, which limits how close from the hydrophone the obstruction measurements can be performed.

Once these limitations are overcome, the feature extraction and signal matching algorithms can be improved by optimizing the process to normalize the reflections data for each tube. Also other features, besides the signal envelope and time-axis projection, could be studied to detect obstructions position, size and type. In addition, the experimental setup and algorithms should be tested by experimenting with different types of liquids, different materials between the walls and obstructions.

REFERENCES

- [1] American Thoracic Society, Patient Information Series 2007, <http://patients.thoracic.org/information-series/en/resources/central-venous-catheter.pdf>
- [2] Migenix 10K Report, 2006.
- [3] Catheter Management, 2010,
<http://www.microbix.com/Public/Default.aspx?I=70&n=Catheter+Clearance>
- [4] S. Goyal, S. Punnam, G. Verma, F. Ruberg, “**Case Report - Persistent left superior vena cava: a case report and review of literature**”, *Cardiovascular Ultrasound Journal*, v 6, 2008.
- [5] Genentech’s Cathflo (Alteplase) reference brochure.
- [6] I. Marshall, “**Acoustic Reflectometry with an arbitrary short source tube**”, *Journal of the Acoustical Society of America*, v 91, issue 6, p 3558-3564, 1992.
- [7] E. Zeron, O. Yañez, R. Gonzalez, “**Steady-State acoustic reflectometry for the reconstruction of solid cylindrical cavities**”, *Proceedings of the Second Joint EMBS/BMES Conference IEEE*, 2002.
- [8] D. Sharp, “**Increasing the length of tubular objects that can be measured using acoustic pulse reflectometry**”, *Journal of Measurement Science and Technology*, v 9, p 1469-1479, 1998.
- [9] J. Buick, J. Kemp, D. Sharp, M van Walstijn, D. Campbell, R. Smith, “**Distinguishing between similar tubular objects using pulse reflectometry: a study of trumpet and cornet lead pipes**”, *Journal of Measurement Science and Technology*, v 13, p 750-757, 2002.
- [10] H. Figueroa, E. Juan, “**Estimation of Tube Wall Compliance Using Pulse-Echo Acoustic Reflectometry**”, *Proceedings 28th Annual International Conference IEEE EMBS*, 2006.
- [11] Solcomhouse - Understanding Sonar, 2010, <http://www.solcomhouse.com/SONAR.htm>.
- [12] E. Juan, G. Wodicka, “**Miniature Acoustic Guidance System for Endotracheal Tubes**”, Thesis submitted to the faculty of Purdue University, 2001.
- [13] EarCheck, 2008, http://www.earcheck.com/resources/dyn/files/91706/_fn/EarCheck+FAQs.pdf
- [14] SonarMed™ Airway Monitoring System, 2011, <http://www.sonarmed.com/>

- [15] M. Kim, S. Lee, “**Detection of leak acoustic signal in buried gas pipe based on the time–frequency analysis**”, *Journal of Loss Prevention in the Process Industries*, v 22, p 990-994, 2009.
- [16] K. Papadopoulou, M. Shamout, B. Lennox, D. Mackay, A. Taylor, J. Turner, X. Wang, “**An Evaluation of Acoustic Reflectometry for Leakage and Blockage Detection**”, *Proc. IMECHE*, v 222, p 959-966, 2008.
- [17] M. Lowe, D. Alleyne, P. Cawley, “**Defect Detection in Pipes Using Guided Waves**”, *Ultrasonincs*, v 36, p 147-154, 1998.
- [18] C. Aristegui, M. Lowe, P. Cawley, “**Guided waves in fluid-filled pipes surrounded by different fluids**”, *Ultrasonics*, v 39, p 367-375, 2001.
- [19] L. Segura, “**Acoustic wave dispersion in a cylindrical elastic tube filled with a viscous liquid**”, *Ultrasonics*, v 37, p 537-547, 2000.
- [20] L. Lafleur, F. Shields, “**Low-frequency propagation modes in a liquid-filled elastic tube waveguide**”, *Journal of the Acoustical Society of America*, v 97, issue 3, p 1435-1445, 1995.
- [21] R. Urick, “Principles of Underwater Sound”, McGraw-Hill Book Company, New York, NY, pp 423 , 1983.
- [22] Discovery of Sound in the Sea: Sound Travel in the Sofar Channel,
<http://www.dosits.org/science/soundmovement/sofar/sofartravel/>
- [23] R. Martinez, L. Leija, A. Vera, “**Ultrasonic Attenuation in Pure Water: Comparison between Through-Transmission and Pulse-Echo Techniques**”, *Pan American Health Care Exchange (PAHCE)*, p 81-84, 2010.
- [24] B. Sturtevant, M. da Cunha, “**BAW Phase Velocity Measurements by Conventional Pulse Echo Techniques with Correction for Couplant Effect**”, *IEEE Ultrasonics Symposium*, p 2261-2264, 2006.
- [25] L. Kinsler, A. Frey, A. Coppens, J. Sanders, “Fundamentals of Acoustics”, 3rd Edition, John Wiley & Sons Inc. Publishing, 1982.
- [26] X. Tian, D. Zhou, Z. Liu, “**Object Recognition Algorithm of Sonar Image**”, *8th International Conference on Signal Processing*, v2, 2006.

- [27] M. Ecemig, P. Gaudiano, “**Object Recognition with Ultrasonic Sensors**”, *IEEE International Symposium on Computational Intelligence in Robotics and Automation (CIRA)*, p 250, 1999.
- [28] MK 60 Encapsulated Torpedo (CAPTOR), <http://www.fas.org/man/dod-101/sys/dumb/mk60.htm>
- [29] M. Munich, “**Bayesian Subspace Methods for Acoustic Signature Recognition of Vehicles**”, *Proceedings 12th European Signal Processing Conference (EUSIPCO)*, 2004.
- [30] J. Santiago, R. Carbó, “**Acoustic Signature of Two Spanish Oceanographic Ships**”, *Underwater Acoustics Forum Acusticum Sevilla*, 2002.
- [31] P. Cano, E. Batle, T. Kalker, J. Haitisma, “**A Review of Algorithms for Audio Fingerprinting**”, *Multimedia Signal Processing IEEE Workshop*, p 169-173, 2002.
- [32] S. Haykin, “*Communications Systems*”, 3rd Edition, John Wiley & Sons Inc. Publishing, 1994.
- [33] F. Mapelli, R. Pezzano, R. Lancini, “**Robust Audio Fingerprinting for Song Identification**”, *12th European Signal Processing Conference (EUSIPCO)*, p 2095-2098, 2004.
- [34] G. Richly, L. Varga, F. Kovács, G. Hosszú, “**Short-term sound stream characterization for reliable, real-time occurrence monitoring of given sound-prints**”, *Proc. 10th Mediterranean Electrotechnical Conference*, 2000.
- [35] T. Blum, D. Keislar, J. Wheaton, E. Wold, “**Method and article of manufacture for content-based analysis, retrieval and segmentation of audio information**”, U.S. Patent 5,918,223, June, 1999.
- [36] Onda Corporation – References, 2011, <http://www.ondacorp.com/images/Gases.pdf>
- [37] Onda Corporation – References, 2011, <http://www.ondacorp.com/images/Liquids.pdf>
- [38] Onda Corporation – References, 2011, <http://www.ondacorp.com/images/Plastics.pdf>
- [39] Onda Corporation – References, 2011, <http://www.ondacorp.com/images/Solids.pdf>